5-2012

Novel Phantoms And Post-Processing For Diffusion Spectrum Imaging

Vaibhav Juneja

Recommended Citation

NOVEL PHANTOMS AND POST-PROCESSING FOR DIFFUSION SPECTRUM

IMAGING

by

Vaibhav Juneja, M.S, B.S.

APPROVED:

_____
Ponnada A. Narayana, Ph.D., Supervisory Professor

_____
Khader M. Hasan, Ph.D.

_____
John D. Hazle, Ph.D.

_____
F. Gerard Moeller, M.D.

_____
Richard E. Wendt, III, Ph.D.

_____
Jerry S. Wolinsky, M.D.

_____

APPROVED:

_____
Dean, The University of Texas
Graduate School of Biomedical Sciences at Houston

NOVEL PHANTOMS AND POST-PROCESSING FOR DIFFUSION SPECTRUM

IMAGING

A

DISSERTATION

Presented to the Faculty of
The University of Texas
Health Science Center at Houston
and
The University of Texas
M. D. Anderson Cancer Center
Graduate School of Biomedical Sciences
in Partial Fulfillment

of the Requirements

for the Degree of

DOCTOR OF PHILOSOPHY

by

Vaibhav Juneja, M.S, B.S.
Houston, Texas

May, 2012

DEDICATION

This dissertation is dedicated to my parents and family

Acknowledgements

First and foremost, I would like to express my gratitude towards my dissertation advisor Dr. Ponnada A. Narayana for his constant support, encouragement, mentorship and for believing in me throughout the years of my graduate studies. I have grown considerably both professionally and personally working in his lab under his guidance.

I would also like to thank all the members of my supervisory committee members Dr. Khader M. Hasan, Dr. John D. Hazle, Dr. F. Gerard Moeller, Dr. Joel L. Steinberg, Dr. Richard E. Wendt, III and Dr. Jerry S. Wolinsky for their continued constructive criticisms.

I would also like to thank Dr. Yuxiang Zhou for assistance with data acquisition and feedback with data analysis; Vips Patel for MR scanner support; Chris Kuether at university of Houston for machine shop work; Dr. John Putkey for providing the degassing equipment and all my lab members for their camaraderie.

Finally, I would like to thank my family for their constant love, support and for their understanding when I had to skip family functions to prioritize my Ph.D. work.

Novel Phantoms and Post-Processing for Diffusion Spectrum Imaging

Vaibhav Juneja, M.S.

Supervisory Professor: Ponnada A. Narayana, Ph.D.

High Angular Resolution Diffusion Imaging (HARDI) techniques, including Diffusion Spectrum Imaging (DSI), have been proposed to resolve crossing and other complex fiber architecture in the human brain white matter. In these methods, directional information of diffusion is inferred from the peaks in the orientation distribution function (ODF). Extensive studies using histology on macaque brain, cat cerebellum, rat hippocampus and optic tracts, and bovine tongue are qualitatively in agreement with the DSI-derived ODFs and tractography. However, there are only two studies in the literature which validated the DSI results using physical phantoms and both these studies were not performed on a clinical MRI scanner. Also, the limited studies which optimized DSI in a clinical setting, did not involve a comparison against physical phantoms. Finally, there is lack of consensus on the necessary pre- and post-processing steps in DSI; and ground truth diffusion fiber phantoms are not yet standardized. Therefore, the aims of this dissertation were to design and construct novel diffusion phantoms, employ post-processing techniques in order to systematically validate and optimize (DSI)-derived fiber ODFs in the crossing regions on a clinical 3T MR scanner, and develop user-friendly software for DSI data reconstruction and analysis. Phantoms with a fixed crossing fiber configuration of two crossing fibers at 90° and 45° respectively along with a phantom with three crossing fibers at 60°, using novel hollow plastic capillaries and novel placeholders, were constructed. T2-weighted MRI results on these phantoms demonstrated high SNR, homogeneous signal, and absence of air bubbles.

Also, a technique to deconvolve the response function of an individual peak from the overall ODF was implemented, in addition to other DSI post-processing steps. This technique greatly improved the angular resolution of the otherwise unresolvable peaks in a crossing fiber ODF. The effects of DSI acquisition parameters and SNR on the resultant angular accuracy of DSI on the clinical scanner were studied and quantified using the developed phantoms. With a high angular direction sampling and reasonable levels of SNR, quantification of a crossing region in the 90°, 45° and 60° phantoms resulted in a successful detection of angular information with mean $\pm$ SD of 86.93°$\pm$2.65°, 44.61°$\pm$1.6° and 60.03°$\pm$2.21° respectively, while simultaneously enhancing the ODFs in regions containing single fibers. For the applicability of these validated methodologies in DSI, improvement in ODFs and fiber tracking from known crossing fiber regions in normal human subjects were demonstrated; and an in-house software package in MATLAB which streamlines the data reconstruction and post-processing for DSI, with easy to use graphical user interface was developed. In conclusion, the phantoms developed in this dissertation offer a means of providing ground truth for validation of reconstruction and tractography algorithms of various diffusion models (including DSI). Also, the deconvolution methodology (when applied as an additional DSI post-processing step) significantly improved the angular accuracy of the ODFs obtained from DSI, and should be applicable to ODFs obtained from the other high angular resolution diffusion imaging techniques.

Table of Contents

Chapter – 1: Introduction and Motivation

Chapter – 2: Background on Diffusion MRI and Diffusion Physics

Chapter – 3: Design and Development of Diffusion Phantoms

[x]

Chapter – 5: Quantitative Evaluation of DSI Using the Phantoms and Application to Human Fiber Tracking

List of Figures

List of Tables

CHAPTER 1 – Introduction and Motivation

1.1 INTRODUCTION

Magnetic resonance imaging (MRI) is a well-established noninvasive radiologic modality for providing soft tissue contrast [1]. Diffusion weighted MRI, a specialized MRI methodology sensitive to water diffusion, holds great potential for probing tissue micro-structural organization for detecting pathology that is not seen on conventional MRI. Since its inception in early 1990s, diffusion tensor imaging (DTI), which exploits the preferential water diffusion along some structures (such as white matter tracts in the central nervous system) [2], is widely used both clinically and in basic research for probing the micro-structural organization of tissues, quantifying white matter integrity and performing tractography [3-11]. However, with the inherent single tensor model assumption, DTI cannot resolve crossing or kissing fibers, thereby limiting its ability to generate reliable fiber tractography [12-15]. Moreover, reduced anisotropy in the regions of crossing fibers may be misinterpreted as a loss of axonal integrity.

High angular resolution diffusion imaging (HARDI) techniques including diffusion spectrum imaging (DSI) and q-ball imaging (QBI) have been proposed to resolve crossing and other complex fiber architecture in the human brain white matter [13, 15-20]. In these methods, directional information of diffusion is inferred from the peaks in the orientation distribution function (ODF). DSI is shown to resolve complex white matter tissue architecture [15, 17, 21]. Extensive studies using histology on macaque brain [22, 23], cat

cerebellum [24], rat hippocampus and optic tracts [25, 26] and bovine tongue[27] are qualitatively in agreement with the DSI-derived tractography.

1.2 Motivation

However, there are two main frameworks in DSI which need to be addressed in more detail and are the major foci of this thesis work:

1) **DSI validation and optimization with ground truth phantoms on a clinical scanner:** There are two studies in the literature which validated DSI using physical phantoms [26, 28]. However, both these studies were not performed on a clinical MRI scanner. Also, the limited studies which optimized DSI in a clinical setting [29, 30] did not involve a comparison against a ground truth physical phantom. Under the constraint of scan time and gradient performance on current clinical systems, it is important to study the effect of parameters which have a significant impact on the angular resolution of DSI. This will allow the optimization of DSI acquisition parameters.

2) **DSI post-processing to address the issue of fibers crossing at small angles:** ODF based methodologies (including DSI) may yield inaccurate orientation information in regions where fibers cross at relatively acute angles, because each contributing fiber bundle generates a peak of finite width, which makes it difficult to resolve the true peaks in the ODF [31]. This problem can be ameliorated by deconvolving the response function of a single fiber from the overall fiber response and is the basis of techniques such as Spherical Deconvolution [32] and QBI Sharpening[31]. There are two recent studies [33, 34] in the context of application of deconvolution in DSI

which were published during the conclusive phase of this thesis. However, the methodologies developed in this thesis are unique in their own right. Overall, currently there is lack of consensus in the DSI community on the necessary pre- and post-processing steps.

In addition, although there are several diffusion fiber crossing phantoms proposed in the literature, they were designed only with two crossing fibers and are rather simplistic for validation purpose. A careful investigation using a three fiber crossing phantom is essential for validation of DSI and other HARDI techniques since such fiber crossings are encountered in multiple brain regions (for eg. in centrum semiovale region where 3 fibers from corpus callosum, corona radiata and superior longitudinal fasciculus intersect and cross).

Also, majority of the diffusion fiber crossing phantoms reported in the literature are constructed using textile fibers, which depend upon the signal from the water protons trapped in between synthetic textile fiber material and may be unreliable. In addition, these phantoms lack the desired tubular geometry [35]. In order to pack the fibers densely and homogeneously while maintaining orientation and simultaneously increasing the packing density, such phantoms generally employ heat shrink tubes [36, 37] or a fiber tightening mechanism[38, 39]. Such design mechanisms leads to inaccuracies in fiber density and introduces uncertainty in the underlying geometry. Hollow capillary tubing is advantageous for this reason. However, one of the main disadvantages of the hollow capillary tubing reported in the literature is large wall thickness (350 µm o.d.) which results in a lower packing density leading to a low SNR.

Therefore, the overall purposes of this dissertation were to design and construct novel diffusion phantoms including three fiber crossings, employ post-processing techniques in order to systematically validate and optimize DSI on a clinical 3T MR scanner, and develop user-friendly software for DSI data reconstruction and analysis.

1.3 Objective and Specific Aims

The main objectives of this research are 1) to design and construct phantoms with two and three fiber crossings for validating DSI-determined angular orientations and 2) to implement deconvolution algorithms as a post-processing step in DSI to enhance resolution of crossing fibers.

The specific aims of this thesis were:

1) To systematically design and construct diffusion fiber crossing phantoms with increasing complexity from two to three interleaved fiber crossings (with different angles serving as test conditions) using hollow plastic capillaries (i.d.=50,o.d.=150) in order to achieve a high packing ratio leading to a high SNR.

2) To implement a deconvolution technique applicable to DSI data as a post-processing step to resolve the peaks in the ODF for determining the fiber orientation with improved accuracy in the regions where fibers cross at acute angles.

3) To acquire and analyze DSI data on the developed phantoms and evaluate angular accuracy of DSI derived ODFs against the known ground truth, especially in the regions of crossing fibers.

[4]

4) To acquire and analyze DSI data on normal human subjects and perform white matter fiber tractography in known fiber crossing regions to demonstrate applicability of the developed methodologies.

1.4 Thesis Organization

The organization of the thesis is as follows:

Chapter 2 provides a background on the basic principles of diffusion MRI.

Chapter 3 outlines various physical diffusion phantoms published in the literature with their respective materials, design principles, advantages and disadvantages. Motivation for developing the phantoms in this thesis is described. The diffusion phantoms developed in this work are then presented in details including their physical construction and design methodology. The developed phantoms offer a means of providing "ground truth" for validation of various diffusion models (particularly the ones that aims to resolve the crossing fibers) and for validation of tractography algorithms.

Chapter 4 presents the current post-processing methodology in DSI and discusses their limitations. The common issue of compromised angular accuracy of ODF based methodologies in the regions of fibers crossing at acute angles is discussed. The current DSI analysis methodologies are described and their limitations are pointed out. A deconvolution based technique applicable to DSI data as a post-processing step is described and implemented on the developed phantoms.

Chapter 5 describes the validation of the DSI analysis using the developed phantoms. Quantitative evaluation of angular accuracy of the DSI derived ODF using these phantoms is

presented. The consequence of DSI acquisition parameters on the angular resolution in phantoms is quantified. The improvement in these regions by applying deconvolution is demonstrated. In addition, the applicability of the developed methodologies on normal human subjects is presented qualitatively. Known regions of human brain consisting of single fibers and crossing fibers are highlighted. Deconvolution seems to improve the fiber delineation and detection from these regions.

Chapter 6 provides summary and future directions based on this work.

CHAPTER 2– Background on Diffusion MRI and Diffusion Physics

2.1 INTRODUCTION

Deciphering human brain structures and their inter-connecting pathways and networks are very active research areas since they have numerous applications in the clinical diagnosis and management of multiple brain disorders. To this end, a large variety of invasive neuro-anatomic methods such as tract tracing were introduced early on to study brain white matter structural configuration and connectivity. However such techniques are not applicable to human studies.

Diffusion weighted MRI, a specialized MRI methodology sensitive to water diffusion, is the only imaging modality that holds great potential for probing tissue micro-structural organization for detecting pathology that is not seen on conventional MRI. The following sections provide the physical origin of the diffusion signal and how it can be measured with MRI.

2.2 Molecular diffusion phenomena

Molecular diffusion is a physical process referring to the random translational motion of molecules in a fluid (for eg. water) owing to their thermal agitation. This phenomenon is also called Brownian motion which is named after Robert Brown, an English botanist in 1827 who observed pollen grains in water under a microscope and found that the pollen

grains were in a constant agitated state. Brown first hypothesized that this phenomenon must be due to something alive, but by observing the same kind of motion in inclusions in quartz that were millions of years old, he discarded this hypothesis and was never able to explain his observations. In 1905, Albert Einstein's molecular-kinetic theory of heat led to Jean Perrin's work in 1909 of precise quantitative measurements of Brownian motion under a microscope. Einstein's theory and Perrin's observations together established the statistical law governing the randomness of these molecules undergoing Brownian motion.

A simplified version of this law for one-dimensional (1D) case is depicted in Fig.2.1, where the variance $< x^2 >$ of the molecular displacement along the dimension x is given by the following equation,

$$< x^2 > = 2D\tau \tag{2.1}$$

where τ is the diffusion time (the time during which the molecules are allowed to diffuse); D is the diffusion coefficient which depends only on the size (mass) of the molecules, the viscosity and the temperature of the medium. Taking square root of both sides of Eq.1, we get the root-mean-square of $< x^2 >$ as follows,

$$\mathrm{r.m.s.}(< x^2 >) = \sqrt{< x^2 >} = \sqrt{2D\tau} \tag{2.2}$$

Hence, given a large number of molecules, the size of the ensemble average $<.>$ molecular excursion increases linearly with $\sqrt{\tau}$ (since D may be considered a constant of proportionality. This mean distance traveled by a pollen grain (suspended in water) increases as the square root of time.

To get a sense of some numbers, the value of D for free water molecules in water at room temperature (37 °C) is 3×10^{-9} m²/sec. Substituting this value of D in Eq.2, for $\tau = 50$ msec, the ensemble of the molecules would have travelled a distance of 17 µm. This ensemble average movement follows a probability distribution function which is discussed in the next section.
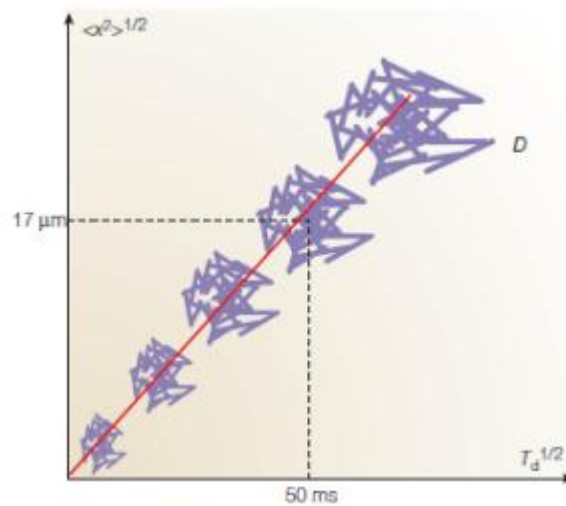
Fig.2.1: Brownian Motion. Given a large number of molecules, the size of the ensemble average $<.>$ molecular excursion increases linearly with $\sqrt{\tau}$. for $\tau = 50\ msec$, the ensemble of the molecules would have travelled a distance of $17\ µm$. Image taken from [40]. Reprinted by permission from Macmillan Publishers Ltd: Nature Reviews Neurosci (40), copyright (2003)

2.3 Diffusion propagator or probability density function (PDF)

The probability distribution function (PDF) governs the probability of molecular displacement, in terms of both magnitude and direction, of the ensemble of molecules undergoing the random Brownian motion. This function is also referred to as the diffusion propagator (this has many alternate names in literature such as displacement probability density function or image of molecular displacement [41]). I will refer to this as PDF for simplicity of representation and denote it as $P(R, \tau)$, where R is the relative molecular displacement vector which may be thought of as the difference of the molecular positions during the diffusion time (τ). Mathematically,

$$R = x(\tau) - x(0) \tag{2.3}$$

where, $x(0)$ and $x(\tau)$ represents the initial and final molecular positions, respectively.

Typically, for free water, the shape of the PDF is Gaussian [40, 41]. In accordance with the Gaussian distribution, approximately 68 % of the molecules undergoing Brownian motion travel less than 17 μm (which is the standard deviation of the mean derived in the previous section) and only 5% of the molecules would have moved a distance greater than 34 μm. Suppose, N is the total number of molecules. Hence, the proportion of the molecules which have travelled a distance r in time τ is represented as n/N (which gives the probability of the molecules to have travelled a distance r in time τ). For $r > 17\ \mu m$ (in our example) this probability will be low, and even lower for $r > 34\ \mu m$.

The PDF is, however, much more complex than a simple Gaussian distribution in real tissues and the estimation of this PDF is central to all the diffusion imaging schemes

discussed in later sections. The next section briefly discusses the origins of diffusion encoding in MRI.

2.4 Diffusion encoding in MRI

Following the establishment of nuclear magnetic resonance (NMR) phenomena in 1946 by Bloch and Purcell[42], Hahn's spin echo experiment [43] in 1950 in which he also noted that the Brownian motion of spins under a non-uniform magnetic field leads to a signal attenuation. Carr and Purcell created 1D MR images using magnetic field gradients in 1954. These discoveries formed the foundation for diffusion MRI. Subsequently, in 1965, Stejskal and Tanner proposed a pulsed gradient spin echo (PGSE) sequence [44] to encode the diffusion weighted signal in Hahn's spin echo pulse sequence. Fig.2.2 shows this PGSE pulse sequence includes a pair of equal rectangular gradient pulses are applied on the either side of 180° degree refocusing RF pulse, in each TE/2 period. The first gradient pulse creates a phase shift of the spins whereas the second pulse nullifies this phase shift for the static spins only. Hence the spins which have the experienced position change due to diffusion in the diffusion time (Δ) undergo different phase shifts resulting in attenuated T2 signal. The random phase shifts of individual spins ultimately leads to a signal attenuation [45], The corresponding echo attenuation is given by [46] ,

$$S(b, TE)_{SE} = S_0 e^{-TE/T_2} e^{-bD} \tag{2.4}$$

where S is the diffusion weighted signal acquired, S_0 represents the spin echo signal obtained without any diffusion encoding gradients, D is the apparent diffusion coefficient, b is the diffusion-sensitizing factor (b-value) given by the following equation,

[11]

$$b = \gamma^2 \delta^2 g^2 \left(\Delta - \frac{\delta}{3}\right) \tag{2.5}$$

where γ is the gyromagnetic ratio, δ is the duration of the diffusion gradient pulse, Δ is the time interval between the application of the two diffusion gradients (i.e. diffusion time), and g is the applied gradient strength (see Fig.2.2)

Finally, by repeating the experiment with two different b-values (i.e. b_0 and b_1), the apparent diffusion coefficient (D) can be computed as follows,

$$D = -\frac{1}{b_1 - b_0} \ln(S(b_1)/S(b_0)) \tag{2.6}$$

Several alternatives of the Stejskal and Tanner PGSE sequence have been introduced over the years such as single-shot diffusion-weighted spin echo EPI pulse sequence, diffusion-weighted stimulated echo sequence, radial scanning, spiral scan to name a few [46]. However, the basic principle of encoding diffusion remains the same.
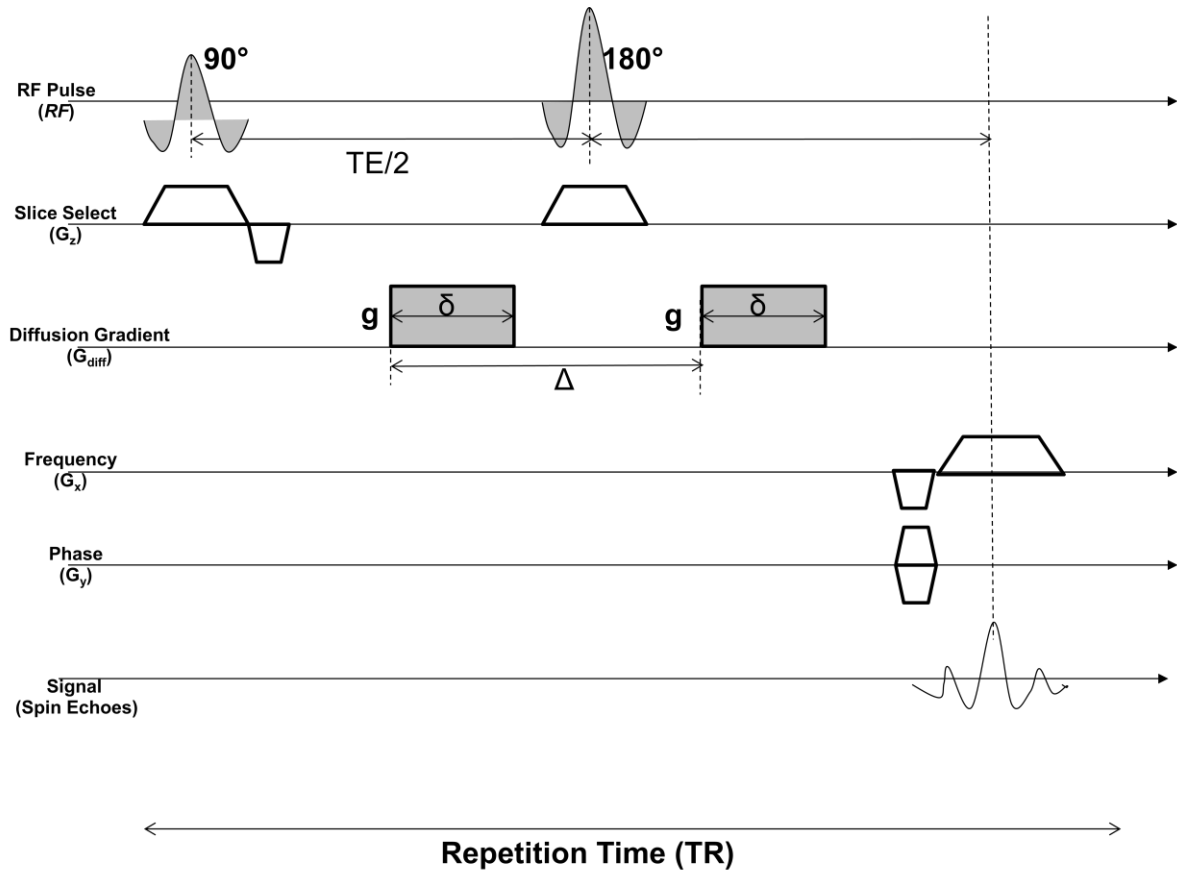
Fig.2.2: Stejskal and Tanner PGSE Pulse Sequence. The PGSE pulse sequence is a modified spin echo pulse sequence which include a pair of equal rectangular gradient pulses are applied on the either side of 180° degree refocusing RF pulse in each TE/2 period. δ is the duration of the diffusion gradient pulse, Δ is the time interval between the application of the two diffusion gradients (i.e. diffusion time).

2.5 Apparent diffusion coefficient (ADC) and diffusion anisotropy (DA)

The term apparent diffusion coefficient is used in the literature to include the effectS of underlying cellular microstructure of the tissue which creates numerous additional barriers and various individual compartments (eg. intracellular, extracellular, neurons, glial cells, axons) within the tissue [47]. These together impede the translational mobility of the diffusing particles (as shown in Fig.2.3). Appropriate acquisition along with mathematical

[13]

modeling allows inferring the microstructural tissue organization from the measured diffusion signal.
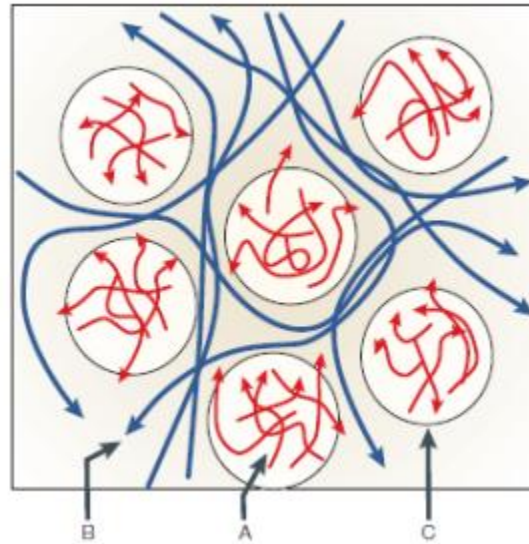
Fig.2.3: Impediment of Diffusing Particles in Biological Tissues. The underlying cellular microstructure of the tissue creates numerous additional barriers and various individual compartments. (A) Restriction created by closed spaces such as cells; (B) Diffusion hindered by obstacles causing deviated paths and (C) compartmental exchange, all lead to an impeded diffusion. Image taken from [40]. Reprinted by permission from Macmillan Publishers Ltd: Nature Reviews Neurosci (40), copyright (2003)

Due to restricted boundaries in tissues, the diffusion in one direction in space usually differs from another direction. In the regions of highly oriented barriers (such as the case in brain white matter), this leads to a preferential direction of diffusion and referred to as an anisotropic (Fig.2.4 b) diffusion, a term used in the literature to distinguish it from isotropic (Fig.2.4 a) diffusion (which is the case if diffusion is equal in all direction when the restrictive boundaries are not there). Both isotropic and anisotropic diffusion are exploited via diffusion MRI to infer the normal and pathological states (for example, the diffusion which is usually anisotropic becomes isotropic in the presence of edema). The anisotropic

diffusion is very useful in inferring the white matter architecture and in performing white matter fiber tractography.
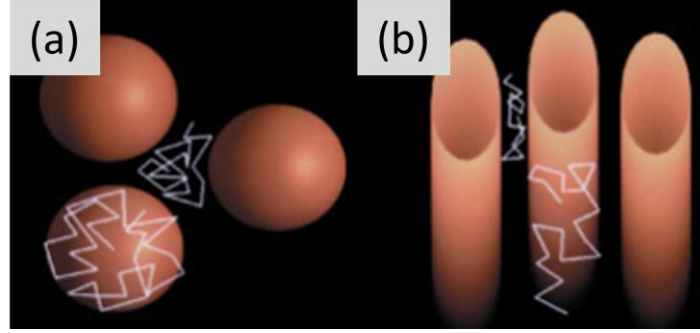
Fig.2.4: Isotropic and Anisotropic Diffusion. (a) isotropic diffusion (diffusion is equal in all direction when the restrictive boundaries are not there) (b) anisotropic diffusion (In the regions of highly oriented barriers diffusion has a preferential direction along the oriented barriers). Image taken from [47]. Reprinted by permission from Macmillan Publishers Ltd: NMR Biomed (47), copyright (2002)

2.6 Diffusion tensor imaging (DTI)

The Diffusion Tensor Imaging is a well established diffusion and is widely used both clinically and in basic research for probing the micro-structural organization of tissues, quantifying white matter integrity and performing tractography [3-11]. It was formulated in [2, 48-50] by Peter Basser who proposed to use a second order symmetric and positive-definite tensor (D) to model the intrinsic diffusion properties of biological tissues. DTI is based on the simple Gaussian assumption of the PDF (introduced in the previous sections), which leads to the following expression of the PDF,

$$P(R, \tau) = \frac{1}{\sqrt{(4\pi\tau)^3 \, |D|}} \; e^{-R^T D^{-1} R/4\tau} \tag{2.7}$$

where $|D|$ is the determinant of the diffusion tensor, D. Hence, in DTI, the PDF is approximated by a 3-variate normal distribution with zero mean. The diffusion tensor is encoded from diffusion-weighted images (DWIs) as follows,

The recorded DWI signal intensity S is given by:

$$S = S_0 e^{-bg^T Dg} \qquad (2.8)$$

where D is the diffusion tensor given by:

$$D = \begin{bmatrix} D_{xx} & D_{xy} & D_{xz} \\ D_{yx} & D_{yy} & D_{yz} \\ D_{zx} & D_{zy} & D_{zz} \end{bmatrix} \qquad (2.9)$$

Note that D is symmetric; the Signal equation can be rewritten as:

$$S = S_0 e^{-bd.g} \qquad (2.10)$$

where d is a 6 x 1 vector of diffusion tensor elements

$$d = \begin{bmatrix} D_{xx} & D_{yy} & D_{zz} & D_{xy} & D_{xz} & D_{yz} \end{bmatrix} \qquad (2.11)$$

g is a 1 x 6 diffusion gradient vector given by

$$g = \begin{bmatrix} g_x^2 & g_y^2 & g_z^2 & 2g_x g_y & 2g_x g_z & 2g_y g_z \end{bmatrix} \qquad (2.12)$$

Let $y = -(1/b) \ln S/S_0$, then $y = d.g$ $\qquad (2.13)$

which can be rewritten in matrix form as,

$$G.d = Y \qquad (2.14)$$

where for N number of gradient encoding directions applied, G is a matrix of dimensions N x 6 (each row of G contains one g vector) Y is a column vector of N x 1 dimensions (each y values for each gradient direction).

From the above equation, computing the 6 diffusion tensor elements in d can be formulated as a problem of solving a system of linear equations.

$$d = (G^\sim G)^{-1} G^\sim Y \qquad (2.15)$$

To solve 6 unknowns in d requires at least six linear equations. Thus the DWIs need to be acquired with at least 6 encoding directions plus one S_0 image). However, in general more than six directions are employed for solving the equations [51]. To transform the diffusion measurements from the laboratory coordinate system to the subject coordinate system, the diffusion tensor is diagonalized to determine the eigenvectors e1, e2, e3 and eigen-values $\lambda 1, \lambda 2, \lambda 3$. From these, several rotationally invariant quantities can be extracted, amongst which two of the most commonly used DTI metrics are the apparent diffusion coefficient (ADC) and Fractional anisotropy (FA) which can be calculated using the following.

$$ADC = (\lambda_1 + \lambda_2 + \lambda_3)/3 \qquad (2.16)$$

$$FA = \frac{\sqrt{((\lambda_1 - \lambda_2)^2 + (\lambda_2 - \lambda_3)^2 + (\lambda_3 - \lambda_1)^2)}}{\sqrt{2(\lambda_1^2 + \lambda_2^2 + \lambda_3^2}} \qquad (2.17)$$

Although an elegant and widely used formulation, DTI cannot resolve crossing or kissing fibers, owing to the inherent single tensor model assumption. DTI is thereby limited in its ability to generate reliable fiber tractography [12-15]. Moreover, reduced anisotropy in

the regions of crossing fibers may be misinterpreted as a loss of axonal integrity. In one of several attempts to resolve crossing and other complex fiber architecture in the human brain white matter, High Angular Resolution Diffusion Imaging (HARDI) techniques including Diffusion Spectrum Imaging (DSI) based on q-space formalism have been proposed. This is discussed next.

2.7 Q-space imaging (QSI) and diffusion spectrum imaging (DSI)

QSI has the ability to provide information on complex underlying architecture including crossing and touching fibers which could not be resolved by the Gaussian assumption of the PDF. q-space, a term first introduced by Callaghan [52]. Each acquisition point in q-space refers to a DWI acquired at that specific value of the wave vector q (in terms of both magnitude and direction). The wave vector q is directly proportional to the gradient vector g (which again has both magnitude and direction) and is given by the following equation,

$$q = \gamma\delta g \tag{2.18}$$

where γ is the gyromagnetic ratio, δ is the duration of the diffusion gradient pulse and $|g|$ is the applied gradient strength.

q is also related to the b-value (introduced in earlier sections) as follows,

$$b = |q|^2(\Delta - \frac{\delta}{3}) \tag{2.19}$$

DSI requires sampling the q-space on a 3D Cartesian grid using the Stejskal and Tanner pulse sequence (described in the earlier sections) with much smaller duration δ, to encode the phase of spin displacements in the diffusion time τ. DSI formulism [17] is based upon

the well established Fourier relationship between the PDF $P(R, \tau)$ and the modulus q-space

signal $S(q, \tau)$ [52-54] and may be expressed using the following Fourier ($\mathcal{F}$) notation,

$$P(R, \tau) = S_0 \mathcal{F}[S(q, \tau)] \qquad (2.20)$$

Hence, the diffusion propagator $P(R, \tau)$ may be recovered using the 3D Fourier

Transform of the DWI signal $S(q, \tau)$ with respect to the gradient wave vector q. In practice,

the modulus of $S(q, \tau)$ is used to exclude the phase shifts arising from tissue motion. Since

the propagator is calculated by Fourier transformation of a measured quantity (diffusion in

this context), $P(R, \tau)$ is referred to as the "diffusion spectrum" and the technique of imaging

using this phenomena is called Diffusion Spectrum Imaging (DSI).

Finally, the PDF (although could be visualized using an isosurface) is commonly

visualized with an orientation distribution function (ODF) which is less sensitive to noise

than the isosurface representation [41]. The PDF is used to estimate ODF by performing a

radial summation of the 3D PDF in accordance with the following formula [13, 15, 17]:

$$ODF = \int PDF \, (ru) \, r^2 dr \qquad (2.21)$$

where, u are the ODF analysis directions and r is the distance along which the integration is

performed. In essence, the area under the curve is computed in each radial direction of the

PDF to estimate the corresponding ODF. ODF thus provides an estimation of multiple fiber

crossings of the underlying fiber structures. An ODF may be considered as a deformed

sphere [41] in which deformation in a given direction is proportional to the integral of the

area of the PDF values in that direction. The ODF surface is color coded according to the

direction of diffusion.

2.8 Alternative strategies and models for high angular resolution diffusion imaging (HARDI)

In diffusion MRI, obtaining the ODF (which has the potential to provide multiple fiber crossings of the underlying fiber structures) is of primary importance. In attempts to save acquisition time and limit hardware requirements, several alternative high angular resolution diffusion (HARDI) models and techniques have been introduced in the literature. Each of these have certain assumptions. These alternate strategies and models include q-Ball imaging (QBI) [13]; spherical deconvolution (SD) and constrained spherical deconvolution (cSD) [32, 55-57]; multi shell QBI [58]; Composite hindered and restricted model of diffusion (CHARMED) [59]; diffusion orientation transform (DOT) [60, 61]; generalized DTI [62], higher order tensors [63], multi Gaussian, multi tensor [64]; Hybrid diffusion imaging (HYDI) [65]; Wishart distribution [66-68]; Von mises-fisher mixture model (vMF mixture model) [69]; persistent angular structure (PAS) MRI [70, 71].

DSI [12, 15, 17, 22, 26, 29, 34, 41, 72] , however, holds the promise to characterize and quantify the PDF without any assumptions about the underlying diffusion processes. DSI is the central theme of this thesis and detailed theoretical description of DSI including post processing is provided in Chapter 4.

CHAPTER 3: Design and Development of Diffusion Phantoms

3.1 INTRODUCTION

Phantoms are extensively used for validation, evaluation, quality assurance and quality control of various imaging modalities including computed tomography (CT), Positron emission tomography (PET), X-ray, Fluoroscopy, Ultrasound (US) and MRI. American college of radiology (ACR) currently provides a physical head phantom for MRI consisting of numerous structures designed to assess several image quality standards of the MRI scanner. However, it has not been standardized and does not (to date) provide a "fiber diffusion phantom" which is essential to validate high angular resolution diffusion imaging techniques such as DSI.

Diffusion phantoms with known structure and geometry offer the possibility of establishing a gold standard to evaluate quantitative diffusion parameters and fiber tractography algorithms. In particular for validating high angular resolution diffusion imaging techniques such as DSI, which aim to resolve crossing fibers, a physical phantom with a known crossing-fiber configuration is essential. These phantoms can also be used for testing new diffusion MRI sequences.

This chapter focuses on the development of phantoms for validating diffusion MRI. Various published diffusion phantoms in the literature with their respective materials, design principles, advantages and disadvantages are reviewed. Motivation for developing the phantoms for DSI validation is described. The diffusion phantoms based on hollow

capillaries developed in this work are then presented in details including their conceptualization, design methodology, and physical construction.

3.2 Diffusion phantoms in published Literature

A wide variety of physical diffusion phantoms have been proposed in the literature using various materials and methods, which I broadly categorize in 4 different types. For each category, I review relevant studies, provide references and highlight their key advantages and disadvantages:

3.2.1   Type 1: Biological phantoms

Numerous biological substances have been utilized for DW-MRI calibration and validation. These may be subcategorized into fibrous vegetables or excised tissues.

The first category amongst biological phantoms is fibrous vegetables based phantoms. Two examples of this type include asparagus [73] and celery[74]. Asparagus has been used to test restricted diffusion [73]. Asparagus is known to exhibit anisotropic diffusion resembling brain white matter. Asparagus thus presents an opportunity to have a good comparison to the in-vivo diffusion and may be a good test object for diffusion tensor tractography. Celery also has anisotropic diffusion [74]. The advantages of using vegetables and plant stems are that they are readily available and no physical construction of phantoms is needed. However, the disadvantages are that they have unknown ground truth configuration and it is not possible to arrange them in complex crossing fiber configurations. Also, since they are biodegradable, they lack durability and reproducibility. Finally, they have limited preservability and their properties are very much dependent upon the storage conditions.

The second category is excised tissue based phantoms. Several variety of this category are reported in the literature and include rat spinal cord [75-78], rat brain [26, 79], mouse myocardium [80], bovine myocardium[81], macaque post-mortem fixed brain [22, 82], bovine tongue [27, 83, 84], cat cerebellum and visual cortex [24, 85]. The main advantage of biological excised tissue is that their structure is very similar to the in vivo situation. However, their underlying structural configuration is also unknown and reliant upon histological comparison. In addition, their preparation requires specialized knowledge and is difficult to obtain and handle during acquisition. In addition, their properties may not be guaranteed to stay constant over time and special storage and handling are needed.

3.2.2   Type 2: Textile fiber phantoms

Several synthetic textile fiber materials have been reported in the literature to create hardware diffusion phantoms. The primary materials reported in the literature are linen [86]; rayon [39]; polyamide [87]; polyester [37]; polyethylene [38, 88]; dyneema [36, 38, 86, 88-90]; acrylic fibers [35] and hemp [86]. The advantages of these textile fiber materials are that they have a very small diameter of up-to 10 μm (close to axonal diameters). Also it is possible to create predefined crossing fiber configurations, including tortuous geometries. Finally, their properties can be maintained reasonably constant over time. However, it is very difficult to achieve and maintain a desired orientation with textile fibers, and they often require employing heat shrink to hold the fibers in place which leads to an inaccurate fiber density and increased uncertainties in the underlying geometry. Finally, they lack the desired tubular geometry;

3.2.3   Type 3: Glass capillaries

Glass capillaries have been used to make phantom [91]. They have the advantage that the underlying structural configuration is precisely known since the glass keeps a very well defined geometry and hence extremely precise angular orientation is achievable. However, glass cannot be bent or manipulated to achieve complicated white matter geometries such as fiber crossing. Also, they have a relatively larger inner diameter (23-80 μm) than textile fibers and their properties can be maintained reasonably constant over time.

3.2.4   Type 4: Fused silica capillary tubing

Fused silica capillary tubing were used in few studies [34, 56, 92]. These capillary tubing are manufactured by Polymicro Technologies, Inc. The main advantage is that with these tubing, a very small internal diameter of 20 μm is achievable. Also, precise angular orientation and known underlying configuration is achievable because these are very rigid capillaries. However, the main disadvantage of fused silica capillary tubing is that they are very fragile and difficult to work with. In addition, they cannot be bent (or they will break). Hence, tortuous geometries cannot be accomplished. A minor disadvantage is that it is very difficult to visualize filled water.

3.2.5   Type 5: Hollow plastic capillaries

Few studies have reported constructing phantoms with hollow plastic capillaries [26, 93]. These are manufactured by Cole Parmer, Inc. The main advantage of capillary tubing is that the water is filled by gluing the capillary on a needle and syringe and hence it is very reliable, unlike the textile fiber phantoms which depend solely upon the water trapped in between synthetic fiber material which may be unreliable. In addition, hollow capillary tubing is able to hold their orientation because of which precise angular orientation is

achievable and can be maintained. In addition, tortuous geometries can be achieved. Furthermore, they have the desired tubular geometry and the underlying structural configuration is precisely known. Finally, their properties can be maintained reasonably constant over time since they are chemically inert. The disadvantage of hollow plastic capillary tubing is larger inner diameter (50 µm) than typical axons and a large wall thickness (350 µm o.d.) which results in a lower packing density leading to a low SNR.

3.3 Motivation to build new crossing fiber diffusion phantoms

Majority of the diffusion fiber crossing phantoms reported in the literature are constructed using textile fibers, which depend upon the signal from the water protons trapped in between synthetic fiber material and may be unreliable. Furthermore, it is difficult to achieve and maintain a desired orientation with these textile fibers. Also, they lack the desired tubular geometry. In order to pack the fibers densely and homogeneously while maintaining orientation and simultaneously increasing the packing density, such phantoms generally employ heat shrink tubes [36, 37] or a fiber tightening mechanism[38, 39]. Such design mechanisms leads to inaccuracies in fiber density and introduces uncertainty in the underlying geometry. Hollow capillary tubing is advantageous for this reason. However, one of the main disadvantages of the hollow capillary tubing reported in the literature is large wall thickness (350 µm o.d.) which results in a lower packing density leading to a low SNR. Note that the hollow capillary tubing utilized in the phantoms developed in this thesis is novel. These capillaries are custom ordered and manufactured (by Zeus Inc. Orangeburg, South Carolina) to achieve a smaller wall thickness (100 µm wall thickness as opposed to previously reported 300 µm). Thus a higher packing density than the previously reported

hollow capillary phantoms in literature could be obtained with a concomitant improvement in the SNR.

Moreover, the diffusion phantoms in the literature were designed only with two crossing fibers, mostly consisting of a very small homogeneous region of crossing fibers and are rather simplistic for validation purpose. A careful investigation using a three fiber crossing phantom that is anatomically relevant is essential for validation of DSI and other HARDI techniques since such fiber crossings are encountered in multiple brain regions (for eg. in centrum semiovale region where 3 fibers from corpus callosum, corona radiata and superior longitudinal fasciculus intersect and cross). A recently published coronal brain slice phantom[94] (again constructed using synthetic fibers) has a small section containing fibers splitting in three directions. However, in this phantom, 1) the fibers represent "splitting" and not "crossing" and 2) have a very limited region consisting of three fibers. Therefore, a novel diffusion phantom consisting of three interleaved crossing fibers is designed and constructed in this thesis. Two additional phantoms consisting of two crossing fibers at 45° and 90° crossings were built to gain experience in handling the proposed material, winding procedure and verify the overall phantom construction workflow as a first pass, before embarking on the more complicated three crossing fiber configuration construction.

3.4 METHODS (Phantoms construction)

Overall, the phantom construction in this work involved hollow plastic capillaries which were filled with distilled water and wrapped around a plastic plate to form a number of interleaved parallel layers resulting in fibers crossing at the desired angle. There are three

general criterions that need to be considered in the phantom construction, and should conform to the primary purpose of the phantom. These are 1) Basic design; 2) Fiber type and material and 3) Medium in which the tubing is inserted. These are detailed in the following subsections with regards to phantom construction in this thesis.

3.4.1   Basic Design

Since the overall purpose of this phantom was to validate DSI derived angular information, a simple 90°, two-way crossing fiber phantom with interleaved configuration was designed and constructed to validate the overall manufacturing procedure approach. Fig.3.1 presents the design theme for the 90° phantom. This design theme is similar to that presented in [26]. The capillaries were carefully placed on top of each other to form parallel layers in an interleaved manner.
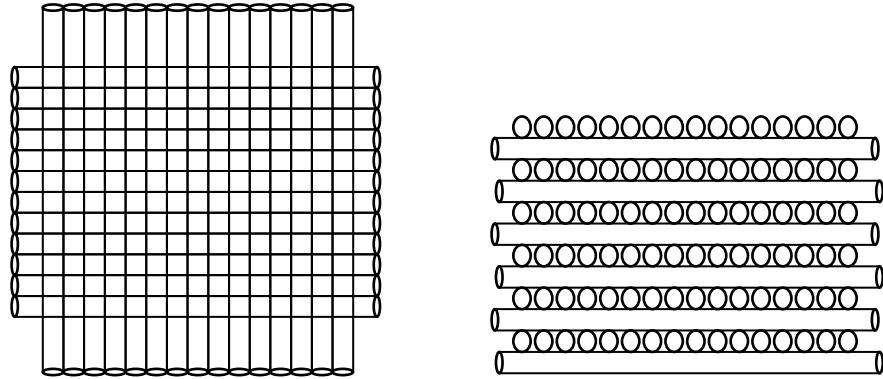
Fig.3.1: Design Theme for 90° Phantom. Capillaries were carefully placed on top of each other to form parallel layers in an interleaved manner (similar to [26]).

This design theme was mechanically realized by designing and constructing a placeholder having a precise angle with a very low tolerance (90°±0.001°). The design was performed with Rhino 4.0 (Robert McNeel & Associates) and realized using machine shop.

[27]

The material used to realize the placeholder was solid wax (which was tested negative for any possible MRI signal). The constructed placeholder is depicted in Fig.3.2. The dimension of the central crossing region was 20 mm x 20 mm.
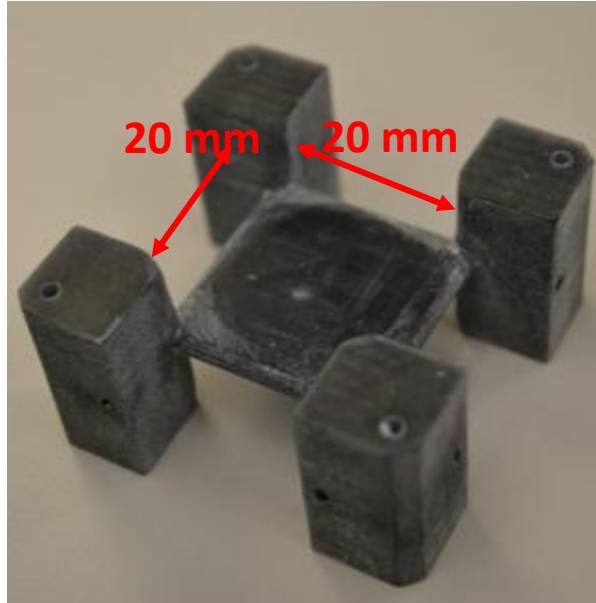
Fig.3.2: Constructed Placeholder for 90° Phantom.

3.4.2   Fiber type and material

Custom ordered hollow plastic capillaries (manufactured by Zeus Inc.) are depicted in Fig.3.3. The capillary tubing have inner diameter (i.d. = 50 µm); outer diameter (o.d. = 150 µm); wall thickness = 100 µm; total length = 500 ft. The outer diameter was smaller than the previously reported hollow capillary phantoms [26] which allowed a high packing ratio, leading to a high SNR.

Fig.3.3: Hollow PTFE ultra-micro-bore tubing. Hollow plastic capillaries with smaller outer diameter than previously reported hollow plastic capillaries.

As outlined in fig.3.4, one end of the hollow capillary was glued onto a 27 G needle which was mounted on an automatic syringe pump (NE-1000 Programmable Syringe Pump) for water filling. Water was lightly doped with Food coloring agent: Blue #1 (also called Brilliant Blue FCF, E#133, Color Index: 42090 - C37H34N2Na2O9S3) for visualizing water inside the tubing. This doping has negligible impact on the relaxation properties. The total volume of water required to fill 500 ft of tubing was about 300 µL. With a constant pressure= 10 µL/hr, pure distilled water (marked with the blue coloring agent for visualization with naked eye) was pumped in the entire 500 ft. length of tubing using the automatic syringe pump and took about 30 hours to fill entirely.

[29]
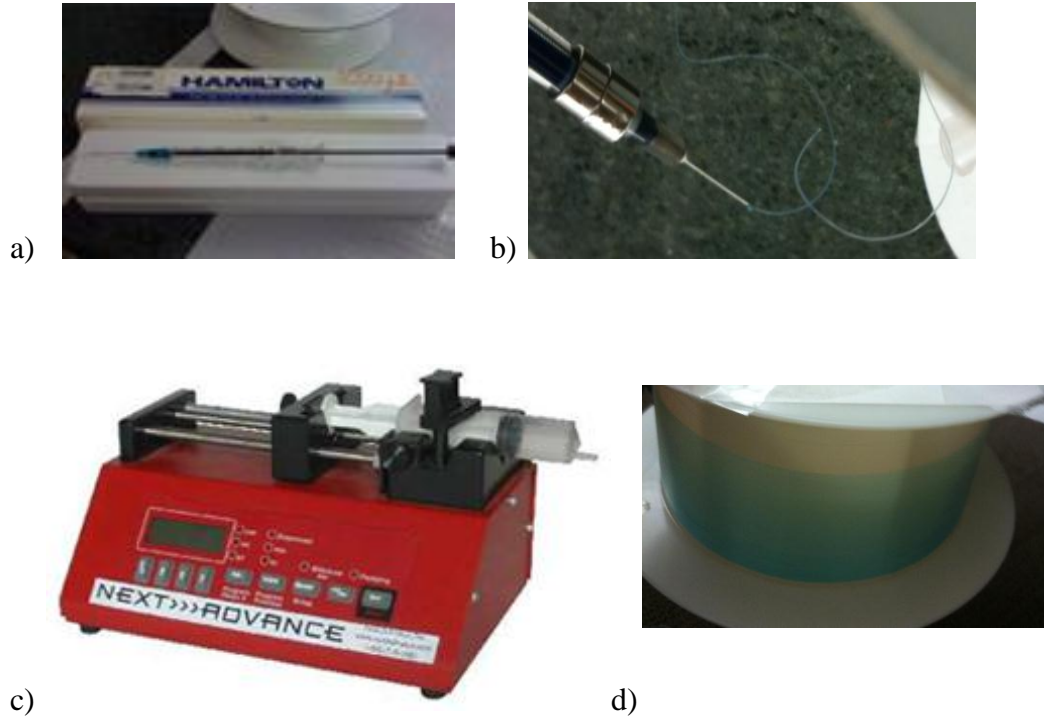
Fig.3.4: Water Filling Setup. (a) 27G needle; (b) One end of capillary was glued to the needle; (c) Water was filled in capillaries using a syringe pump; (d) Water filled capillary.

After observing that the water is indeed retained over a period of 2 weeks, the water filled capillaries were then wrapped around the designed plastic base using in-house manufactured semi-automatic winding machine. The wrapping of the tubing was manually guided to ensure that they are wrapped right next to each other without gap or overlap. If an error was made, the machine was re-winded and tubing was re-wrapped until a near perfect layout was achieved. The photograph of the completely wrapped 90° phantom is shown in Fig.3.5.
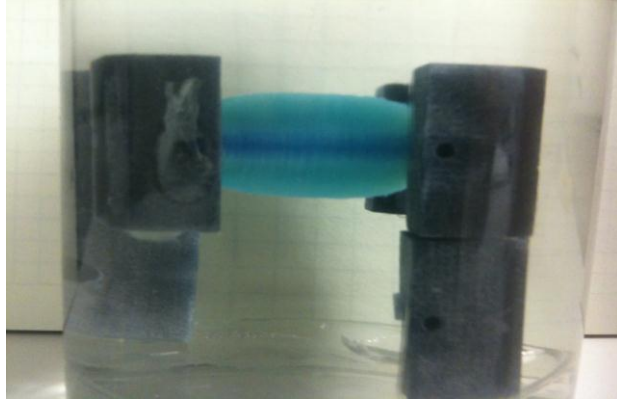
Fig.3.5: Completed 90° Phantom With Wrapped Capillaries.

3.4.3   Medium in which the tubing is inserted

Usually, agar gel or pure water is chosen since otherwise air would cause strong susceptibility gradients at the air-water interface, resulting in distortions in the EPI Images. I did not choose gel because it creates sticky interfaces and is hard to take apart if further design modifications are needed. I also did not use pure water since it would not be possible to confidently distinguish between the signal coming from water inside the tube and the water surrounding the tubes. Therefore, I used water heavily doped with $MnCl_2$. This heavily doped $MnCl_2$ eliminated any signal coming from outside medium and ensured that any diffusion weighted signal received was coming only from the water in tubes. The entire assembly was degassed and sonicated to remove trapped air bubbles.

3.5 RESULTS (phantom construction)

3.5.1   90° Phantom

The photograph of the completed 90° phantom is shown in Fig.3.6. The dimensions of the crossing region of the completed 90° phantoms were: x=20 mm, y=20 mm, z= 4.2 mm each side (corresponding to 28 interleaved layers each side). The resultant slice thickness was slightly greater than the theoretically calculated slice thickness due to lesser number of turns at the edges. This was done deliberately to avoid wrapping of the tubes around the sharp edges to avoid any possible rupturing of the capillary tubing.

Fig.3.6: Photograph of the Completed 90° phantom.

3.5.2   45° Phantom

After confirming the results on the 90° Phantom, an additional configuration was designed and constructed similarly consisting of a 45° (Fig.3.7), two-way crossing fiber phantom with interleaved configuration. This was to study the effect of reducing the angle between the crossing fibers, before embarking upon the more complicated 60° phantom construction. The 45° phantom was constructed using the same 500 ft. length tubing. However, given the design requirement to form a 45° configuration, a trade-off between the available length of tubing and the achievable crossing region cross-section at a given slice thickness had to be made. The dimensions were optimized as follows: x=15 mm, y=35 mm, z= 3.3 mm each side (corresponding to 22 interleaved layers each side). The photograph of the completed 45° phantom is shown in Fig.3.8.
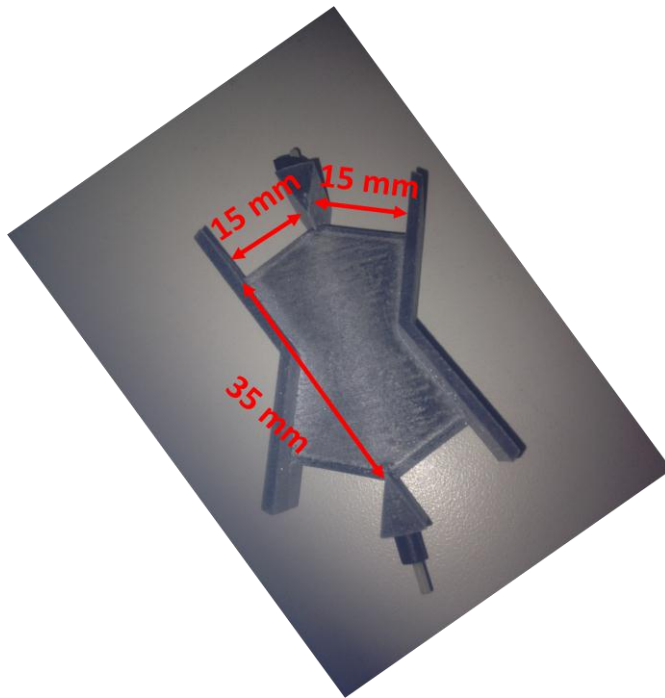
Fig.3.7: Constructed Placeholder for the 45° Phantom.

[33]
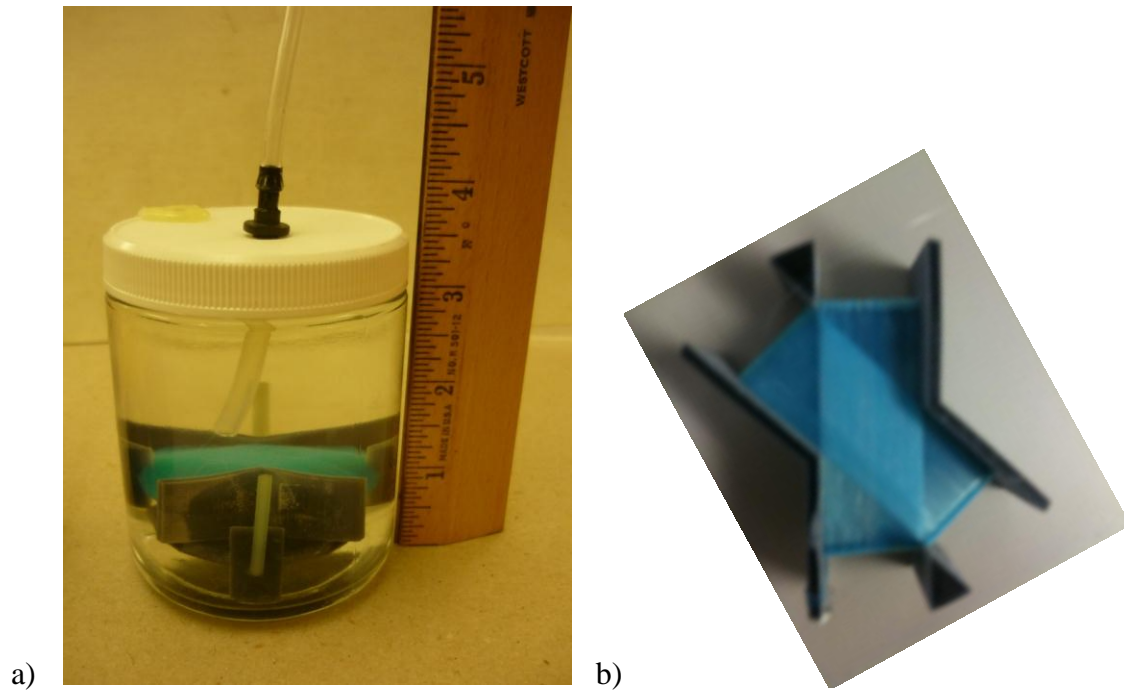
Fig.3.8: Photograph of Completed 45° Phantom. (a) Photograph of the phantom (b) Axial View of the completed phantom with wrapped capillaries.

3.5.3 60° Phantom

Finally, a 60°, three-way crossing fiber phantom with interleaved configuration was similarly designed (Fig.3.9 a) and constructed (Fig.3.9 b).

a)

b)
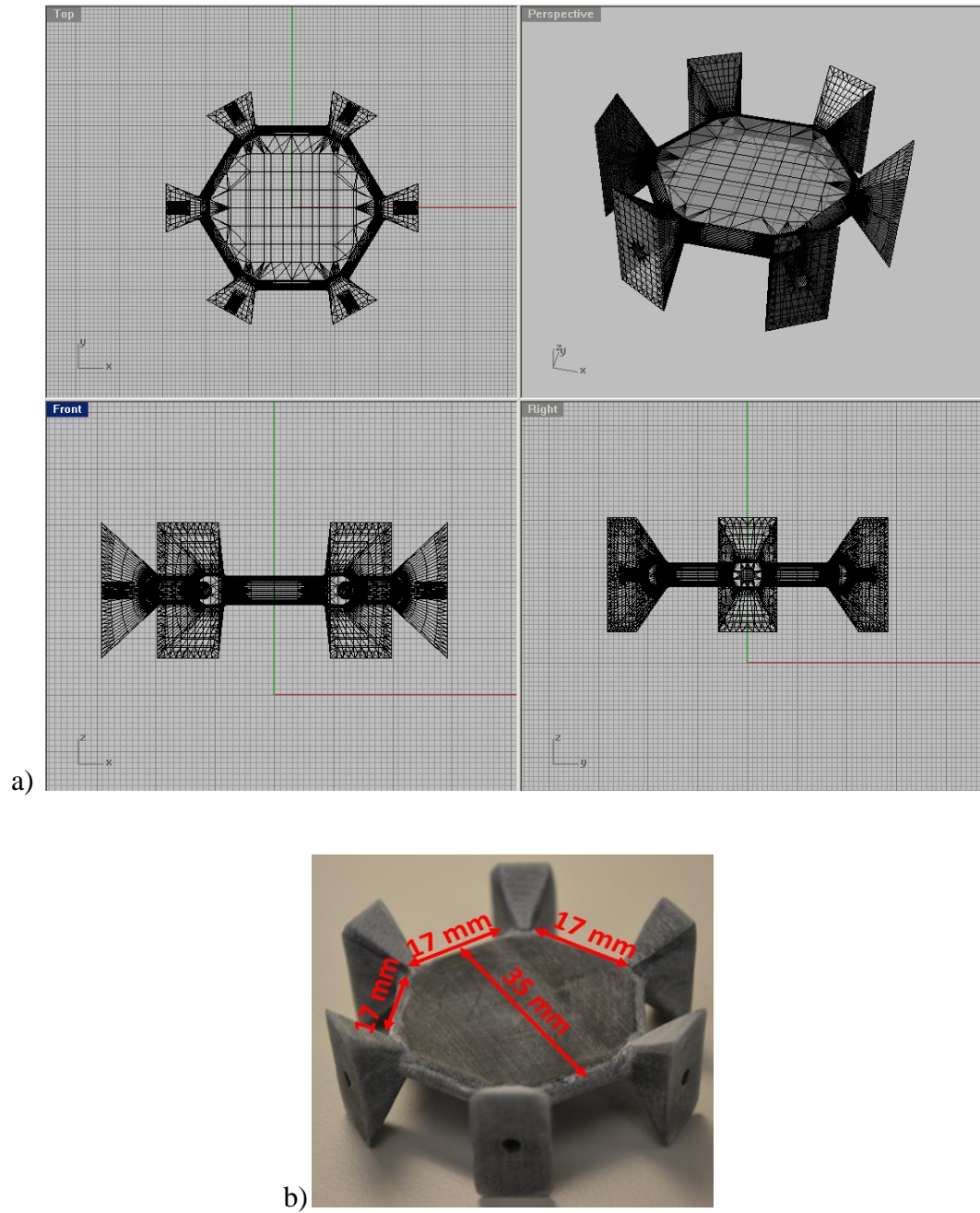
Fig.3.9: 60° Phantom Placeholder. (a) Design theme and (b) constructed placeholder.

To construct the 60° phantom, 1000 ft. tubing was used (instead of 500 ft. used for the other two phantoms). Again, a trade-off between the available length of tubing and the achievable crossing region cross-section at a given slice thickness had to be made. The dimensions were optimized as follows: x=17 mm, y=37mm, z= 3.85 mm each side (corresponding to 25 interleaved layers each side). The photograph of the completed 60° phantom is shown in Fig.3.10.

a)   b)
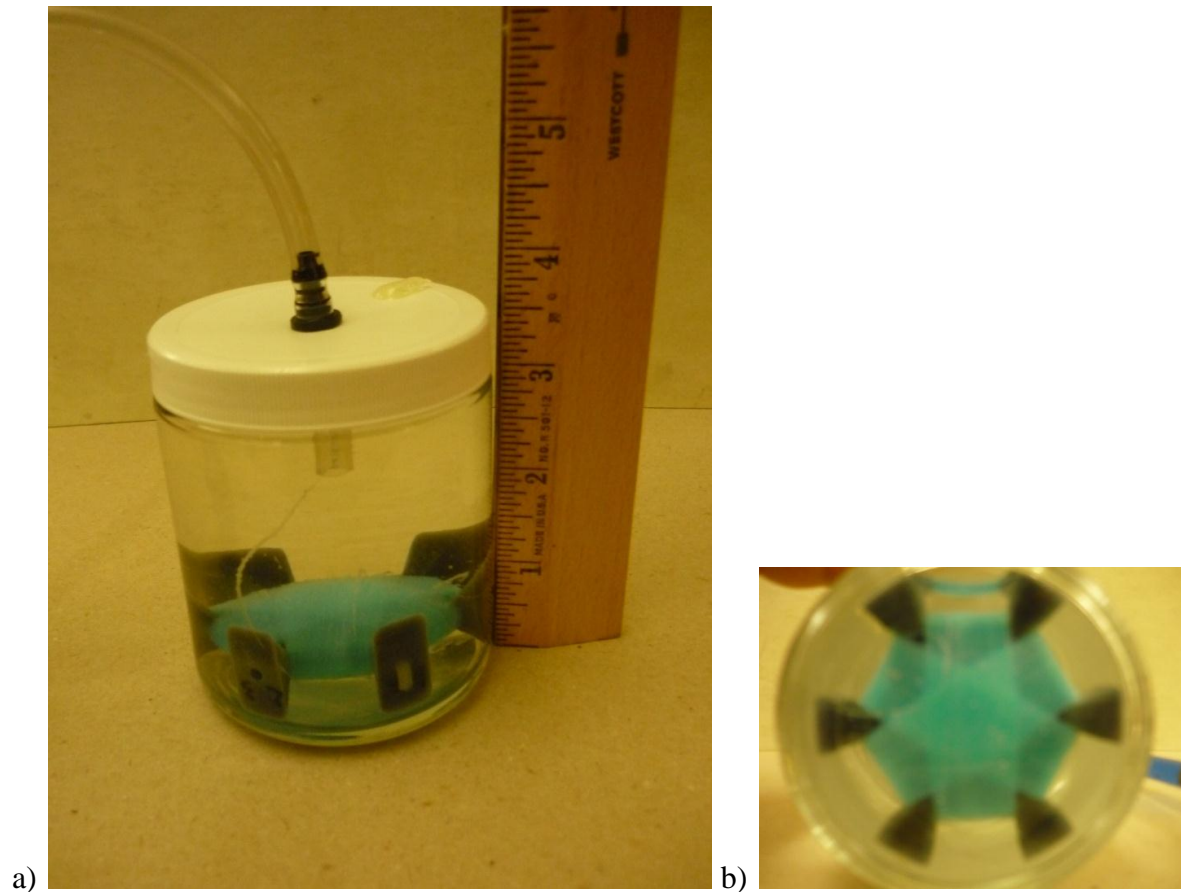
Fig.3.10: Photograph of Completed 60° phantom. a) Photograph of the Completed

Phantom (b) Axial View.

3.6 METHODS (MRI Acquisition)

MRI data was acquired on all the phantoms on a Philips 3.0 T Intera scanner (Achieva, Philips Medical Systems, Best, Netherlands) with a maximum gradient amplitude of 80 mT/m and a slew rate of 200 mT/m/ms An 8 channel SENSE FLEX coil was used for data acquisition. A high resolution T2 weighted image was acquired on each phantom using a T2-TSE (Turbo Spin Echo) T2-w sequence with the following sequence parameters: TE/TR=100/5000 msec; FOV=120x120 mm2; Matrix=512x512; Spatial Resolution= 0.234x0.234 mm/px; ΔTH=4 mm; NEX=8; Acq and took 6 min 45 sec for acquisition. In addition DSI data was also acquired, whose details are provided in the subsequent chapter after presenting the detailed analysis flowchart and deconvolution methodology.

3.7 RESULTS (MRI Acquisition)

Representative slice (from a crossing region) of T2-weighted image of the 90°, 45° and 60° Phantoms are shown in Fig.3.11, Fig.3.12, and Fig.3.13 respectively. T2 weighted images show good SNR, homogeneous signal and absence of air bubbles.
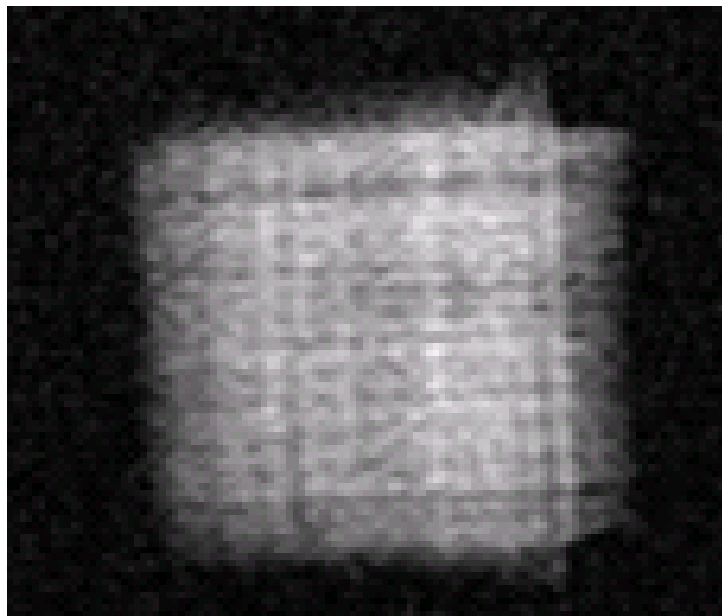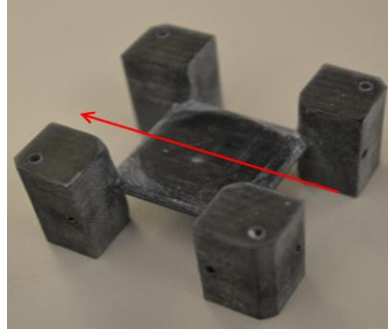
Fig.3.11: T2-weighted Image of 90° Phantom. Representative slice from crossing region.
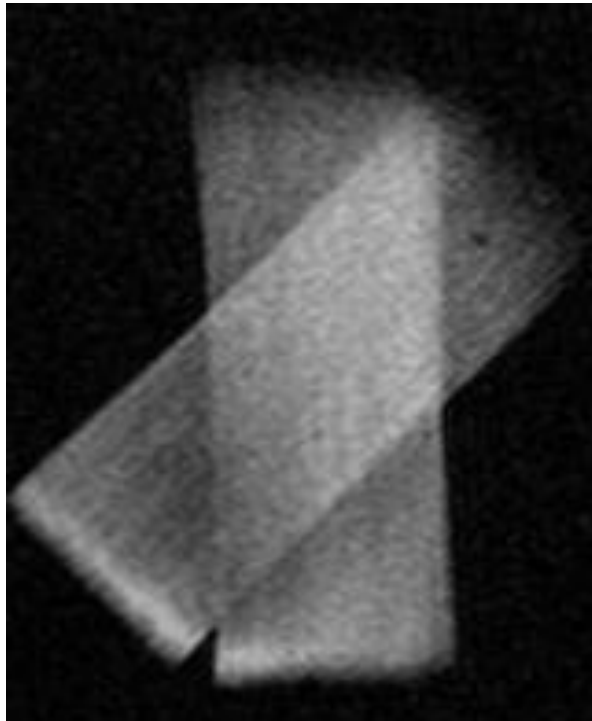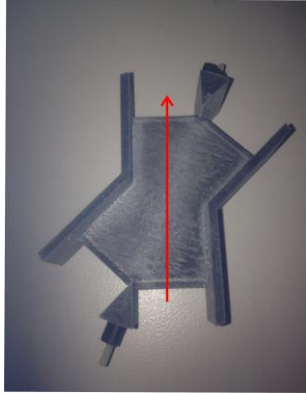
Fig.3.12: T2-weighted Image of 45° Phantom. Representative slice from crossing region.
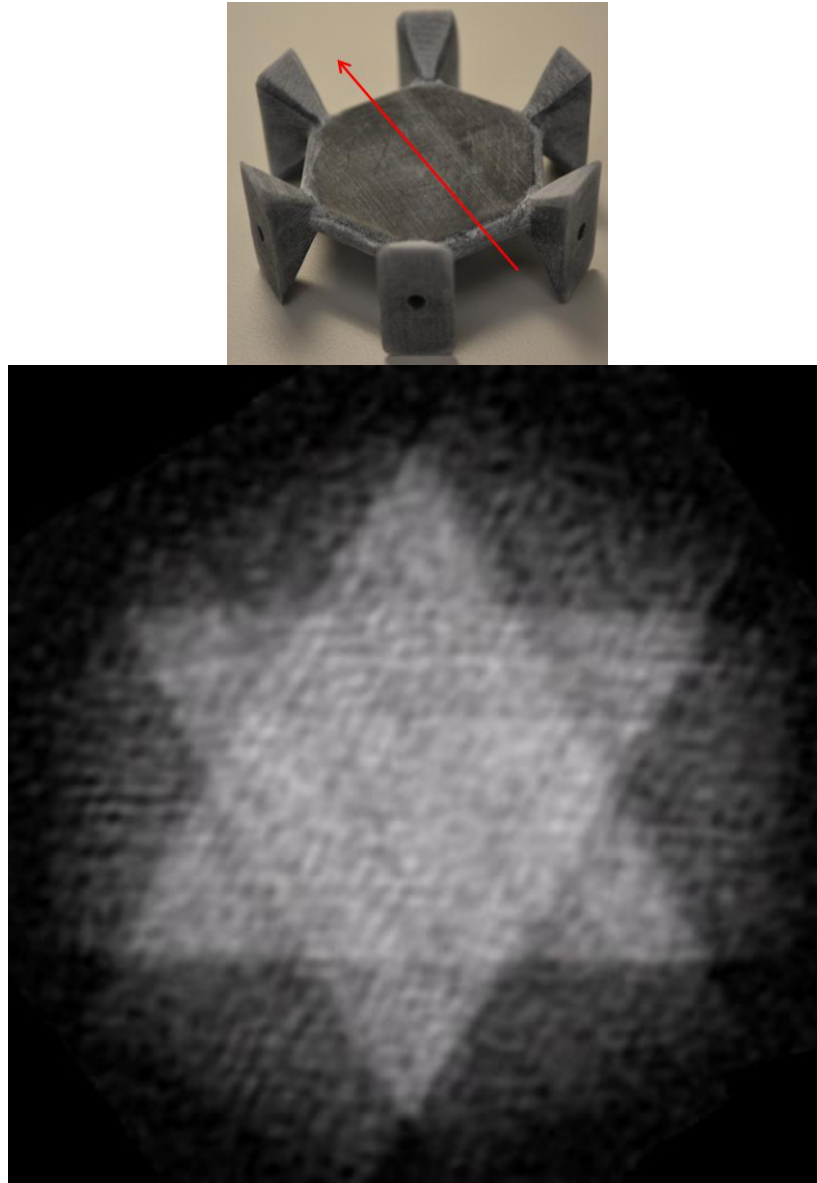
Fig.3.13: T2-weighted Image of 60° Phantom. Representative slice from crossing region.

3.8 SUMMARY

The phantom developed in this thesis utilizes novel hollow capillary tubing designed to obtain a higher packing density than the previously reported hollow capillary phantoms. Also, a novel diffusion phantom consisting of three interleaved crossing fibers is designed and constructed. Two additional phantoms consisting of two crossing fibers at 45° and 90° crossings are also constructed. The developed phantoms offer a means of providing ground truth for validation of various diffusion models (particularly the ones that aims to resolve the crossing fibers) and for validation of tractography algorithms. The utility of these phantoms in evaluating angular accuracy of DSI is presented in Chapter 5.

CHAPTER 4 – Post Processing Deconvolution in DSI

4.1 INTRODUCTION

Diffusion-weighted images (DWIs) are typically acquired using an Echo Planar Imaging (EPI) sequence with a small matrix size to reduce the acquisition scan time.

Following the acquisition of the k-space data, as a part of the image reconstruction by the scanner computer, mathematically the k-space is filled for the missing points, filtered, interpolated, and inverse Fourier transformed to create the DWIs. .The resultant DWIs still need further processing in order to extract diffusion metrics [95]. These post-processing operations generally include, but are not limited to, distortion correction [96, 97] (both eddy current and susceptibility related), registration [97-104] of non diffusion-weighted and diffusion-weighted (both linear and non-linear), motion correction [105-110] and de-noising [111-114].

There are additional processing steps involved in the orientation distribution function (ODF) based diffusion-weighted MRI methodologies (such as DSI and HARDI) in which the directional information of diffusion is inferred from the ODF peaks. The challenge is that ODF may yield inaccurate orientation information in regions where fibers cross at relatively acute angles because each contributing fiber bundle generates a peak with finite width. This makes it difficult to resolve the true peaks in the ODF [12, 31, 32, 115]. This chapter deals with the post-processing steps to help resolve the ODF peaks. Specifically, a

de-convolution based technique applicable to DSI derived ODFs is described and implemented. In the following sections the current DSI analysis methodologies are described and their limitations are pointed out. The theoretical background necessary for understanding this methodology is also described.

4.2 Post-processing methodology in DSI and associated technical challenges

DSI formulism is based upon the well established Fourier relationship between the diffusion spectrum and the modulus q-space signal. DSI require sampling the DWIs on a 3D Cartesian grid using the Stejskal and Tanner pulse sequence (described in Chapter 2) which encodes the phase of spin displacements in the diffusion time τ by employing a pair of opposite polarity diffusion gradient pulses of strength g and duration δ.

The sampled MR q-space signal $S(q, \tau)$ is thus made proportional to the voxel average dephasing (φ) of the spins (during the experimental duration τ). Mathematically,

$$S(q, \tau) = S_0 < exp(i\varphi) > \tag{4.1}$$

where $(<.>)$ represents voxel average and S_0 is a constant and represents the spin echo signal obtained without any diffusion encoding gradients. q is the diffusion wave vector given by

$$q = \gamma \delta g \tag{4.2}$$

where γ is the gyromagnetic ratio, δ is the duration of the diffusion gradient pulse and g is the applied gradient strength.

[43]

Under the narrow pulse approximation ($\delta \ll \tau$), the voxel averaged dephasing φ may be approximated as the dot product of the gradient wave vector q and the relative displacement vector R.

Mathematically,

$$\varphi = q.R \tag{4.3}$$

The relative spin displacement (R) may be thought of as the difference of the spin positions. Mathematically,

$$R = \text{x}(\Delta) - \text{x}(0) \tag{4.4}$$

where $\text{x}(0)$ represents the spin position at the application of the first diffusion gradient pulse and $\text{x}(\Delta)$ represents the spin position at the application of the second diffusion gradient pulse.

Hence, the voxel average may be considered as a displacement probability distribution of the spins in the time τ and may be represented by a diffusion propagator $P(R,\tau)$ which represents the probability of a spin to make a vector displacement R in the given experimental mixing time τ. Considering the 3D probability of spin displacement, Eq.4.1 may be reformulated as,

$$S(q,\tau) = S_0 \int_{R^3} P(R,\tau) \, exp(i \, \varphi) \; d^3R \tag{4.5}$$

Substitution the formulism for φ from Eq.4.2,

$$S(q,\tau) = S_0 \int_{R^3} P(R,\tau) \, exp(i \, q.R) \; d^3R \tag{4.6}$$

Thus the signal equation takes the form of a Fourier relationship between

$P(R,\tau)$ and $S(q,\tau)$. Hence $P(R,\tau)$ can be obtained by the Fourier Transformation of $S(q,\tau)$, as follows:

$$P(R,\tau) = S_0^{-1} \int_{R^3} S(q,\tau)\,exp(-2\Pi\,i\;q.R)\;d^3q \tag{4.7}$$

(note the change of variables inside the integral)

Finally, this relationship may be expressed using the following Fourier ($\mathcal{F}$) notation,

$$P(R,\tau) = S_0\mathcal{F}[S(q,\tau)] \tag{4.8}$$

Hence, the diffusion propagator $P(R,\tau)$ may be recovered using the 3D Fourier Transform of the DWI signal $S(q,\tau)$ with respect to the gradient wave vector q. In practice, the modulus of $S(q,\tau)$ is used to exclude the phase shifts arising from tissue motion.

Since the propagator is calculated by Fourier transformation of a measured quantity (diffusion in this context), $P(R,\tau)$ is referred to as the "diffusion spectrum" and the technique of imaging using this phenomena is called Diffusion Spectrum Imaging (DSI).

$P(R,\tau)$ is also generally referred to as the Probability Distribution function (PDF). A flowchart of the key components in the DSI analysis [17, 26, 29] are depicted in Fig.4.1 and will be elaborated in the following sub-sections. According to [33]there is no consensus in the DSI community on what pre-filtering and pre-processing steps are essential prior to the FFT computation (step 4.2.3 described below). These steps are hence elaborated in further details.
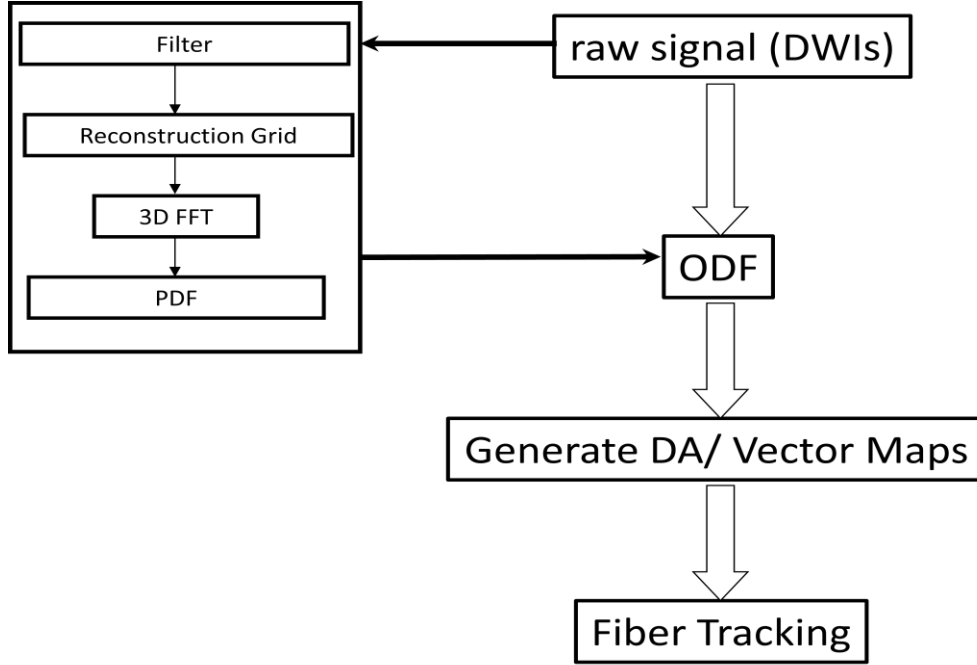
Fig.4.1: DSI Flowchart. ODF is estimated from raw signal after multiple processing steps (see text).

4.2.1 Filtering for de-noising

The most commonly employed de-noising methodology in DSI involves applying a tapering function that is smooth and non-negative with a finite support to ensure smooth attenuation of the signal to zero at the edges of the sampled region. A Hanning window (used frequently to reduce aliasing in the Fourier transforms) is one such tapering function commonly deployed in DSI data processing [17]. The Hanning window is defined as follows:

$$A(\mathrm{x}) = \left(\frac{1}{2}\right)\left\{1 + \cos\left(\frac{\Pi \mathrm{x}}{\mathrm{F}}\right)\right\} \tag{4.9}$$

where F = full width at half maximum and is set to the dimensions of the reconstruction grid

(explained in the following section). A three-dimensional Hanning window is applied to the raw data.

Other methods include setting the diffusion signal to zero if smaller than two times of the mean signal in air and re-gridding the resulting data to a Cartesian lattice using a linear hyper-surface fitting algorithm [116]. Another method is to apply a statistical thresholding technique by fitting a gamma distribution to the resulting 3D image intensities and retaining only those values within 95% confidence intervals, thus neglecting all intensities near the noise floor [33]. There is also possibility of applying wavelet thresholding [33].

4.2.2   Reconstruction Grid

In theory, the diffusion propagator $P(R, \tau)$ is defined by the following 3D integral (rewritten from Eq.4.6) as follows,

$$P(R) = \iiint_{-\infty}^{\infty} S(q) \exp(-2\Pi i Rq) \, d^3q \tag{4.10}$$

where $S(q)$ is the q-space signal, R is the real space vector of the displacement of water molecules, q is the wave vector.

In practice, the q-space is sampled symmetrically within the limits of $\pm q_{max}$ along each Cartesian axis [17]. Hence, Eq.4.10 takes the form of the following definite integral [33]:

$$P(R_x, R_y, R_z) = \iiint_{-q_{max}}^{q_{max}} S(q_x, q_y, q_z) \exp(-2\Pi i (R_x q_x, R_y q_y, R_z q_z) \, dq_x dq_y dq_z \tag{4.11}$$

where $\{R_x, R_y, R_z\}$ are the Cartesian components of the real space vector and $\{q_x, q_y, q_z\}$ are the Cartesian components of the q-space vector.

A typical procedure in DSI analysis is to zero pad the q-space signal in order to increase the reconstruction grid resolution. The reconstruction grid resolution reported in the literature ranges from 7x7x7 [65] to 17x17x17 [17] to 35x35x35 [33]. The propagator is interpolated in order to compute the ODF (subsequent step after FFT) to this spherical lattice and for low-resolution grids which leads to Cartesian artifacts [13]. However, increasing the grid size increases the computational cost.

4.2.3 FFT computation

A discrete 3D Fourier transform is performed on the modulus q space signal (symmetric around the center of q space) to obtain the Probability Distribution Function, (PDF), in accordance with Eq.4.8.

4.2.4 Orientation distribution function (ODF)

The orientation distribution function (ODF) is computed from the PDF by performing a radial summation of the 3D PDF in accordance with the following formulism [13, 15, 17]:

$$\text{ODF} = \int \text{PDF} \, (ru)r^2 dr \tag{4.12}$$

where u are the ODF analysis directions and r is the distance along which the integration is performed. In practice, the ODF is not integrated from zero (i.e. r starts at 2 instead of 0) in order to avoid integrating the isotropic central part of the PDF.

4.2.5 Diffusion anisotropy (DA)

Diffusion anisotropy is a quantitative metric that can be obtained from the DSI data [25]. It can be used to quantify the shape of the PDF and a unique value of DA can be determined from the ODF in each voxel. DA is an indicator of the diffusion anisotropy within each voxel and is formulated as the standard deviation of the normalized ODF [25]. Mathematically,

$$DA = std(\text{ODF}) \hspace{6cm} (4.13)$$

Clearly, the standard deviation (and hence the DA value) is very low for an ODF representing an isotropic ODF (since the ODF is spherical in such regions). On the other hand, the standard deviation (and hence the DA value) is very high for a very well defined ODF such as the one in single fiber regions. The DA value is intermediate (between isotropic and single fiber DA value) in the regions of crossing fibers.

4.2.6 Fiber tracking

The DA and vector map information is used to perform DSI based fiber tracking. Note that in DSI based fiber tracking each voxel can have more than one direction vector for visualizing crossing fibers. The descriptive analysis methodology and parameters used in this thesis work are provided in the Methods section (section 4.5).

4.3 Limitations of DSI methodology and other ODF based methodologies

In the ODF based diffusion weighted MRI methodologies (such as DSI and HARDI) the directional information of diffusion is inferred from the peaks in the ODF. ODF may yield

[49]

inaccurate orientation information in regions where fibers cross at relatively acute angles because each contributing fiber bundle generates a peak of finite width, making it difficult to resolve the true peaks in the ODF [115].

This becomes a specially challenging at low b-values [31] or when the angular resolution of the technique involved is not enough (for example due to low SNR or reduced angular sampling). In such situations, the ODF presents itself as a convolution of the true ODF with a point spread function. It is possible to recover the two peaks by deconvolution techniques if the convolution kernel is correctly identified [31, 33, 34, 60, 115].

It was shown in [33, 60] that because of a finite support of HARDI measurements in q-space, the diffusion propagator obtained is a convolved version of the true propagator with a point spread function (PSF) that can be defined as the Fourier transform of the boxcar function. The effect of computing the diffusion spectrum out to finite q-values is equivalent to multiplying the diffusion signal by a 3D boxcar filter, given by the following equation:

$$\mathbb{III}(q_x, q, q_z) = \mathbb{III}(q_x)\mathbb{III}(q_y)\mathbb{III}(q_z) \tag{4.14}$$

where $\mathbb{III}(q_x, q, q_z) = 1$ if $|q_x| \leq q_{max}$, $|q_y| \leq q_{max}$, $|q_z| \leq q_{max}$, and 0 otherwise.

This formulation can be expressed as a convolution operation $\otimes$ as follows,

Measured Propagator = True Propagator $\otimes \mathcal{F}\mathbb{III}(q_x, q, q_z)$

where the measured propagator is a convolved version of the true propagator with the Fourier transform of the boxcar function (i.e. PSF). Also, [33] pointed out that the convolution between the true propagator and PSF results in a blurred propagator which has a decreased contrast and a lower angular resolution.

In addition, [115] showed how the maxima of a ODF may provide biased or misleading estimates of the underlying fiber structure when the fibers cross at acute angles. As shown in the Fig.4.2 (a), consider two fiber populations coexisting and crossing at an acute angle in an imaging voxel. These are depicted by two different colors (red and blue) in the illustration. Each of these fiber populations results in an ODF peak of finite width (these finite width peaks are illustrated in the corresponding colors in Fig.4.2 b and Fig.4.2 c). The issue is that the ODF is a linear summation of these finite width peaks and if the data doesn't have enough angular accuracy, these peaks combine linearly and the true peaks get masked (as shown in Fig.4.2 d). The resultant ODF (as shown in Fig.4.2 e) thus has only one peak (although it should be depicting two peaks). Notice also, how the resultant peak is not a true representative of either of the two peaks (note: the axes units are arbitrary and are for illustrative purposes only)

This is thus an inverse problem, i.e. given the superimposition of the peaks, how to resolve the true peaks. One of the potential solutions (obviously with certain assumptions) lies in the theory of deconvolution which is covered next.
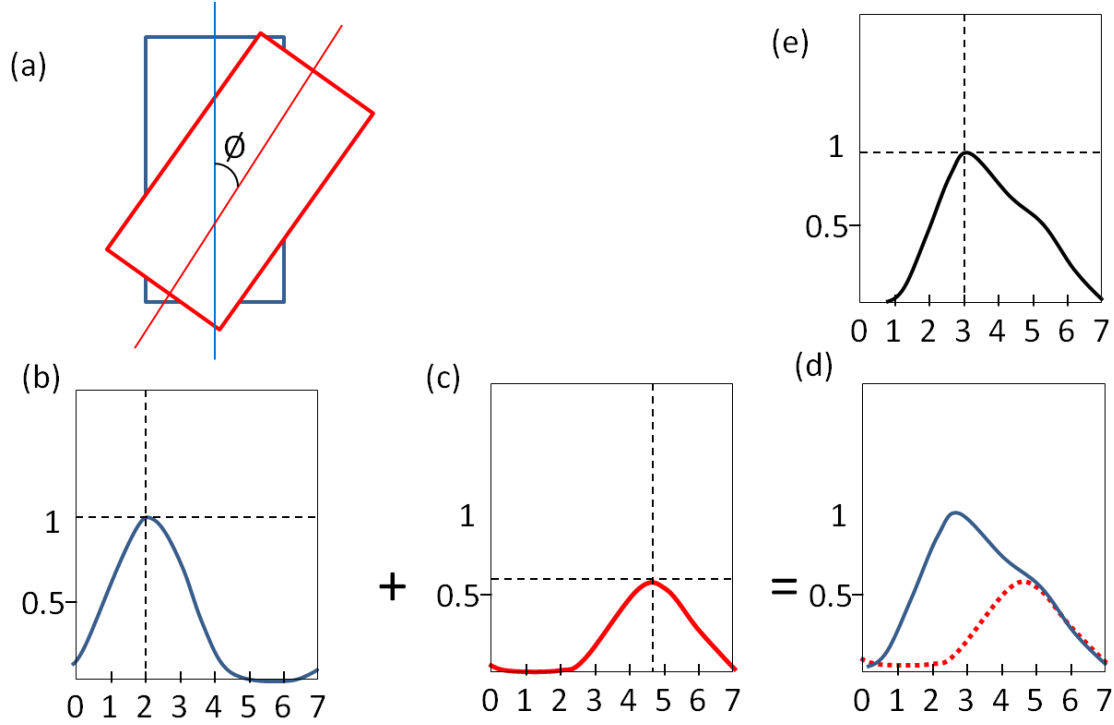
Fig.4.2: ODF Maxima Interference. In the regions of two fibers crossing at a relatively acute angle Ø (illustrated in (a) with red and blue colors), the corresponding ODF profiles from each fiber bundle (shown in red and blue in b and c respectively) superimpose (d) to mask the overall peak (e) which is not a true representative of either of the two underlying fiber populations. (The axes units are arbitrary and are for illustrative purposes only).

4.4 Deconvolution in DW-MRI and DSI

Deconvolution is a core concept in digital signal and image processing and has been extensively applied in the context of medical imaging across all modalities (CT, PET, MRI, Ultrasound). Specifically, the concept of deconvolution as related to this thesis work concerns with diffusion MRI.

In the context of diffusion MRI, spherical deconvolution was first introduced by [32] to directly determine the fiber orientation density function from diffusion weighted MRI data

[52]

[32]. In the methodology of [32] (later refined in [55, 56] using additional regularization) the fiber orientation was directly estimated from diffusion weighted data by transforming the HARDI signal coefficients directly and did not involve any intermediary diffusion framework. Later, [31] utilized the deconvolution concept in q-ball imaging and obtained sharp ODFs by deconvolving the response of single fiber response function from the HARDI signal.

This idea of deconvolution was extended to DSI by [33] in which the true DSI PDF was obtained from measured DSI PDF by deconvolving it with a point spread function defined as the Fourier transform of the boxcar function (as detailed in the previous section). Finally, [34] proposed a deconvolution methodology based on a mixed diffusion model consisting of measured diffusion ODF and a background isotropic diffusion component and obtained a sharper version of the measured ODF by deconvolving a characteristic ODF from the measured ODF by defining a convolution matrix whose column vectors were the characteristic ODFs oriented at a number of orientations.

The deconvolution methodology implemented in this thesis is motivated from these studies and conceptually is similar to [31]. However, according to [34], the methodology in [31] can only be applied to images acquired by the single-shell sampling scheme, and not to data acquired by other sampling schemes. The deconvolution methodology in this thesis is shown to be successful when applied to DSI derived ODFs as a post processing step, leading to detection of valid crossing fibers and in improving the angular accuracy of DSI.

The following sections provide the necessary details on the deconvolution methodology implemented in this thesis. A brief introduction to Spherical harmonics is provided as this is an essential component of the deconvolution methodology utilized in this thesis.

4.5 METHODS

4.5.1 Spherical harmonics

Spherical harmonics Y_ℓ^m are the angular portions of Laplace's equation in spherical coordinates. They are defined as:

$$Y_\ell^m(\theta, \emptyset) = \sqrt{\frac{2l+1}{4\pi} \frac{(\ell-m)!}{(\ell+m)!}} P_\ell^m(cos\theta) e^{im\emptyset} \qquad (4.15)$$

where ℓ is the order and m is the degree.

In the above equation P_ℓ^m represents the Legendre polynomial. The spherical harmonics form a complete orthonormal basis set of functions over the sphere, much like the Fourier series forms a complete orthonormal basis over an interval in Cartesian space [32].

Analogous to the Fourier transform where the bases are sines and cosine function, spherical harmonics form the bases for any complex function defined on a sphere. Thus, similar to the possibility of representing any complex function with sines and cosine functions as their bases, a complex function on the sphere can be expressed as a series of spherical harmonics as their bases. In the case of an ODF computed by DSI, which is a function represented by deforming the unit sphere, it is possible to represent it as a linear summation of spherical harmonic bases[31].

$\ell = 0$

$\ell = 2$

$\ell = 4$

m = -4   m = -3   m = -2   m = -1   m = 0   m = 1   m = 2   m = 3   m = 4
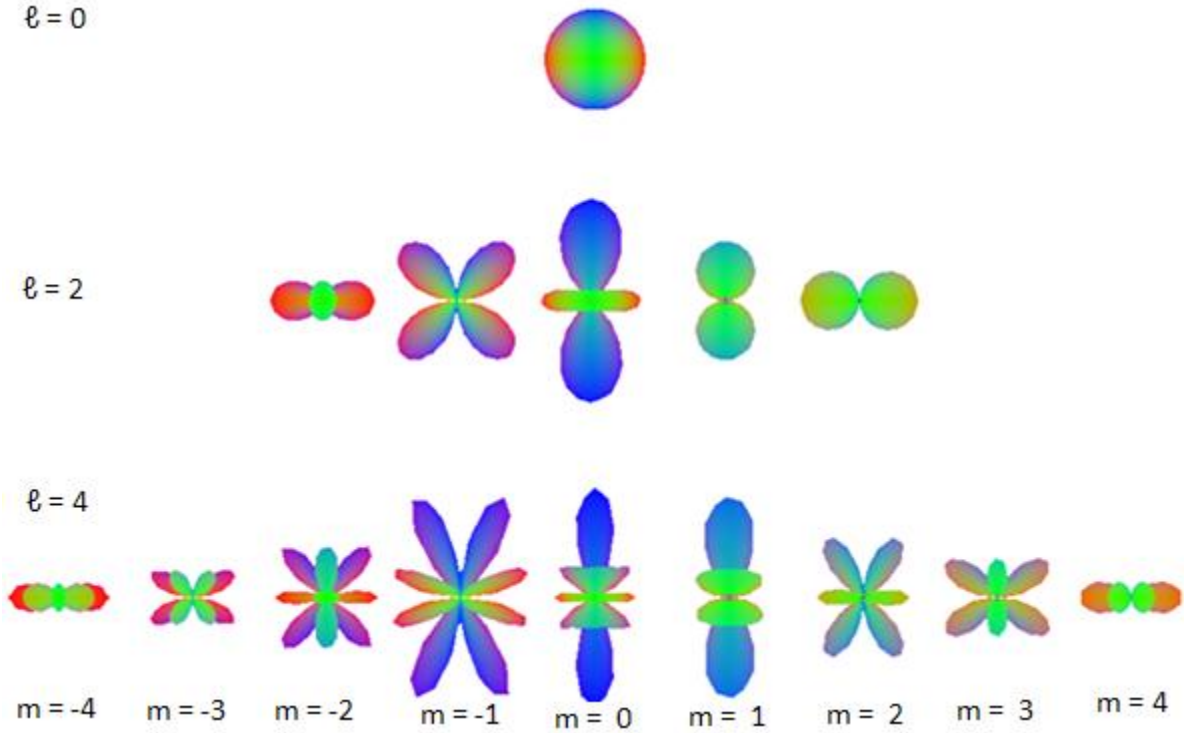
Fig.4.3: Spherical Harmonics Illustration. Only the even order basis corresponding to order 2 and 4 are shown. Spherical harmonics can be used to represent a square integrable function on the unit sphere.

Since the ODF is a real and symmetric function, the modified real and symmetric spherical harmonic bases can be defined by considering only the even degree terms by defining a single index j as follows [31],

$$j(\ell, m) = m + \frac{\ell^2 + \ell + 2}{2} \tag{4.16}$$

where ℓ is the degree and m is the order. The values of ℓ and m are defined as,

$\ell = 0, 2, 4, \ldots, L$ (since only even terms are considered); $m = -\ell, \ldots, 0, \ldots, \ell$

Using the definition of a single index j (in Eq.4.16), the modified Spherical harmonic bases are chosen based on the order m as follows[31],

$$Y_j = \begin{cases} \sqrt{2}.\, R_e\left(Y_\ell^{|m|}\right), & if\ m < 0 \\ Y_\ell^m, & if\ m = 0 \\ \sqrt{2}.\,(-1)^{m+1}\text{Im}(Y_\ell^m), & if\ m > 0 \end{cases}$$

(4.17)

Hence in this formulism, an ODF can be treated as a square integrable spherical function on a unit sphere and can thus be approximated with a linear combination of these modified spherical harmonics bases Y_j. Since the ODF is a smooth spherical function, it may be approximated by a linear summation of only a few bases of spherical harmonic series, since higher order spherical harmonics may be needed only to represent functions consisting of high frequency components. Mathematically,

$$ODF(u) = \sum_{j=1}^{N} c_j Y_j(u),$$ (4.18)

where u is the number of directions along which the ODF is reconstructed, and c_j are the coefficients corresponding to the jth modified spherical harmonic bases described below.

4.5.2 Deconvolution of DSI ODFs based on spherical harmonic

The deconvolution begins with the assumption that the obtained DSI ODF ($ODF_{obtained}$) is formed by the convolution between the single fiber diffusion ODF kernel, R, and the true fiber ODF Fig.4.4 (a). Hence in theory, the deconvolved ODF (i.e. $ODF_{expected}$) can be obtained by deconvolving the single fiber response function R from the given DSI ODF ($ODF_{obtained}$) [31] as illustrated in Fig.4.4 (b) .
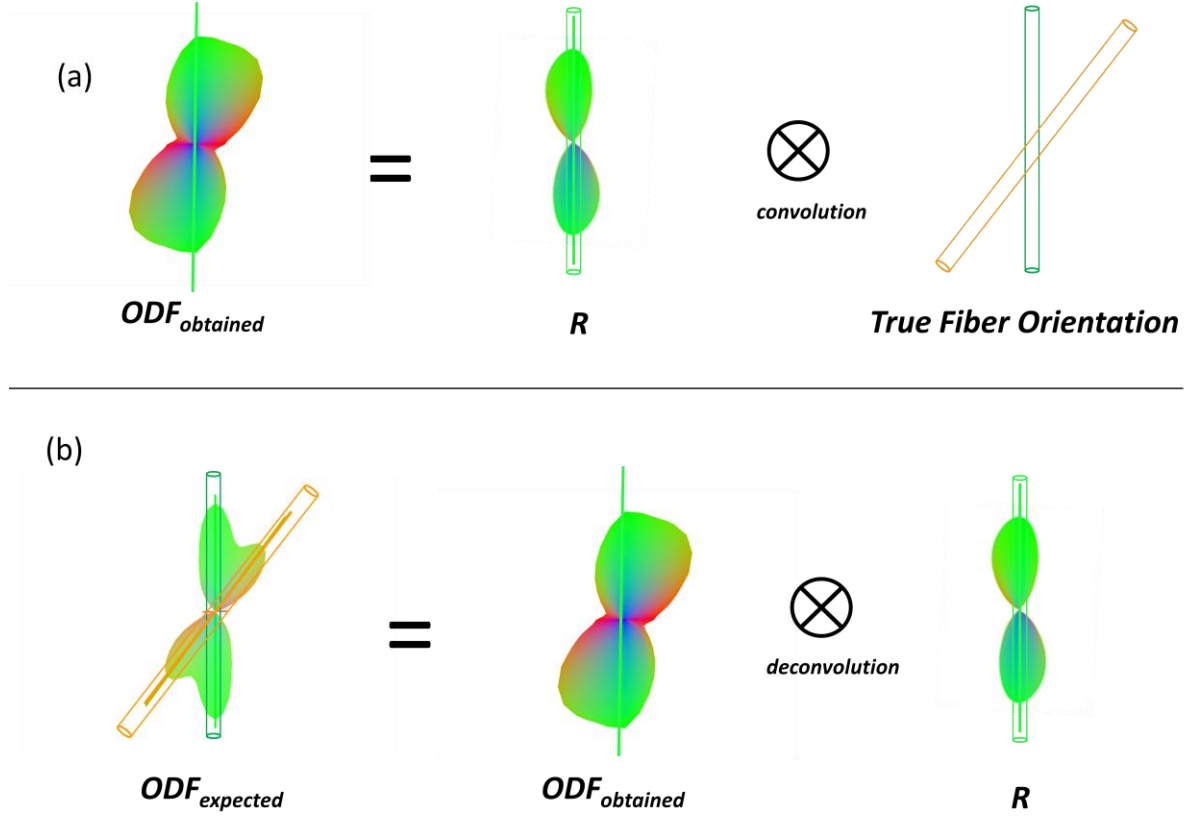
Fig.4.4: Concept of Deconvolution Applied to ODFs Obtained from DSI. (a) A DSI ODF ($ODF_{obtained}$) can be represented as a convolution of the single fiber response function R with the true fiber orientation. (b) The deconvolved ODF ($ODF_{expected}$) can thus be obtained by deconvolving the single fiber response function R from the given DSI ODF ($ODF_{obtained}$).

The problem formulation begins by representing a DSI ODF ($ODF_{obtained}$) as a convolution of the single fiber response function with the true fiber orientation ($ODF_{expected}$). Mathematically, this spherical convolution can be written as,

$$ODF_{obtained}(\text{u}) = \int_{|z|=1} R(u.z)\, ODF_{expected}(z)dz \tag{4.19}$$

where $R(\text{u}.\text{z})$ is the single fiber response function and the integration is performed on a unit sphere (represented by $|\text{z}| = 1$).

As explained in the previous section, an ODF may be approximated by a truncated spherical harmonic representation. Hence, both $ODF_{obtained}$ and $ODF_{expected}$ may be represented with their corresponding spherical harmonics coefficients c_{jo} and c_{je} respectively. Mathematically,

$$ODF_{obtained} = \sum_{j=1}^{N} c_{j0} Y_j(u) \qquad (4.20)$$

$$ODF_{expected} = \sum_{j=1}^{N} c_{je} Y_j(u) \qquad (4.21)$$

Hence, the convolution integral may be reformulated as,

$$\sum_{j=1}^{N} c_{jo} Y_j(u) = \sum_{j=1}^{N} c_{je} \int_{|z|=1} R(u.z) Y_j(z) \, dz, \qquad (4.22)$$

To solve this convolution integral, Funk-Hecke formula can be applied. The Funk-Hecke formula is a theorem that relates the inner product of any spherical harmonic (Y_j) with any continuous function defined on the interval $[-1, 1]$ eg. R. The Funk-Hecke formula greatly simplifies the convolution integral over the sphere and reduces it to the following equation:

$$\sum_{j=1}^{N} c_{jo} Y(u) = \sum_{j=1}^{N} 2\pi P_{\ell_j}(0) c_{js} f_j \, Y_j(u) \qquad (4.23)$$

where P_{ℓ_j} is a Legendre polynomial of order ℓ_j and since only even orders in the SH basis are used, $P_{\ell_j}(0)$ is simply formulated as,

$$P_{\ell_j}(0) = (-1)^{\frac{l_j}{2}} \left\{ \frac{\left(3.5....(\ell_j-1)\right)}{2.4....\ell_j} \right\} \qquad (4.24)$$

where the coefficient f_j are solved using the Funk-Hecke formula as follows:

$$f_j = 2\pi \int_{-1}^{1} P_{\ell j}(t)\, R(t)\, dt\,, \quad t \in \{-1,1\} \tag{4.25}$$

where $R(t)$ is the single fiber response function. According to [32], $R(t)$ is specified as a Diffusion Tensor "D" from single fiber region with eigenvalues [λ1, λ2, λ3] (such that λ1 >> λ2, λ3 and λ3 ≈ λ2). R(t) was determined from the voxels containing the highest diffusion anisotropy value. This strategy is same as other studies involving such single fiber response function [31, 32, 34]. In accordance with [31] and [13], R(t) was formulated as a diffusion ODF as follows:

$$R(u) = \frac{1}{Z}\sqrt{1/(u'D^{-1}u)}\,, \quad u = (x, y, z)' \tag{4.26}$$

where Z is a normalization constant [13].

$R(u)$ is converted to spherical coordinates and finally to the [-1,1] domain in order to satisfy the condition for the Funk-Hecke formula. This was done in accordance with [31].

Finally, the computed f_j are used to obtain the expected ODF as follows:

$$ODF_{expected}(u) = \sum_{j=1}^{N} 2\pi\, P_{l_j}(0)\, c_{je}\, Y_j(u) \tag{4.27}$$

where $c_{je} = c_{jo}/f_j$ \hfill (4.28)

Hence, a technique to de-convolve the response function of an individual peak from the overall ODF was implemented.

The DSI analysis flowchart was modified to include this deconvolution module (as shown in Fig.4.5) and the deconvolved ODFs were utilized instead of the originally obtained ODFs.
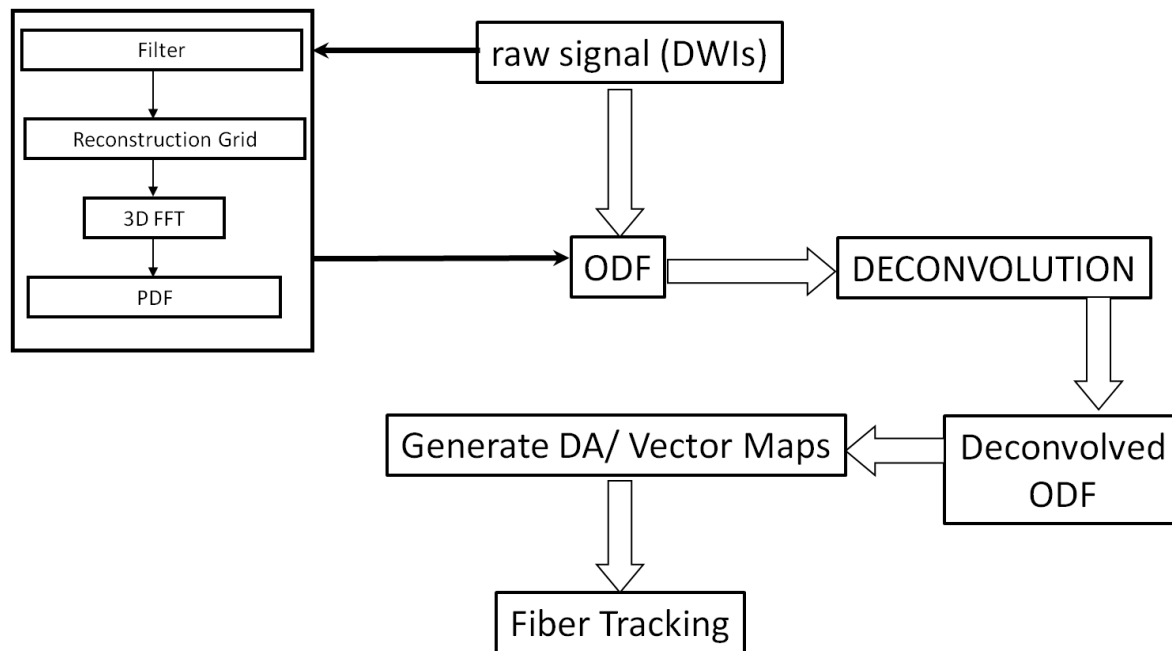
Fig.4.5: Modification in DSI Analysis Flowchart to Include ODF Deconvolution. The ODF computed is deconvolved and then used to generate the DA and Vector Map which results in a better delineation of the peaks (see text for details)**.**

4.5.3   Final DSI Data post processing workflow

DSI data analysis was performed as follows:

For each imaging voxel, the dimension of the q-space was set to a 17x17x17 Cartesian grid. The DWI signal intensities were reorganized in this gridded 3D space around the center of q-space. Note that in doing so, the signal intensity value at (0,0,0) was placed at the center (8,8,8) of the q-space grid and the signal intensities from the increasing q value images were placed in accordance with their sampled positions.

A Hanning filter (size=8) was applied to the q-space in order to ensure smooth attenuation of the signal at high |q| values. The filtered q-space was zero padded to 17x17x17. A 3D Fourier transform was performed to obtain the 17x17x17 PDF space (3-

dimensional double floating-point array) to obtain the 3D PDF. The ODF was estimated by integrating several discrete points along various directions in the PDF (from 2.1 to 6.0, step = 0.2). These directions were defined by a set of vectors ui that were vertices generated from a 4-fold tessellated icosahedron consisting of 642 sampling directions. This resulted in an optimal accuracy in ODF for visualization purposes. Note that tri-Iinear interpolation was used to obtain the missing values from the discrete PDFs. The ODF was obtained by deformation of a RGB color coded sphere with the radius proportional to the PDF value in a particular Ui direction in accordance with Eq.4.12. Min-Max normalized ODF was obtained by normalizing the ODFs by the maximum ODF length within each voxel. ODF was deconvolved using the methodology explained in the previous section. Diffusion anisotropy (DA) was computed based on these deconvolved ODFs.

At each voxel, deconvolved ODFs were used to infer fiber directions by searching the local maxima, i.e. a set of directions of maximum diffusion. Hence, a ODF with its associated set of direction vectors and an associated DA value at every voxel in the scanned volume was determined. This information was utilized for subsequent fiber tracking.

Fiber tracking was performed based on the direction vectors derived from the maximas of the ODFs which comprised the vector set. Fiber tracking was based on a modified streamline (or Eulerian integration or deterministic) algorithm[22], such that multiple directions per step could be accounted for. From each initialization seed voxels, bi-directional steps were initiated in every voxel, for each vector in the set. Thus a fiber trajectory was grown in two opposite directions. The first step was chosen with a predefined step-size (stepsize) in a random direction and the subsequent steps were chosen along the

[61]

direction of the vector whose orientation was the closest to the current direction of the fiber. The same criterion was used upon entering a new voxel i.e. the direction that produces least curvature for the incoming path was chosen. The fiber was terminated either if upon entering into a new voxel results in a change of direction sharper than Øc or when both the fiber ends enter the gray matter (determined by a DA value of DAthesh). A stepsize of 0.4 was used. Note that the step-size should be kept at a value of $< \frac{1}{2}$ the voxel size as recommended by [22]) . A smaller step-size results in finer fiber turns. Also, a typically threshold value of Øc<0.5 radian (i.e. 30) was used. A DA threshold (DAthesh) value of 0.25 was chosen based on the range of DA values in the gray matter of our data-sets.

4.5.4   MRI acquisition (Phantom Study)

MRI data was acquired on all the three phantoms on a Philips 3.0 T Intera scanner (Achieva, Philips Medical Systems, Best, Netherlands) with a maximum gradient amplitude of 80 mT/m and a slew rate of 200 mT/m/ms. An 8 channel SENSE FLEX coil was used for data acquisition. T2-weighted images were acquired using Turbo Spin Echo (T2-TSE sequence) with the following sequence parameters; TE/TR=100/5000 msec; FOV=120x120 mm2; Matrix=512x512; Spatial Resolution= 0.234x0.234 mm/px; ΔTH=4 mm; NEX=8;

DWIs were acquired on all the three phantoms developed and reported in the previous chapter (90°, 45° and 60°). The DSI patch was obtained from Gyrotools and is based on the single shot spin echo EPI based diffusion weighted pulse sequence similar to the one used in DTI, with the added functionality of predefined sampling directions on a Cartesian grid. A gridsize could be defined in the DSI acquisition scheme whereby a gridsize of 3 correspond to 123 samples, a gridsize of 4 correspond to256 samples, while a gridsize of 5 correspond

to 515 directions and so on. The gridsize of 4 was used for the 90° phantom and gridsize of 5 was used for the 45° and 60° phantom, since they require a higher angular resolution to distinguish (as explained in the next chapter). The DWIs were averaged 8 times on the scanner (NEX=8) to get sufficient SNR. A maximum b-value of 6600 s/mm2 was used for all the acquisitions. The following sequence parameters were used: TE/TR: 85.9/7500 msec; FOV=120x120 mm2; matrix=128x128; spatial resolution=0.9375x0.9375 mm/px; slice thickness = 4 mm. Note that additional data was acquired using different NEX and number of samples whose effects will be presented in details in the next chapter.

4.6 RESULTS

4.6.1   Results on the 45° phantom

Fig.4.6 (a) presents a high resolution T2-weighted image of the 45° phantom containing both single fibers and crossing fibers. Representative ODFs, from each of these single and crossing fiber regions, are shown in Fig.4.6 (b and c) respectively, before employing any deconvolution procedure. Note that the quality of ODFs in the single fiber region appears visually satisfactory and represents the underlying fiber orientations correctly; however, the two peaks in the crossing region are indistinguishable and the true peaks are masked.

The same ODFs are shown in Fig.4.6 (d and e) after employing the deconvolution procedure. With the application of deconvolution procedure, the two true peaks in the ODF are readily detectable (Fig.4.6 d), while the orientation of the single fiber region ODF is also enhanced (i.e. the peaks are narrower in the deconvolved ODF). Also, the 3D angle between

the two vectors (generated in the direction of the peaks of the deconvolved ODF) was very close to 45° for the illustrated ODF, verifying the robustness of both the deconvolution technique and the phantom construction.

Fig.4.6: Illustrative Pixels From 45° Phantom Before and After Deconvolution. (a) High resolution T2-weighted Image of the 45° phantom; (b) representative ODF from the single fiber region before deconvolution; (c) representative ODF from the crossing fiber region before deconvolution; (d) representative ODF from the single fiber region after deconvolution; and (e) representative ODF from the crossing fiber region after deconvolution.

Fig.4.7 and Fig.4.8 illustrate a central 7x7 region of the phantom before and after applying the deconvolution procedure respectively. Qualitative improvement in overall ODF quality can be appreciated.
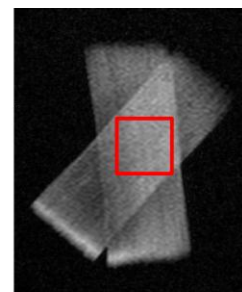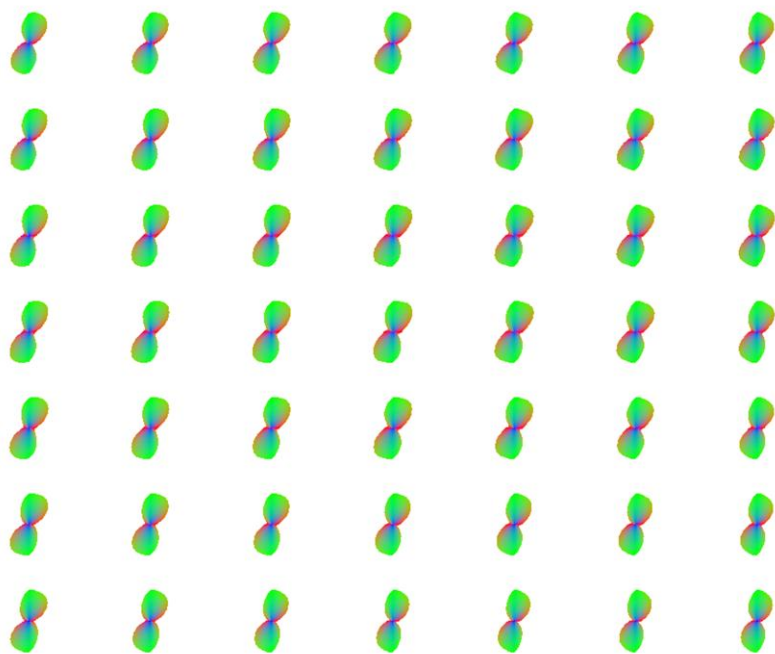
Fig.4.7: **ODFs of 45° Phantom Before Deconvolution.** The Central 7x7 region is depicted on the T2 weighted image shown in the inset.
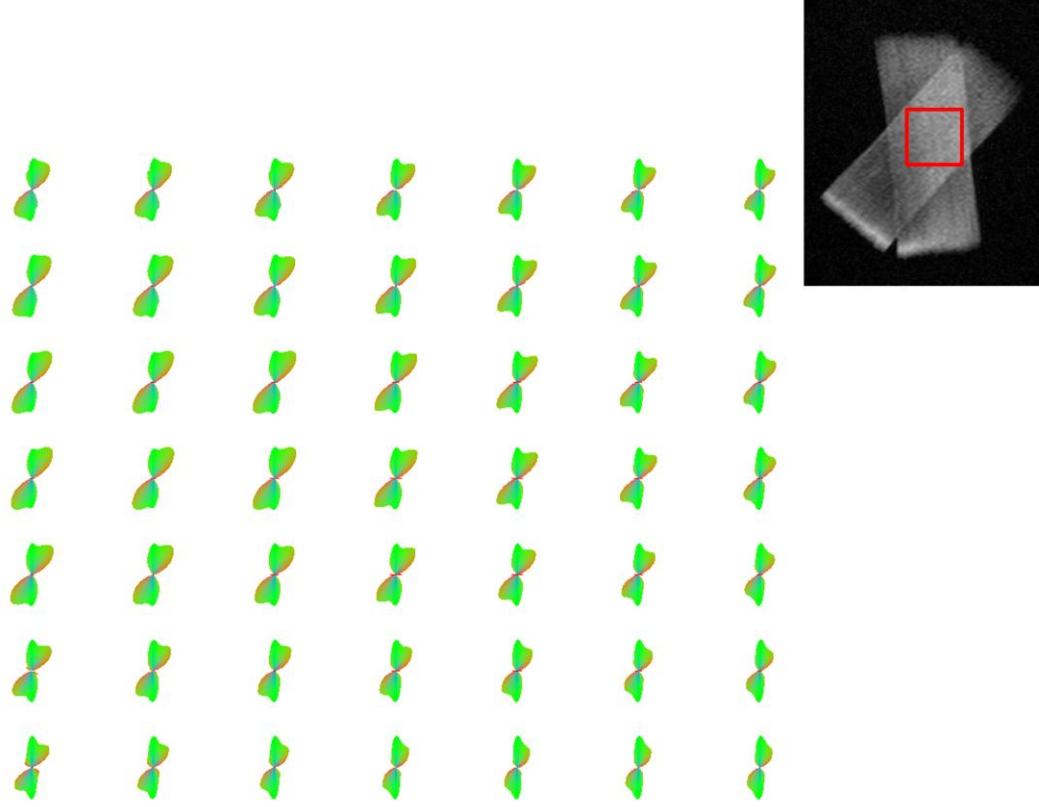
Fig.4.8: **ODFs of 45° Phantom After Deconvolution.** The Central 7x7 region is depicted on the T2 weighted image shown in the inset.

For each voxel, vectors are computed from the peaks of the deconvolved ODF. A DA map was also generated based on the deconvolved ODFs and the vectors are shown overlaid on the DA map in Fig.4.9. The single fiber regions show precisely one vector with correct orientation while the crossing fiber regions show two vectors forming an angle ≈ 45°, consistent with the ground truth.
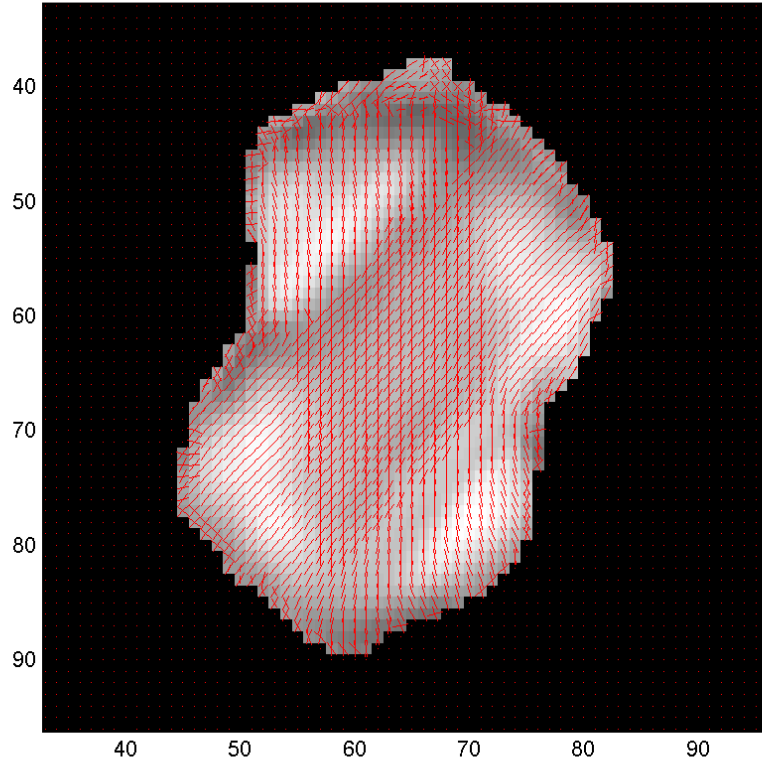
Fig.4.9: **Vector Map Overlaid On DA Map For 45° Phantom.** The vectors are computed from the peaks of the deconvolved ODFs obtained at each voxel. These vectors are overlaid on the DA map (generated based on the deconvolved ODFs).

4.6.2 Results on the 90° phantom

Representative ODF from the crossing region of 90° phantom is shown in Fig.4.10 (a) before and in Fig.4.10 (b) after applying the deconvolution technique. Although, deconvolution leads to narrowing of the peaks and enhances the visual appearance of ODF, it does not make any significant change in the detection or orientation of the peaks in the ODF. The two peaks were correctly identified in both cases (with or without deconvolution) and returned an angle ≈ 90°.
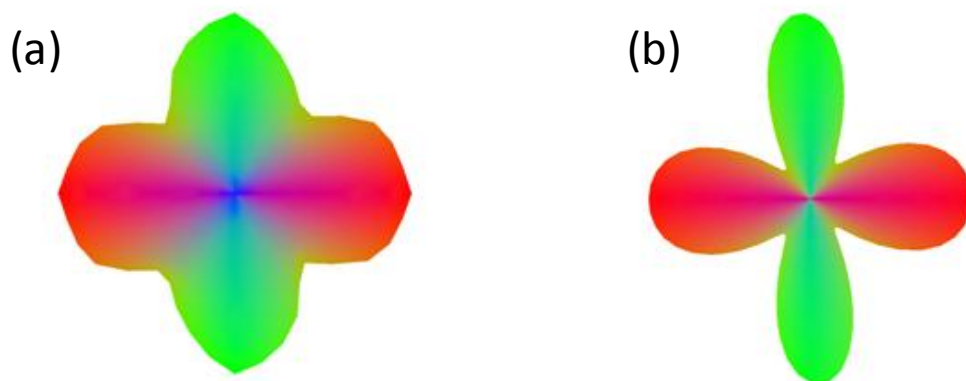
Fig.4.10: **ODFs From Crossing Region of 90° Phantom.** (a) ODF before applying the deconvolution technique; (b) ODF after applying the deconvolution technique. Note that deconvolution does not make any significant change in the detection or orientation of the peaks in the ODF. The two peaks were correctly identified in both cases (with or without deconvolution) and returned an angle ≈ 90°.

Fig.4.11 and Fig.4.12 illustrates a central 7x7 region of the phantom before and after applying the deconvolution procedure respectively. Qualitative improvement in overall ODF quality can be appreciated.

Fig.4.11: **ODFs of 90° Phantom Before Deconvolution.** The Central 7x7 region is depicted on the T2 weighted image shown in the inset.

Fig.4.12: **ODFs of 90° Phantom After deconvolution.** The Central 7x7 region is depicted on the T2 weighted image shown in the inset.

For each voxel, vectors are computed from the peaks of the deconvolved ODF. A DA map was also generated based on the deconvolved ODFs and the vectors are shown overlaid on the DA map (Fig.4.13)
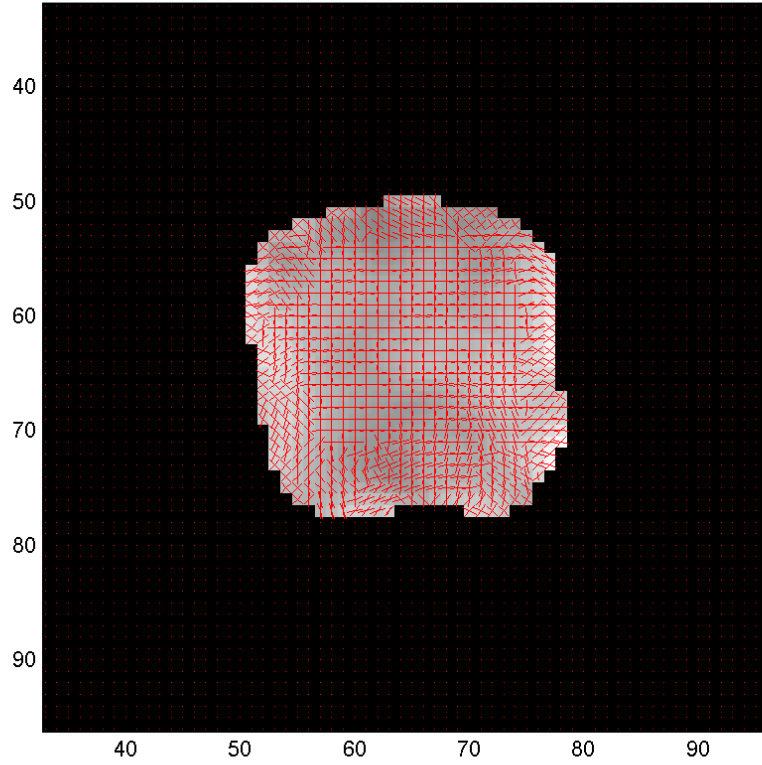
Fig.4.13: **Vector Map Overlaid on DA Map for the 45° Phantom.** The vectors are computed from the peaks of the deconvolved ODFs obtained at each voxel. These vectors are overlaid on the DA map (generated based on the deconvolved ODFs).

4.6.3   Results on the 60° phantom

Several examples of before and after the application of the deconvolution procedure are shown in Fig.4.14 on the 60° phantom. Fig.4.6 (a) presents a high resolution T2-weighted image of the 60° phantom containing both single fibers and crossing fibers. Note that both two and three way crossings exist along-with the single fiber regions in the 60° phantom which can be simultaneously evaluated)
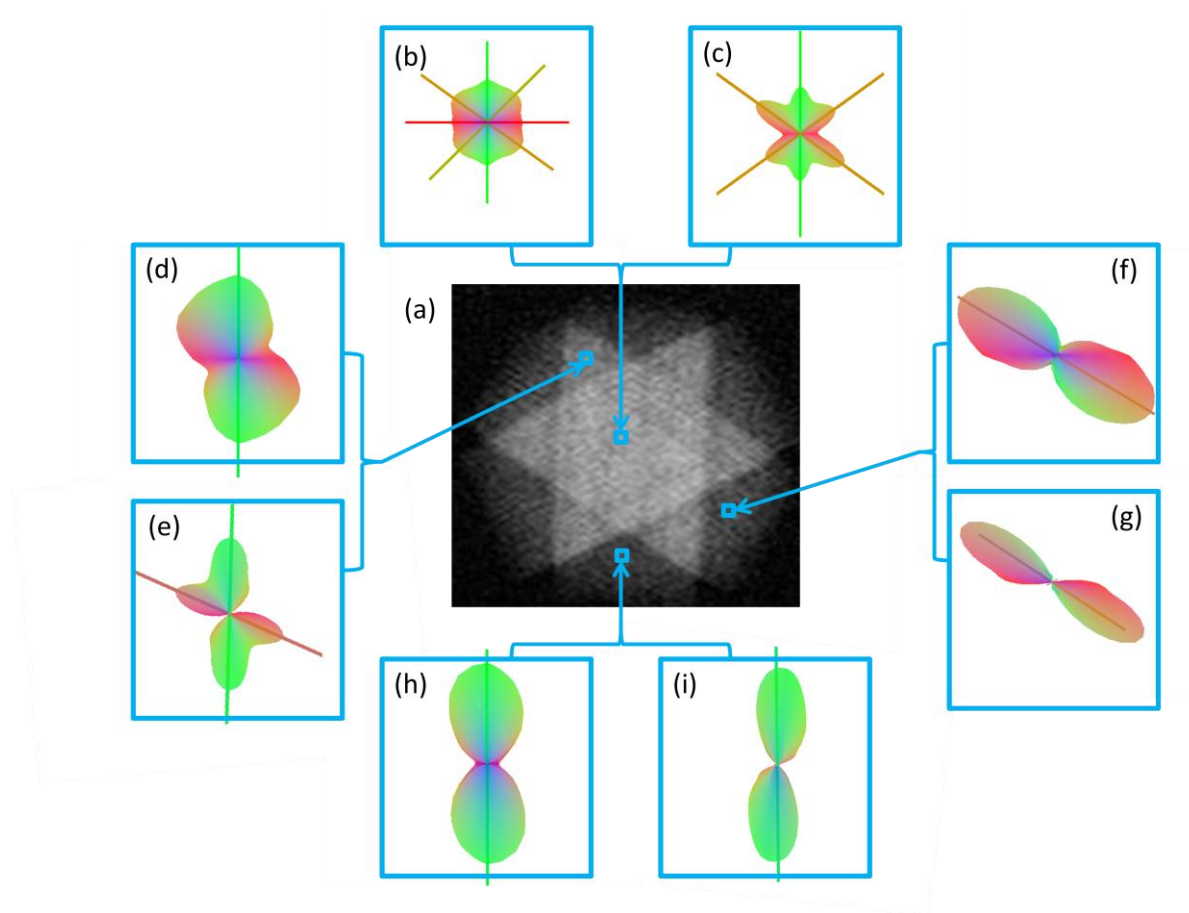
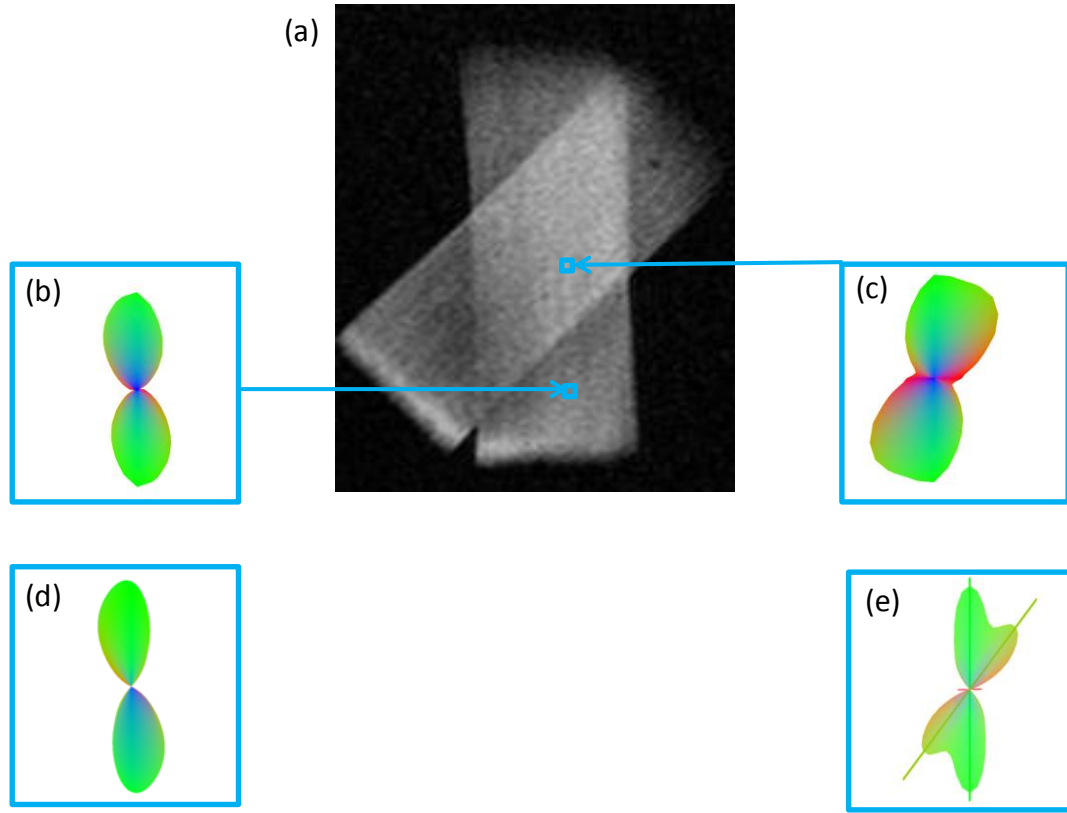**Fig.4.14: ODFs From 60° Phantom Before and After Deconvolution.** (a) high resolution T2-weighted image of the phantom; (b and c) representative ODF from the three way crossing fiber region of the phantom before and after deconvolution; (d and e) representative ODF from the two way crossing fiber region of the phantom before and after deconvolution; (f and g) representative ODF from the single fiber (inclined)region of the phantom before and after deconvolution; (h and i) representative ODF from the single fiber (vertical) region of the phantom before and after deconvolution.

A representative ODF, from the three crossing fiber region, is shown in Fig.4.14 (b and c) before and after applying the deconvolution procedure, respectively. Note that before applying the deconvolution, either a spurious fourth peak was identified in some voxels (as shown in Fig.4.14b) or the three peaks were not identified and were masked (not shown). Deconvolution presents an ODF with much sharper geometry and clearly visible three peaks which were correctly identified. Also, the angle between first and second vector computed

from the deconvolved ODF was correctly identified to be ≈ 60°. Additionally, the angle between second and third vector was also correctly identified to be ≈ 60°.

Also, a representative ODF, from the two crossing fiber region, is shown in Fig.4.14 (d and e) before and after applying the deconvolution procedure, respectively. Note that before applying the deconvolution, the two peaks were not correctly identified and one of the peaks was masked (as shown in Fig.4.14d). Deconvolution presents an ODF with much sharper geometry and clear two peaks which were correctly identified. Also, the angle between first and second vector computed from the deconvolved ODF was correctly identified to be ≈ 60°.

Finally, a representative ODF, from the single fiber region inclined at 60°, is shown in Fig.4.14 (f and g) before and after applying the deconvolution procedure, respectively. Another such pair of representative ODF, from the single fiber vertical region, is shown in Fig.4.14 (h and i) before and after applying the deconvolution procedure, respectively. The quality of ODFs in the single fiber region is good even without deconvolution and represents the underlying fiber orientations correctly. With the application of deconvolution procedure, the single fiber region ODFs are further enhanced (i.e. the peaks are narrower in the deconvolved ODF).

Overall, it can be appreciated from the deconvolved ODFs (Fig.4.14 c, e, g, i) that the deconvolution resulted in narrower peaks and hence better angular resolution of the ODF. This evaluation verifies the robustness of both the deconvolution technique and the 60° phantom construction.

Fig.4.15 and Fig.4.16 illustrates a central 7x7 region of the phantom before and after applying the deconvolution procedure respectively. Qualitative improvement in overall ODF quality can be appreciated.
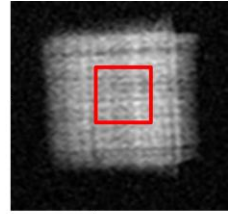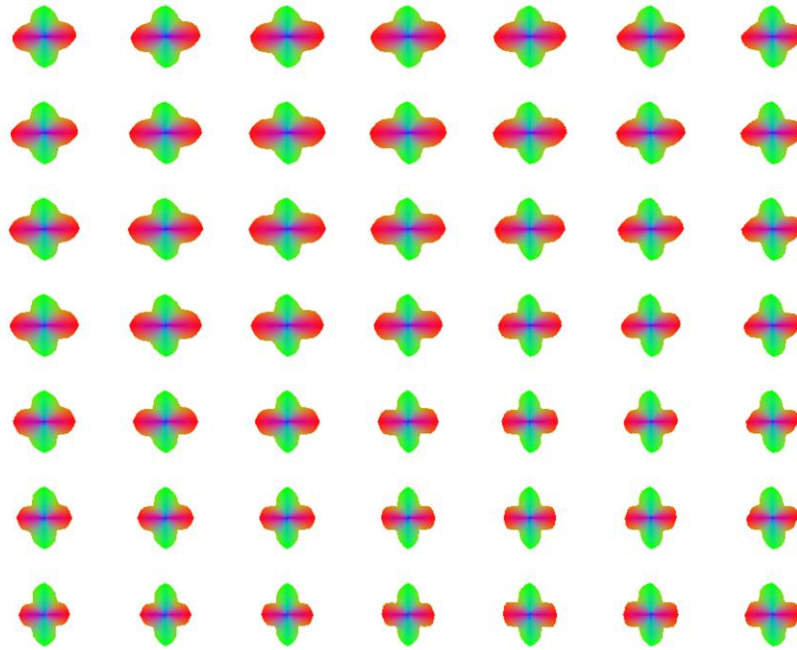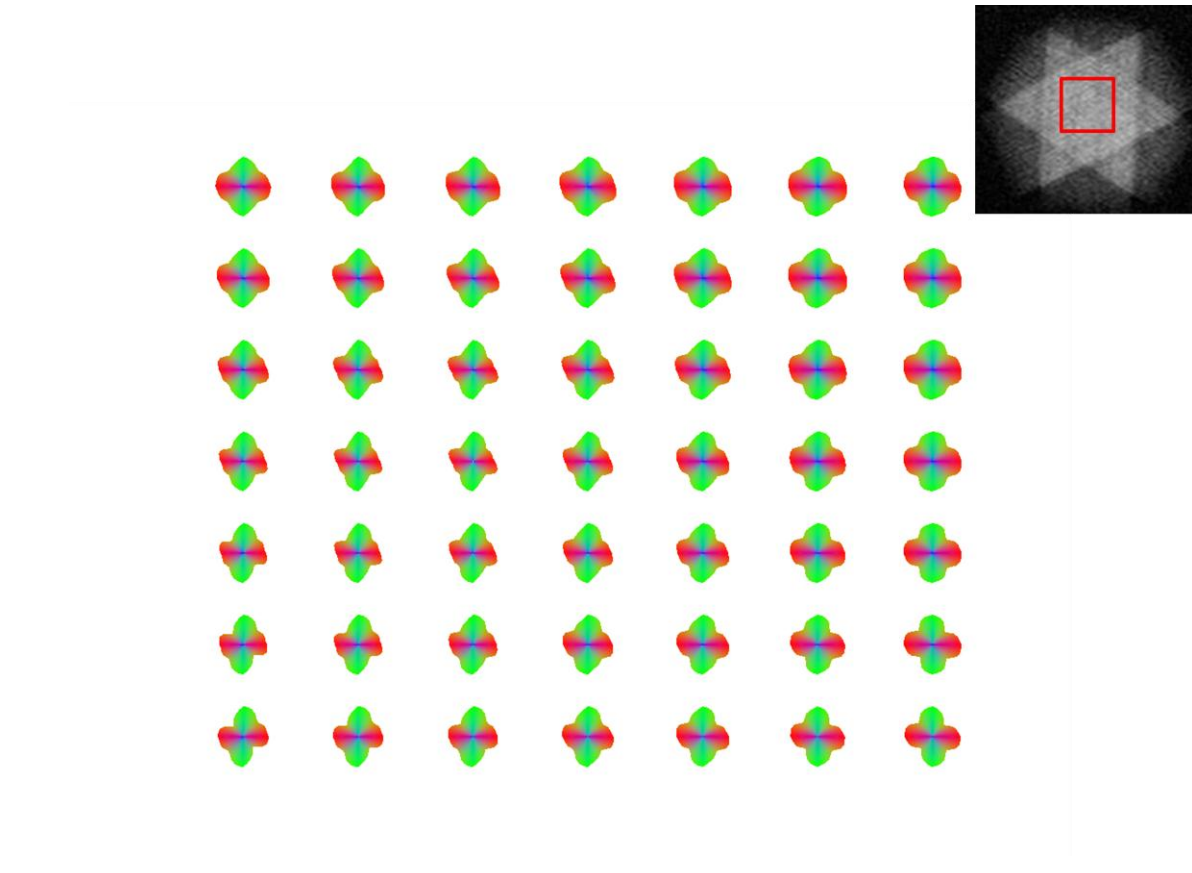

Fig.4.15: ODFs of 60° Phantom Before Deconvolution. The Central 7x7 region is depicted on the T2 weighted image shown in the inset.
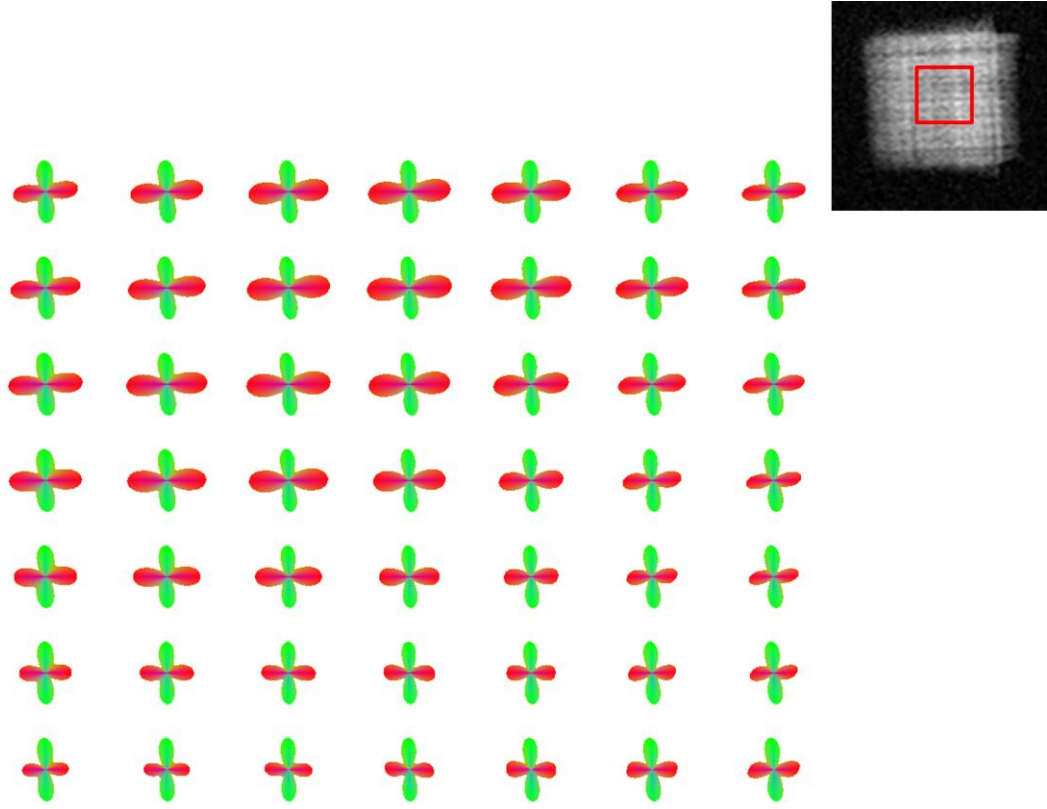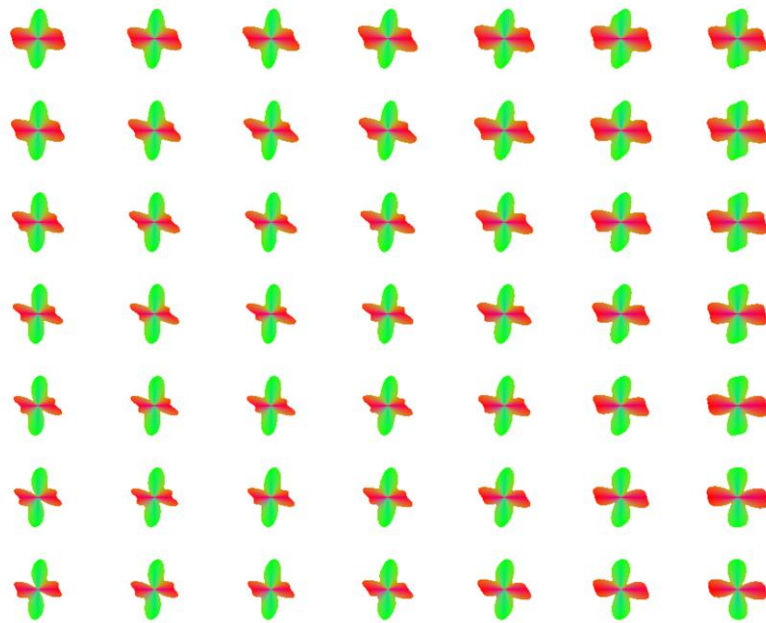
Fig.4.16: ODFs of 60° Phantom After Deconvolution. The Central 7x7 region is depicted on the T2 weighted image shown in the inset.

For each voxel, vectors are computed from the peaks of the deconvolved ODF. A DA map was also generated based on the deconvolved ODFs and the vectors are shown overlaid on the DA map in Fig.4.17. Notice the single fiber regions show precisely one vector with correct orientation, the two crossing fiber regions show two vectors forming an angle ≈ 60° and the three crossing fiber regions show three vectors forming an angle ≈ 60° (both between first and second, and between second and third), in consensus with the ground truth.
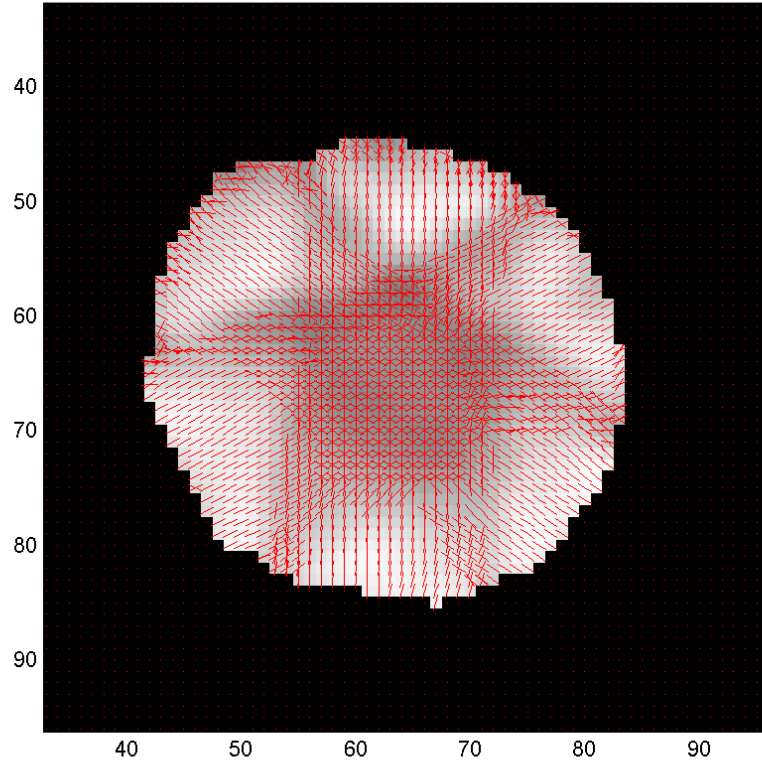
Fig.4.17: Vector Map Overlaid on DA Map for the 60° Phantom. The vectors are computed from the peaks of the deconvolved ODFs obtained at each voxel. These vectors are overlaid on the DA map (generated based on the deconvolved ODFs).

4.6.4   Effect of deconvolution parameters

Note that the deconvolution parameters have a significant impact on the overall performance of the deconvolution procedure and hence these parameters must be chosen carefully. These are the spherical harmonic estimation order ℓ and the regularization term λ. These parameter values were optimized using the ground truth phantoms. The effect of changing these parameters is shown in the following section for the 60° phantom as an example.

[76]

4.6.4.1 Effect of estimation order ℓ

The effect of the order ℓ is shown in Fig.4.18 (b-f) on the deconvolution. For low estimation orders (≤ 8), not all the peaks were correctly identified. As the estimation order ℓ is increased, the true crossing fiber peaks were successfully detected. This is attributed to the higher frequency spherical harmonic bases which are used in the estimation as the order is increased. However, at values of estimation order $\ell \geq 12$, the detected peaks deviated from the ground truth and may lead to spurious peaks for very high estimation orders (not shown). Based on the ground truth, order ℓ of 10 was found to be optimal. This value was verified with the 90° and 45° phantoms as well.
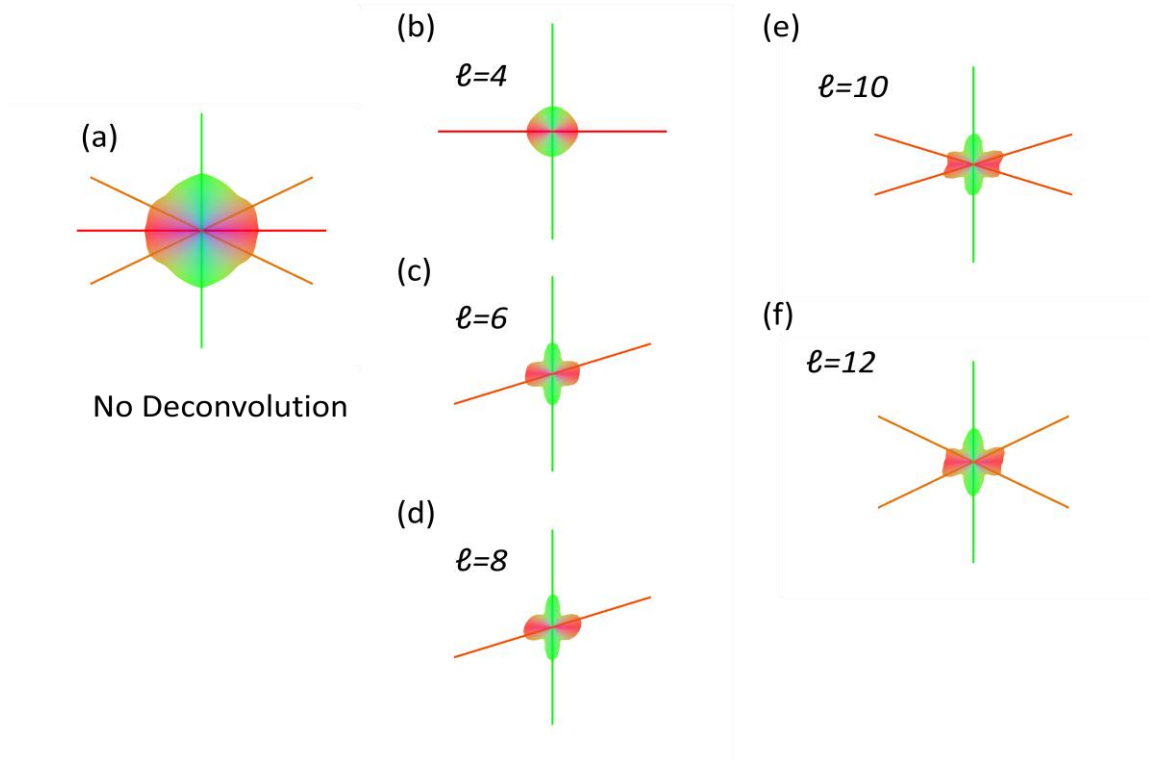
Fig.4.18: Effect of Varying the Estimation Order ℓ on the 60° Phantom. An estimation order ℓ of 10 was found to be optimal, since the ground truth is known. This value was verified to be optimal for the 90° and 45° phantoms as well.

4.6.4.2 Effect of regularization term λ

The effect of the regularization term λ is shown in Fig.4.19 (b-e) on the deconvolution. Without regularization (Fig.4.19 a), the deconvolution doesn't lead to any improvement, and rather worsens the ODF (see Fig.4.18 a - ODF without deconvolution). At very low values of λ (Fig.4.19 b), spurious peaks may be detected. Conversely, at very high values of λ (Fig.4.19 e), the ODF gets very smooth and the true peaks are undetected.
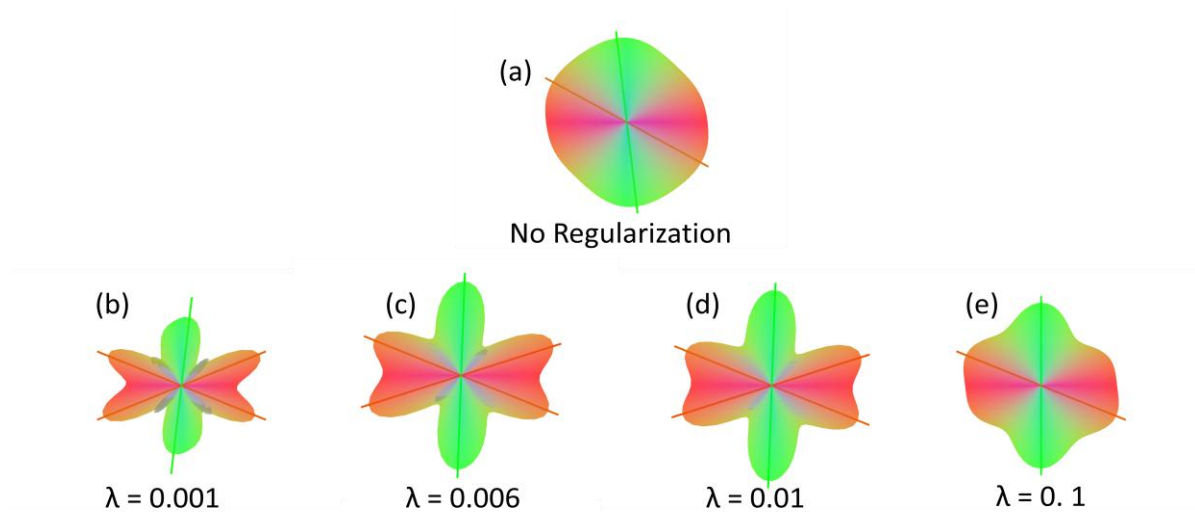
Fig.4.19: Effect of Varying the Regularization Term λ on the 60° Phantom. The regularization term λ of 0.01 was found to be optimal, since the ground truth is known. This value was verified to be optimal for the 90° and 45° phantoms as well.

Overall, without appropriate regularization term, the deconvolution resulted in either undetected or spurious peaks. This was especially true for data with low levels of SNR or low angular sampling, Based on the ground truth, regularization term λ of 0.01 was found to be optimal. This value was verified with the 90° and 45° phantoms as well.

4.7 SUMMARY

This chapter presented the current post-processing methodology in DSI and discussed their limitations. The common issue of compromised angular accuracy of ODF based methodologies in the regions of fibers crossing at acute angles was discussed and the methodologies presented in the literature were briefly reviewed. A deconvolution technique applicable to DSI data as a post-processing step for resolving peaks in the ODF was described. The result of de-convolution post-processing was presented on the data acquired on the phantoms, which demonstrated the efficacy of the proposed deconvolution methodology in DSI. The deconvolution methodology significantly improved the angular accuracy of the DSI derived crossing fibers

CHAPTER 5 – Quantitative Evaluation of DSI Using the Phantoms and Application to Human Fiber Tracking

5.1 INTRODUCTION

Like any other imaging modality, it is important to study the effect of acquisition parameters in DSI prior to applying it to the human studies. Under the constraint of scan time and gradient performance on current clinical systems, it is important to study the effect of parameters which have a significant impact on the angular resolution of DSI. This will allow the optimization of DSI acquisition parameters. The following sections introduce the theoretical background for angular resolution as related to DSI.

5.1.1   Angular Resolution in DSI

Angular resolution is directly proportional to the capacity of any diffusion modality to differentiate fiber populations at each location and to determine their orientation [12, 13, 15, 17, 22, 29]. In DSI, the primary parameters affecting the angular resolution are the number of sampling points and the b-value [17, 22, 28, 29]. Also, the SNR affects the quality of the diffusion weighted images and indirectly affects the angular resolution accuracy.

In a DSI scheme that typically employs a single shot spin echo EPI based diffusion weighted pulse sequence (Fig.5.1), gradient interval (Δ) and the gradient duration (δ) are kept constant during sampling of the q-space while the gradient strength is varied for

different q-space locations. In DSI acquisition, the q-space locations are specified on a Cartesian grid inside a sphere and the sampling points are given by the following equation:

$$q = aq_x + bq_y + cq_z \qquad (5.1)$$

where $\sqrt{a^2 + b^2 + c^2} \leq gridsize \qquad (5.2)$

where (a, b, c are integers) and the gridsize corresponds to the number of sampling directions to be acquired (a gridsize of 3 corresponds to 123 samples, a gridsize of 4 corresponds to 256 samples, a gridsize of 5 corresponds to 515 directions and so on).

For a given echo time TE, δ is minimized and Δ maximized by using the maximal available (allowable) gradient strength g_{max}. Thus the q-space is sampled from the center to

$$q_{max}, \quad q_{max} = \gamma \delta g_{max} \qquad (5.3)$$

where γ is the gyromagnetic ratio

The nominal diffusion spatial resolution (r) given by the following equation:

$$r = 1/q_{max} = \gamma \delta g_{max} \qquad (5.4)$$

The resolution of PDF (PDF_{res}) and FOV of PDF (PDF_{FOV}) can thus be determined using the following equations [15, 17]:

$$PDF_{res} = 1/(2 * q_{max}) \qquad (5.5)$$

$$PDF_{FOV} = 1/\Delta q \qquad (5.6)$$

$$\Delta q = q_{max} / gridsize \qquad (5.7)$$

Finally, the theoretical angular resolution of DSI is given by the following equation:

$$\Omega = \tan^{-1}\{PDF_{res} / (PDF_{FOV} /2))\} \qquad (5.8)$$
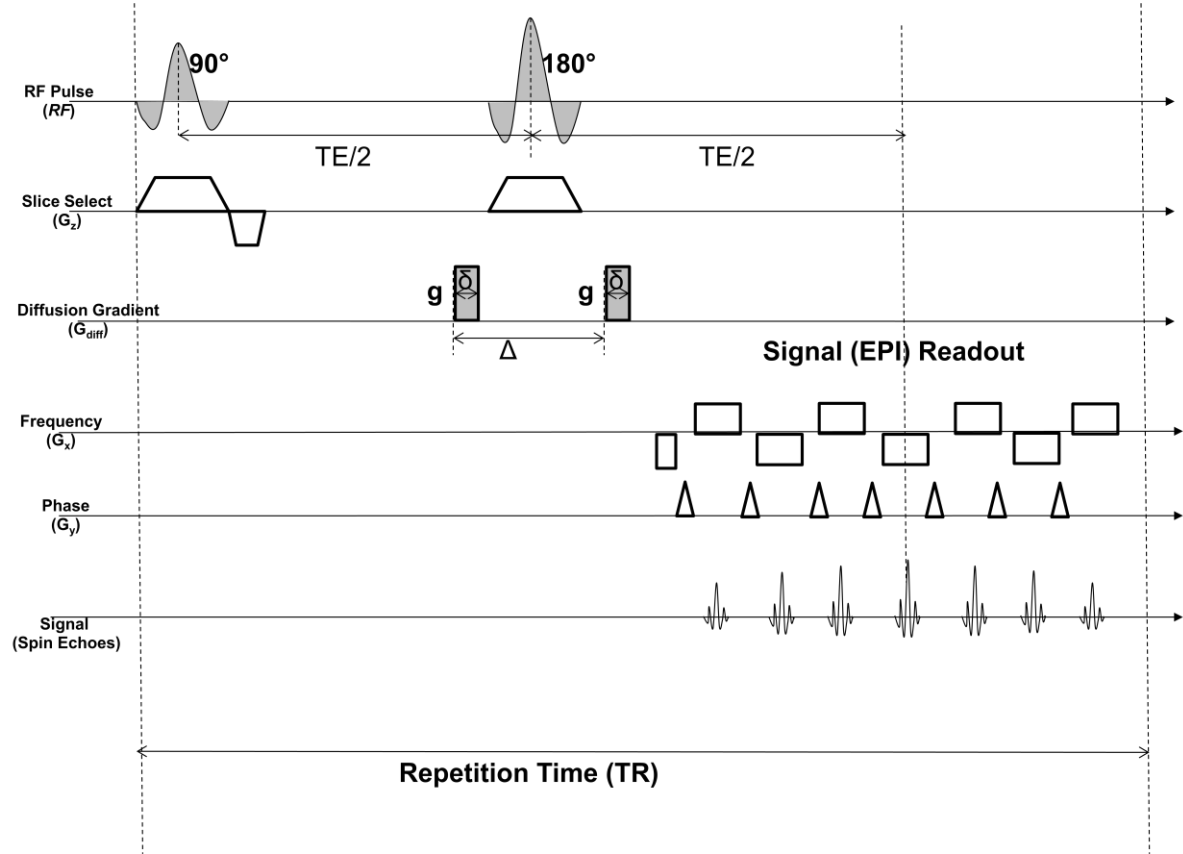
Fig.5.1: Single-shot spin-echo EPI (ss-SE-EPI) Pulse Sequence with Diffusion Weighted Gradients. Pulse sequence typically used to sample the q-space in DSI. Gradient interval (Δ) and the gradient duration (δ) are kept constant during sampling of the q-space while the gradient strength (g) is varied for different q-space locations.

However, the effective angular resolution is approximately the root-mean square sum of the nominal angular resolution and the angular width of the diffusion contrast under the given conditions [22].

5.1.2 Motivation

There are only two studies in the literature which has validated the DSI results using physical phantoms [26, 28]. However, both studies were not performed on a clinical MRI scanner. Also, the limited studies which optimized DSI in a clinical setting [29, 30] did not compare the results against the ground truth.

DSI optimization was performed in [30] by evaluating the variation of several DSI measures (fiber length, fiber density, and average ODF) along the cingulum bundle as a function of the sampling density and diffusion (q-space sampling bandwidth) resolutions. DSI was optimized on a clinical scanner in [29] where the optimal b-value was reported to be 6500 s/mm^2 for DSI data acquired with 515 and 4000 s/mm^2 for DSI data acquired with 203 number of directions. However, their study did not use ground truth phantoms for optimization, and was instead based on simulation of human data.

It is important to study the effect of various acquisition parameters and their practical impact on the accuracy of DSI derived angular information under given experimental conditions [22]. Therefore, in this study, a systematic quantitative evaluation of the angular accuracy of DSI under varying number of sampling directions and SNR is presented using the ground truth phantoms on a clinical 3T scanner.

5.2 METHODS (Phantom)

MRI Acquisition

As summarized in Table 5.1, all the three phantoms (90°, 45° and 60°) were evaluated with 257 sampling directions at various SNR values (achieved by varying the NEX from 2 to 4 to 8). Additionally, the 60° and 45° phantoms were evaluated each with 515 sampling directions at different levels of SNR. Further evaluation was performed with the 45° phantom by varying the number of sampling directions (from 123 to 257 to 515) at a constant SNR. In all evaluations, the data was analyzed on a central homogeneous 10x10 voxel region of interest (100 voxels) as depicted on Fig.5.2.

For all evaluations reported, all other acquisition parameters were kept constant, including the maximum b-value (6600 s/mm2). The following sequence parameters were used: TE/TR: 85.9/7500 msec; FOV=120x120 mm2; matrix=128x128; spatial resolution=0.9375x0.9375 mm/px; Nslices=6; slice thickness = 4 mm.

Phantom	Number of sampling	NEX	SNR
90° Phantom	257	2,4,8	28, 44, 60
45° Phantom	257	2,4,8	32, 44, 60
45° Phantom	515	2,4,8	30, 45, 65
45° Phantom	123,257,515	8	64
60° Phantom	257	2,4,8	38, 46, 61
60° Phantom	515	2,4,8	29, 46, 64

Table 5.1: **Summary of Evaluations Performed with Phantoms.** All three phantoms (90°, 45° and 60°) were evaluated with 257 sampling directions with increasing levels of SNR (achieved by increasing the NEX from 2 to 4 to 8). Additionally, the 60° and 45° phantoms were evaluated each with 515 sampling directions with increasing levels of SNR. Further evaluation was performed with the 45° phantom by varying the number of sampling directions (from 123 to 257 to 515) at a constant SNR. (SNR values are rounded and were calculated from the b0 images).
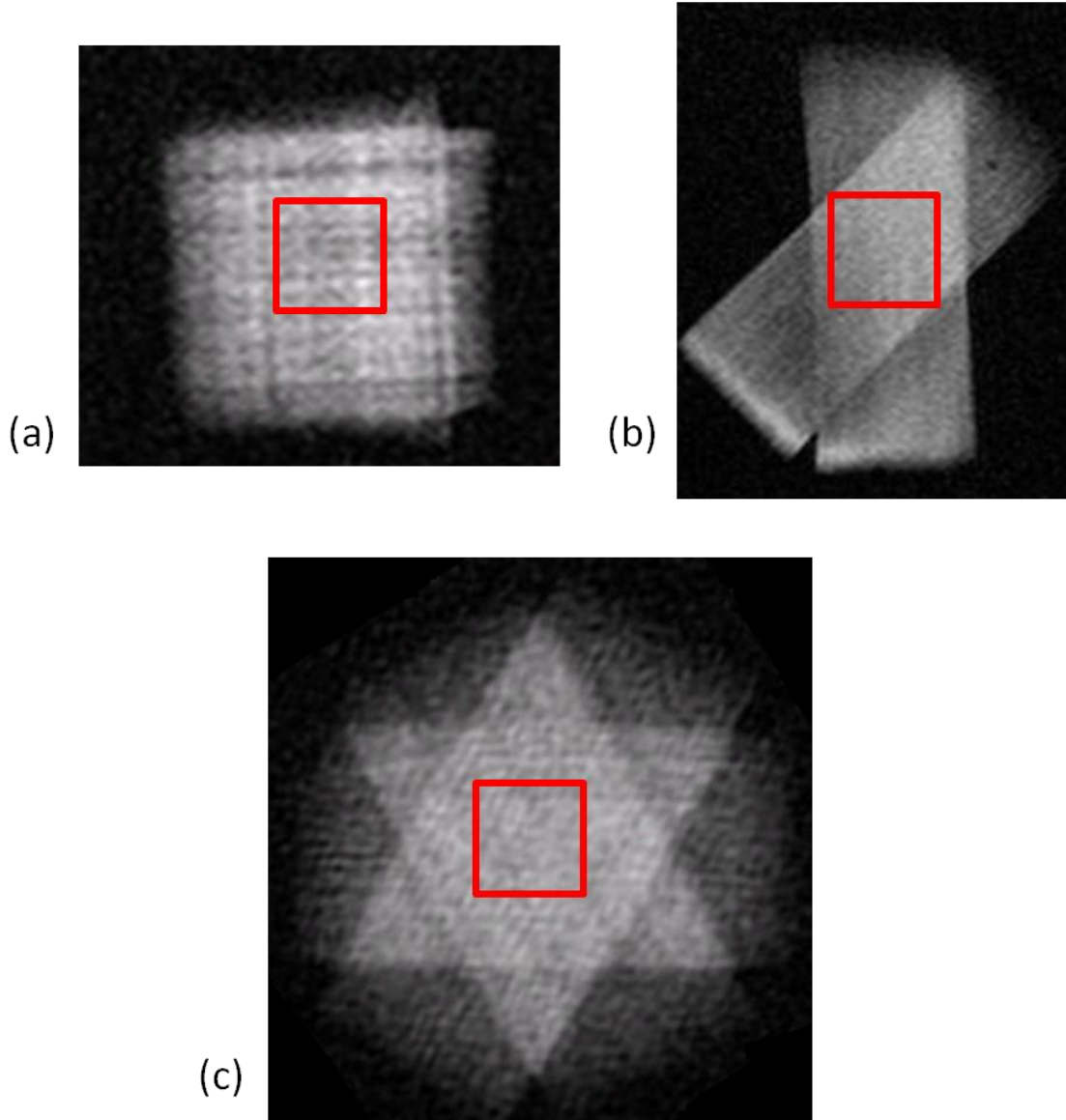
Fig. 5.2: Specification of Region of Interest (ROI) for Quantitative Analysis. (a) ROI on 90° phantom (b) ROI on 45° phantom and (c) ROI on 60° phantom. A homogeneous central region (10x10 voxels) consisting of crossing fibers was chosen for further quantification.

Data was analyzed with the methods developed in the previous chapter. Deconvolution was performed with spherical harmonic order of ℓ=10, and a regularization factor λ=0.01 was used.

The first two primary vectors ($v1$) and ($v2$), detected by the local maximum method (in the case of the 90° and 45° phantoms), are represented as follows:

$$v1 = a_1\,\hat{\imath} + b_1\,\hat{\jmath} + c_1\,\hat{k} \qquad\qquad (5.9)$$

$$v2 = a_2\,\hat{\imath} + b_2\,\hat{\jmath} + c_2\,\hat{k} \qquad\qquad (5.10)$$

The 3D angle between these two vectors (v1) and (v2) was computed as follows:

$$angle = \cos^{-1}(v1.v2) \qquad\qquad (5.11)$$

where $v1.v2$ represents the dot product of $v1$ and $v2$

Similarly, the first three primary vectors ($v1$), ($v2$) and ($v3$) detected by the local maximum method (in the case of the 60° phantom), are represented as follows:

$$v1 = a_1\,\hat{\imath} + b_1\,\hat{\jmath} + c_1\,\hat{k} \qquad\qquad (5.12)$$

$$v2 = a_2\,\hat{\imath} + b_2\,\hat{\jmath} + c_2\,\hat{k} \qquad\qquad (5.13)$$

$$v3 = a_3\,\hat{\imath} + b_3\,\hat{\jmath} + c_3\,\hat{k} \qquad\qquad (5.14)$$

The 3D angle between vectors (v1) and (v2) was computed as follows:

$$angle = \cos^{-1}(v1.v2) \qquad\qquad (5.15)$$

where $v1.v2$ represent the dot product of $v1$ and $v2$

The 3D angle between vectors (v2) and (v3) was computed as follows:

$$angle = \cos^{-1}(v2.v3) \qquad\qquad (5.16)$$

where $v2.v3$ represent the dot product of $v2$ and $v3$

5.3 RESULTS (Phantom)

5.3.1　Results of 90° phantom

The 90° phantom was evaluated by keeping the number of sampling directions fixed at 257 and varying the SNR by increasing the number of averages from 2 to 4 to 8. The results of this evaluation are presented in Fig.5.3. The angle statistics are shown in Fig.5.3 (g, h, i) and

tabulated in Table 5.2. It can be appreciated from the vector maps in Fig.5.3 (a, b, c) and from the overall quality of representative ODFs in (d, e, f) that as SNR increases (from NEX= 2 to 4 to 8), there is an overall qualitative improvement in the detection of the number of crossing fibers (detection efficiency). The crossing angle reaches very close to the ground truth (90°) for NEX = 8 (mean ± STD = 86.93 ± 2.65). For the 90° phantom, reasonable angular accuracy was achieved even at low SNR levels and with 257 sampling directions (with mean ±STD = 82.5 ± 5.43 at NEX = 2) which was much improved already at NEX = 4 (mean ± STD = 85.68 ± 4.12) since the angle between the crossing fibers is quite large (90°) and readily distinguishable. Therefore, I did not find it necessary to evaluate the 90° phantom with 515 sampling points.

Fig.5.3: Results of Evaluation on 90° Phantom (using number of samples = 257 and NEX=2, 4 and 8). (a, b, c) vector map generated from deconvolved ODFs (from the 10x10 voxel region of interest = 100 voxels) corresponding to NEX=2, 4 and 8 respectively; (d, e, f) representative ODF (from the crossing region) after deconvolution corresponding to NEX=2, 4 and 8 respectively; (g, h, i) angles calculated between the first and second vectors for the 100 voxels corresponding to NEX=2, 4 and 8 respectively.

RESULTS			
90° with Number of samples =257	NEX=2	NEX=4	NEX=8
Mean	82.5	85.68	86.93
Median	83.38	87.33	87.63
standard deviation	5.43	4.12	2.65
% detected	100%	100%	100%

Table 5.2: Summary of Results of Evaluation on 90° Phantom (using number of samples = 257 and NEX=2, 4 and 8); Mean, Median, standard deviation (STD) and percentage of voxels detected with two vectors (%detected) are tabulated for the angle between the first and second detected vector (angle 1).

5.3.2 Results of 45° Phantom

45° was evaluated with 257 sampling directions with increasing SNR. Additionally, the 45° phantom was evaluated with 515 sampling directions with increasing levels of SNR. Further evaluation was performed with the 45° phantom by varying the number of sampling directions (from 123 to 257 to 515) at a constant SNR. The following three subsections present the result of each evaluation for the 45° phantom.

5.3.2.1 45° Phantom at 257 sampling directions with increasing levels of SNR

The 45° phantom was evaluated by keeping the number of sampling directions fixed at 257 and varying the SNR varied by increasing the number of averages from 2 to 4 to 8. The results of this evaluation are presented in Fig.5.4. The angle statistics are shown in Fig.5.4 (g, h, i) and tabulated in Table 5.3. It can be appreciated from the vector maps in Fig.5.4 (a, b, c) and from the overall quality of representative ODFs in (d, e, f), that as SNR increases (from NEX= 2 to 4 to 8), there is no overall qualitative improvement in crossing fibers detection accuracy and the values are not in agreement with the ground truth

especially at NEX=4 (mean ± STD = 61.97 ± 11.28). In addition, the percent detection of the two fibers is also very low (55%). These observations can be appreciated visually in the vector map (Fig.5.4 a, b, c). Also, at NEX=2 although the mean is very close to the ground truth (44.04) and the % detection seems to be high (95%), the standard deviation is high (13.67) and the spread in the data can be appreciated visually in (Fig.5.4 g). Also, the deconvolution seems to have incorrectly increased the % detection value to 95% (Table 5.3) since most of the angles are incorrect and far off from the ground truth value of 45° (also, the standard deviation of 13.67 is very high). Hence, deconvolution should be used with caution if the angular resolution of the data is low or if the SNR is low.

Under low SNR conditions and at acute angles, deconvolution may introduce spurious peaks as is the case here (for NEX=2). Hence, even by increasing the SNR (from NEX= 2 to 4 to 8), the results are not in agreement with the ground truth (mean ± STD = 44.04 ± 13.67, 61.97 ± 11.28, 54.53 ± 17.07 at NEX= 2, 4, 8 respectively). This is with regards to a low angular accuracy with 257 samples. Finally, even as SNR increases (from NEX= 2 to 4 to 8), the standard deviations are very high (13.67 at NEX=2; 11.28 at NEX=4 and 17.07 at NEX=8) and there is no particular trend.
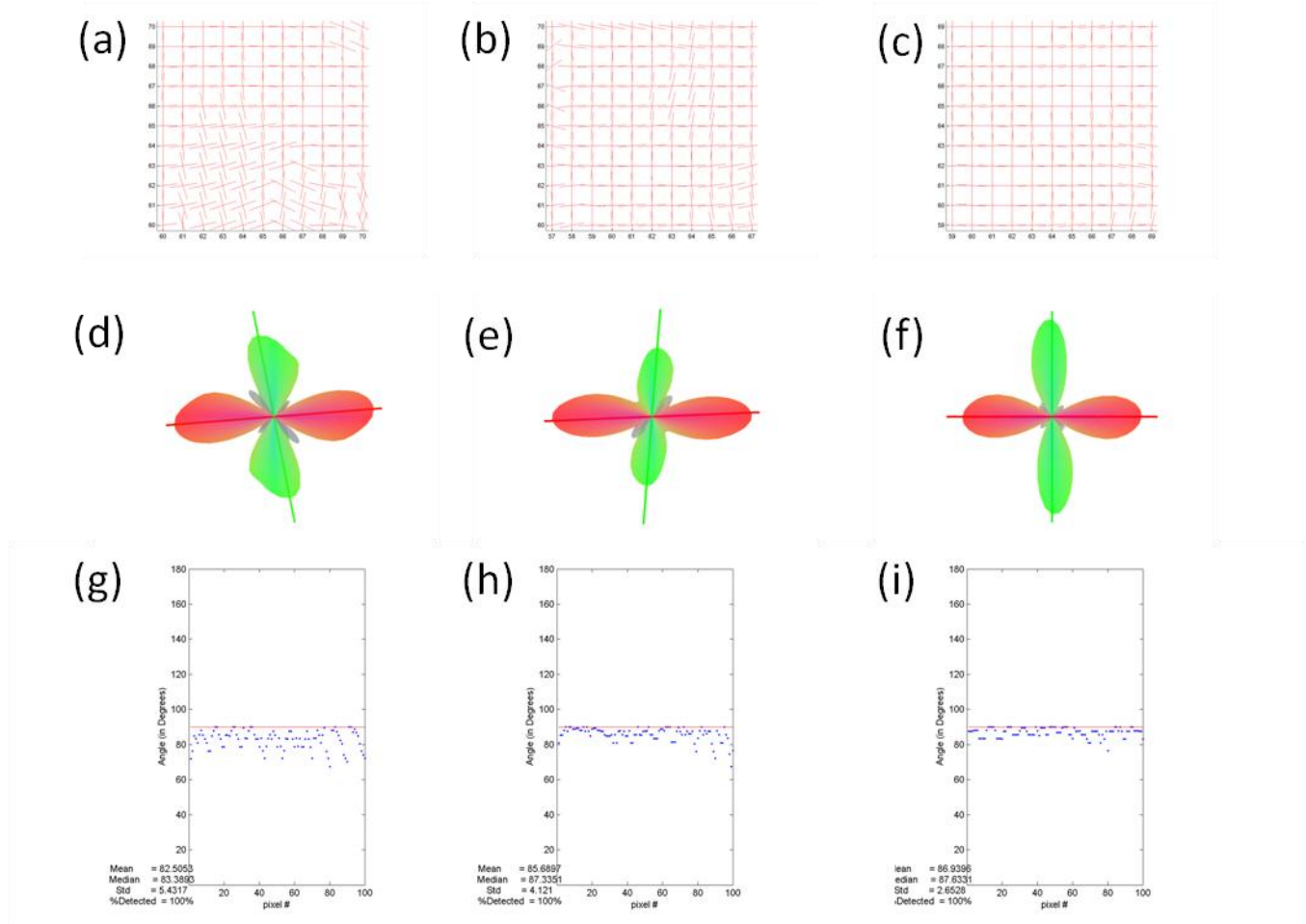
Fig.5.4.: Results of Evaluation on 45° Phantom (using number of samples = 257 and NEX=2, 4 and 8). (a, b, c) vector map generated from deconvolved ODFs (from the 10x10 voxel region of interest = 100 voxels) corresponding to NEX=2, 4 and 8 respectively; (d, e, f) representative ODF (from the crossing region) after deconvolution corresponding to NEX=2, 4 and 8 respectively; (g, h, i) angles calculated between the first and second vectors for the 100 voxels corresponding to NEX=2, 4 and 8 respectively.

RESULTS			
45° with number of samples =257	NEX=2	NEX=4	NEX=8
Mean	44.0446	61.9758	54.538
Median	38.2694	67.5	67.5
standard deviation	13.6718	11.2814	17.0705
% detected	95%	55%	82%

Table 5.3: Summary of Results of Evaluation Performed on 45° phantom (using number of samples = 257 and NEX=2, 4 and 8). Mean, Median, standard deviation (STD) and percentage of voxels detected with two vectors (%detected) are tabulated for the angle between the first and second detected vector (angle 1).

5.3.2.2 45° Phantom at 515 sampling directions with increasing levels of SNR

The 45° phantom was further evaluated by keeping the number of sampling directions fixed at 515 and varying the SNR by increasing the number of averages from 2 to 4 to 8. The results of this evaluation are presented in Fig.5.6. The angle statistics are shown in Fig.5.5 (g, h, i) and tabulated in Table 5.4. It can be appreciated from the vector maps in Fig.5.5 (a, b, c) and from the overall quality of representative ODFs in (d, e, f) that as SNR increases (from NEX= 2 to 4 to 8), the results are in closer agreement with the ground truth with lower standard deviation values (44.66 ± 5.25, 43.11 ± 3.78, 44.61 ± 1.67 at NEX=2, 4 and 8 respectively). Also, as SNR increases (from NEX= 2 to 4 to 8), the standard deviations decreases (from 5.25 to 3.78 to 1.67 at NEX=2, 4 and 8 respectively). Note that the overall performance of DSI with 515 samples is much better as compared to DSI with 257 samples. Even at low SNR levels (for example at NEX=2) DSI with 515 samples results in much closer agreement with the ground truth with lower standard deviation values (mean $\pm$ STD= 44.66 ± 5.25 at 515 samples) compared to the corresponding NEX=2 at 257 samples (mean $\pm$ STD= 44.04 ± 13.67) or NEX=8 at 515 samples (mean $\pm$ STD= 54.53 ± 17.07). Therefore,

given a choice between increasing NEX and increasing the number of samples (for a given scan time), results from this evaluation suggests increasing the number of samples is preferable.

Finally, as SNR increases (from NEX= 2 to 4 to 8), there is a concomitant decrease in the standard deviation values as expected (a decrease from 5.25 to 3.78 to 1.67 for NEX=2, 4, 8 respectively).

Fig.5.5: Results of Evaluation on 45° Phantom (using number of samples = 515 and NEX=2, 4 and 8). (a, b, c) vector map generated from deconvolved ODFs (from the 10x10 voxel region of interest = 100 voxels) corresponding to NEX=2, 4 and 8 respectively; (d, e, f) representative ODF (from the crossing region) after deconvolution corresponding to NEX=2, 4 and 8 respectively; (g, h, i) angles calculated between the first and second vectors for the 100 voxels corresponding to NEX=2, 4 and 8 respectively.

RESULTS			
45° with number of samples =515	NEX=2	NEX=4	NEX=8
mean	44.6695	43.1135	44.6123
median	47.2131	43.1932	45
standard deviation	5.2528	3.783	1.6709
% detected	99%	97%	100%

Table 5.4: Summary of Results of Evaluation on 45° Phantom (using number of samples = 515 and NEX=2, 4 and 8). Mean, Median, standard deviation (STD) and percentage of voxels detected with two vectors (%detected) are tabulated for the angle between the first and second detected vector (angle 1).

5.3.2.3 45° Phantom at fixed SNR and varying number of sampling points (123, 257 and 515)

The 45° phantom was further evaluated by keeping the SNR fixed (NEX=8) and varying the number of sampling directions by increasing from 123 to 257 to 515. The results of this evaluation are presented in Fig.5.6. The angle statistics are shown in Fig.5.6 (g, h, i) and tabulated in Table 5.5.

It can be appreciated from the vector maps in Fig.5.6 (a, b, c) and from the overall quality of representative ODFs in (d, e, f) that as number of samples increases from 123 to 257 to 515, the angular accuracy dramatically increases and reaches a value that is in very close agreement with the ground truth value of 45° for 515 samples. Notice that the standard deviations are also dramatically reduced (mean ± STD = 87.12 ± 21.24, 60.79 ± 13.63 and 44.61 ± 1.67 at number of of samples = 123, 257 and 515 respectively).

Again, deconvolution introduced spurious peaks in the case of both 123 samples and in some voxels in the 257 samples. Hence, deconvolution should be used with caution if the angular resolution of the data is low. However, deconvolution enhanced the detection of the

correct peaks when the angular resolution of the data was reasonably high (for example in the 515 case where deconvolution correctly enhanced the detection to 100%)
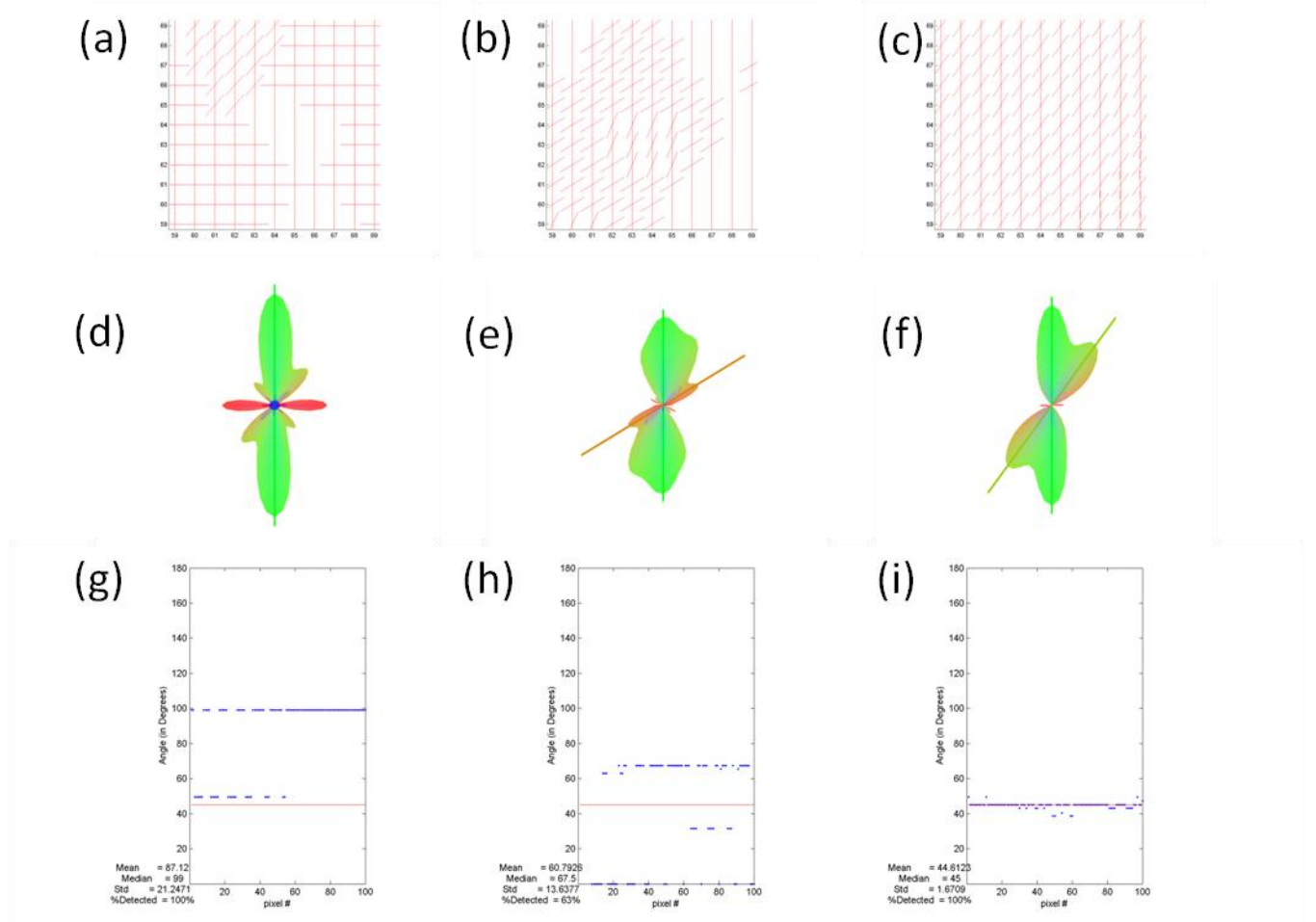
Fig.5.6: Results of Evaluation on 45° Phantom (with NEX= 8 and using number of samples = 123, 256 and 515). (a, b, c) vector map generated from deconvolved ODFs (from the 10x10 voxel region of interest = 100 voxels) corresponding to number of samples = 123, 256 and 515 respectively; (d, e, f) representative ODF (from the crossing region) after deconvolution corresponding to number of samples = 123, 256 and 515 respectively; (g, h, i) angles calculated between the first and second vectors for the 100 voxels corresponding to number of samples = 123, 256 and 515 respectively; (j, k, l) angles calculated between the second and third vectors for the 100 voxels corresponding to number of samples = 123, 256 and 515 respectively.

RESULTS			
45° with NEX=8	*Number of samples=123*	*Number of samples=257*	*Number of samples=515*
mean	87.12	60.7926	44.6123
median	99	67.5	45
standard deviation	21.2471	13.6377	1.6709
% detected	100%	63%	100%

Table 5.5: Summary of Results of Evaluation on 45° Phantom (with NEX= 8 and using number of samples = 123, 256 and 515). Mean, Median, standard deviation (STD) and percentage of voxels detected with two vectors (%detected) are tabulated for the angle between the first and second detected vector (angle 1).

5.3.3   Results of 60° Phantom

60° was evaluated with 257 sampling directions with increasing levels of SNR (achieved by increasing the NEX from 2 to 4 to 8). Additionally, the 60° phantom was evaluated with 515 sampling directions with increasing levels of SNR. The following two subsections presents the result of each evaluation for the 60° phantom.

5.3.3.1 60° Phantom at 257 sampling directions with increasing levels of SNR

The 60° phantom was evaluated by keeping the number of sampling directions fixed at 257 and varying the SNR varied by increasing the number of averages from 2 to 4 to 8. The results of this evaluation are presented in Fig.5.7. The angle statistics are shown in Fig.5.7 (g, h, i) for angle 1, (j, k, l) for angle 2 and tabulated in Table 5.6. It can be appreciated from the vector maps in Fig.5.7 (a, b, c) and from the overall quality of representative ODFs in (d, e, f) that as SNR increases (from NEX= 2 to 4 to 8), there is an overall qualitative improvement in crossing fibers detection efficiency although they are not in agreement with the ground truth, especially for the second angle since the standard deviations are noticeably high (18.46, 29.23, 15.894 for NEX= 2, 4, 8 respectively).

Although the mean and median values seem to be close to the ground truth for both angles (Table 5.6), these numerical values should be interpreted cautiously because a)standard deviations are fairly high and b)not all of the second vectors are detected for example at NEX=2; only 60% of the second vectors are detected. This percentage increased to 90% for NEX=4 and dropped to 70% at NEX=8.

Overall, there is an improvement in the crossing fiber detection efficiency for the number of samples = 257 at NEX=8 with lower standard deviation values for both first and second angles and small deviation from ground truth in their mean and median values (mean $\pm$ STD = 59.43 $\pm$ 6.86 and 63.59 $\pm$ 15.89 for angles 1 and 2 respectively).

Fig.5.7: Results of Evaluation on 60° Phantom (using number of samples = 257 and NEX=2, 4 and 8). (a, b, c) vector map generated from deconvolved ODFs (from the 10x10 voxel region of interest = 100 voxels) corresponding to NEX=2, 4 and 8 respectively; (d, e, f) representative ODF (from the crossing region) after deconvolution corresponding to NEX=2, 4 and 8 respectively; (g, h, i) angles calculated between the first and second vectors for the 100 voxels corresponding to NEX=2, 4 and 8 respectively; (j, k, l) angles calculated between the second and third vectors for the 100 voxels corresponding to NEX=2, 4 and 8 respectively.

[99]

RESULTS			
60° Angle1 with number of samples =257	2	4	8
mean	68.542	60.4296	59.4382
median	68.6146	59.5685	57.5
standard deviation	16.6358	8.6353	6.8692
% detected	100%	100%	100%

60° Angle2 with number of samples =257	NEX=2	NEX=4	NEX=8
mean	69.4462	66.9702	63.5983
median	69.5812	62.1695	60
standard deviation	18.4618	29.2308	15.893
% detected	68%	90%	74%

Table 5.6: Summary of Results of Evaluation on 60° phantom (using number of samples = 257 and NEX=2, 4 and 8). Mean, Median, standard deviation (STD) and percentage of voxels detected with two vectors (%detected) are tabulated for the angle between the first and second detected vector (angle 1) in (a) and for the angle between the second and third detected vector (angle 2) in (b).

5.3.3.2 60° Phantom at 515 sampling directions with increasing levels of SNR

The 60° phantom was evaluated by keeping the number of sampling directions fixed at 515 and varying the SNR varied by increasing the number of averages from 2 to 4 to 8. The results of this evaluation are presented in Fig.5.8. The angle statistics are shown in Fig.5.8 (g, h, i) for angle 1 and (j, k, l) for angle 2 and tabulated in Table 5.7. It can be appreciated from the vector maps in Fig.5.8 (a, b, c) and from the overall quality of representative ODFs in (d, e, f) that as SNR increases (from NEX= 2 to 4 to 8), there is an overall qualitative improvement in the crossing fiber detection efficiency although they are far from agreement with the ground truth especially for NEX=2 and NEX=4. However at NEX=8, there is a significant improvement in the crossing fibers detection with very low standard deviation for both angle 1 and angle 2 (mean ± STD = 59.8 ± 2.33 and 60.03 ±2.21 for angles 1 and 2 respectively).

[100]

Comparing the results of the two evaluations on the 60° phantom, it might seem that the mean values in evaluation with 515 sampling points are farther from ground truth than in evaluation with 257 sample points. However, a) overall standard deviations are much lower in evaluation with 515 sampling points versus evaluation with 257 sampling points for both the angles and across all SNR levels (with the exception at NEX=2 and NEX=4 where evaluation with 257 sampling points has slightly lower values) and b) the percent detection for both the first and second angle in evaluation with 515 sampling points are much higher (close to 100% for both the angles). This implies an overall improvement in the accuracy with increasing the number of samples from 257 to 515. Overall, the number of samples = 515 at NEX=8 performed the best both qualitatively and quantitatively (mean ± STD = 59.8 ± 2.33 and 60.03 ±2.21 for angles 1 and 2 respectively).
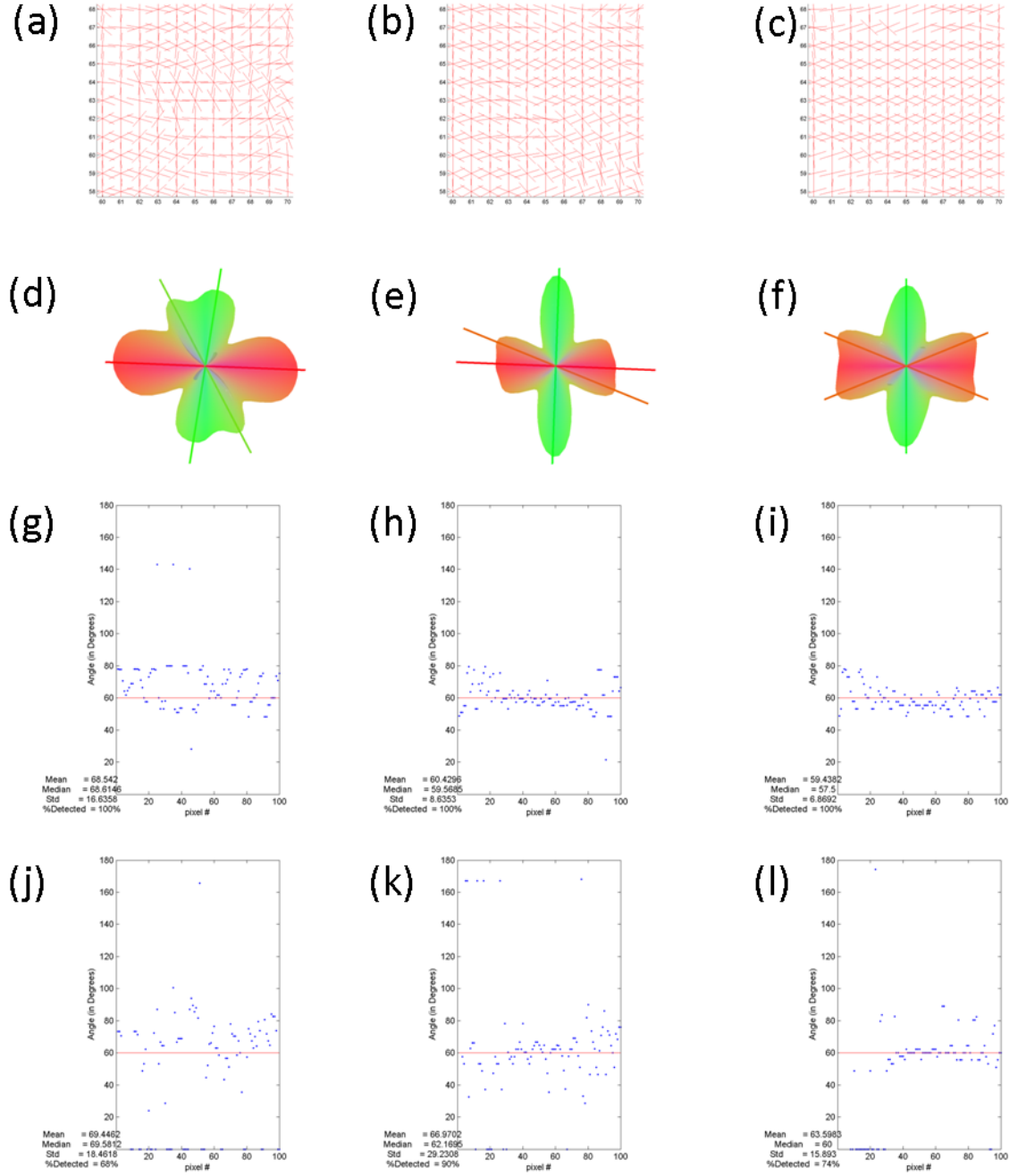
Fig.5.8: Results of Evaluation on 60° Phantom (using number of samples = 515 and NEX=2, 4 and 8). (a, b, c) vector map generated from deconvolved ODFs (from the 10x10 voxel region of interest = 100 voxels) corresponding to NEX=2, 4 and 8 respectively; (d, e, f) representative ODF (from the crossing region) after deconvolution corresponding to NEX=2, 4 and 8 respectively; (g, h, i) angles calculated between the first and second vectors for the 100 voxels corresponding to NEX=2, 4 and 8 respectively; (j, k, l) angles calculated between the second and third vectors for the 100 voxels corresponding to NEX=2, 4 and 8 respectively.

[102]

RESULTS			
60° Angle1 with number of samples =515	NEX=2	NEX=4	NEX=8
mean	39.6243	50.705	59.8009
median	42.8217	48.5	60
standard deviation	18.2773	9.8674	2.3363
% detected	100%	100%	100%

60° Angle2 with number of samples =515	NEX=2	NEX=4	NEX=8
mean	73.8221	73.3402	60.035
median	75.7839	73.4353	60
standard deviation	18.0351	9.0953	2.2132
% detected	98%	98%	100%

Table 5.7: Summary of Results of Evaluation on 60° phantom (using number of samples = 515 and NEX=2, 4 and 8). Mean, Median, standard deviation (STD) and percentage of voxels detected with two vectors (%detected) are tabulated for the angle between the first and second detected vector (angle 1) in (a) and for the angle between the second and third detected vector (angle 2) in (b).

5.4 Summary of Phantom Studies

The phantoms developed in this thesis were used to quantitatively evaluate the effect of the number of samples and SNR on the angular accuracy of DSI derived ODFs. As the number of sampling points increases, there is an overall improvement in the angular accuracy in DSI. At NEX=8 and number of samples=515, the crossing angles reach values very close to the ground truth for both 45° and 60° phantoms. Also, given a choice between increasing NEX and increasing the number of samples (for a given scan time), increasing the number of samples appears to yield more accurate results. It is important to carefully investigate the overall vector map to judge the results, as the mean values may be misleading. Standard deviations help in identifying potential issues. Finally, deconvolution

in general is beneficial for DSI as a post-processing step; however, deconvolution should be used with caution if the angular resolution or SNR of the data is low.

Similar evaluations can be performed with these phantoms to test the effect of other acquisition parameters (for example effect of b-value and effect of slice thickness) and for evaluating different acquisition and reconstruction schemes.

5.5 METHODS (Human subjects)

MRI Acquisition and Analysis

Data was acquired on 10 normal human subjects (7 males and 3 females; 35±11 yrs, range 25 to 59 yrs) using an 8-channel SENSE head coil on a 3T MRI scanner (Achieva, Philips Medical Systems, Best, Netherlands). Multi-slice, diffusion-weighted images were acquired using a single shot spin echo EPI sequence with the following sequence parameters: TE/TR=95/11400 msec; FOV=220x240 mm2; matrix=256x256; spatial resolution=0.9375x0.9375 mm/px; Nslices=28 (covering the whole brain); slice thickness = 4 mm; NEX=1; bmax=9700 s/mm2 ; gridsize of 4 (corresponding to 257 diffusion weighted images) was used and the total DSI data acquisition time was 48 min. Because of the long scan times, data was not acquired with a larger grid size or more number of averages.Data was analyzed with the methodologies developed in the previous chapter. Deconvolution was performed with spherical harmonic order ℓ=10, and regularization factor λ=0.01.

5.6 RESULTS (Human subjects)

5.6.1   Effect of Deconvolution on single fiber region

Fig.5.9. shows a representative ODF from corpus callosum (CC) region before (Fig.9 a) and after deconvolution (Fig.9 b). The deconvolution not only did not affect the orientation of single coherent fiber bundles, such as callosal fibers, but in fact enhanced it (sharper peaks). Fig.10 (a) presents a vector map (and a zoomed version from the callosal region) derived from the ODFs before deconvolution (Fig.10 b) and after deconvolution (Fig.10 c) to underscore this point.
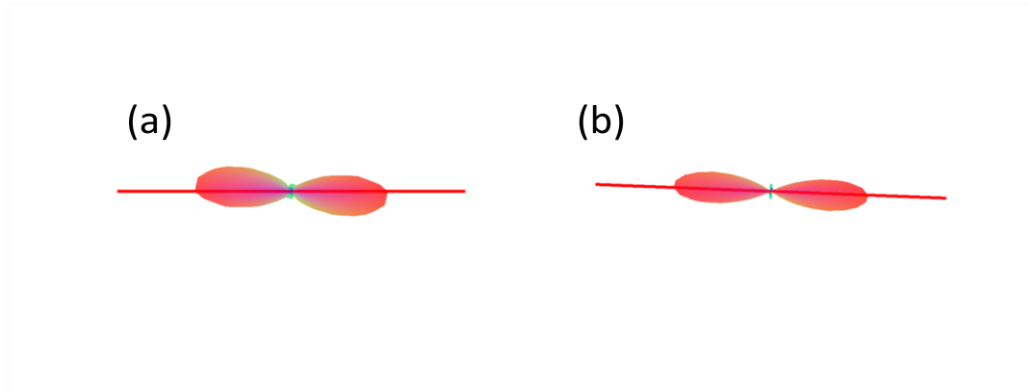
Fig.5.9: Representative ODF from CC region. (a) Representative ODF before deconvolution; (b) Representative ODF after deconvolution. Deconvolution doesn't adversely affect the directionality of single fiber regions and in turn enhances it.
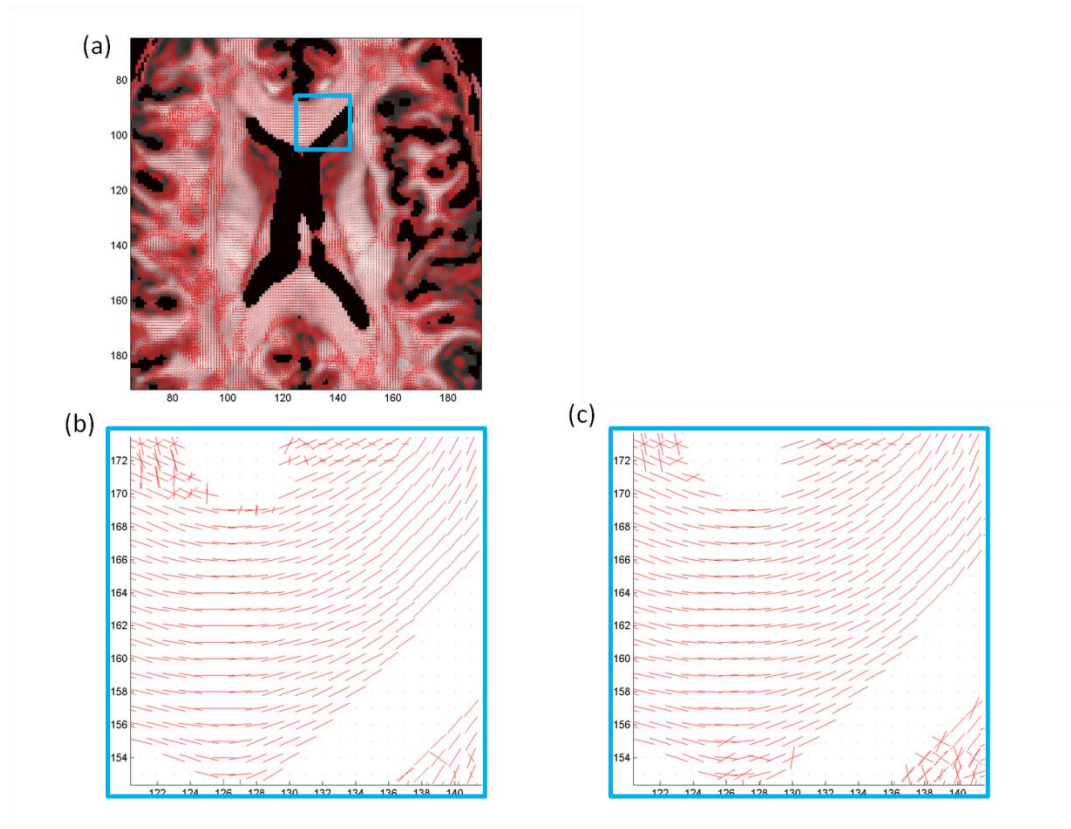
Fig.5.10: Representative Vector Map (derived from ODFs from CC) Region. (a) Vector map overlaid on DA intensity map; (b) Zoomed vector maps before deconvolution; (c) Zoomed vector maps after deconvolution. Deconvolution doesn't adversely affect the directionality of single fiber regions and in turn enhances it.

5.6.2 Effect of Deconvolution on crossing fiber region

Representative ODFs from a crossing fiber region of in centrum semiovale are shown before (Fig.5.11 a) and after deconvolution (Fig.5.11 b). Centrum semiovale is a crossing fiber region in the human brain known to consist of crossing fibers in three different orientations from corona radiata (superior-inferior), corpus callosum (left-right) and superior longitudinal fasciculus (anterior-posterior)). Deconvolution cleaned up the spurious fibers (based on the known anatomy in this region).

[106]
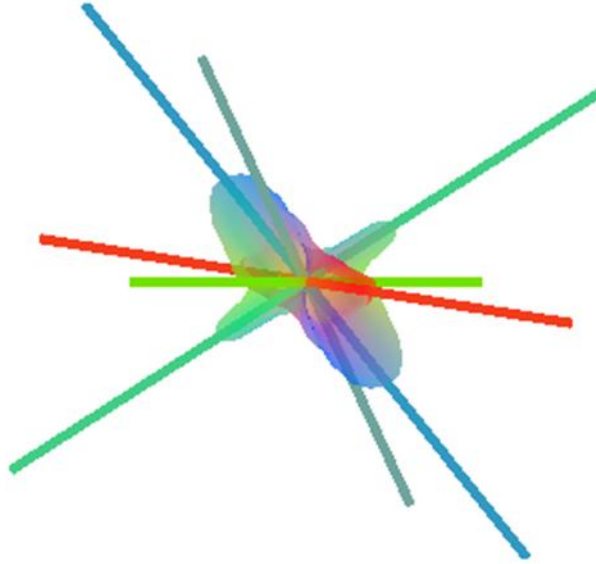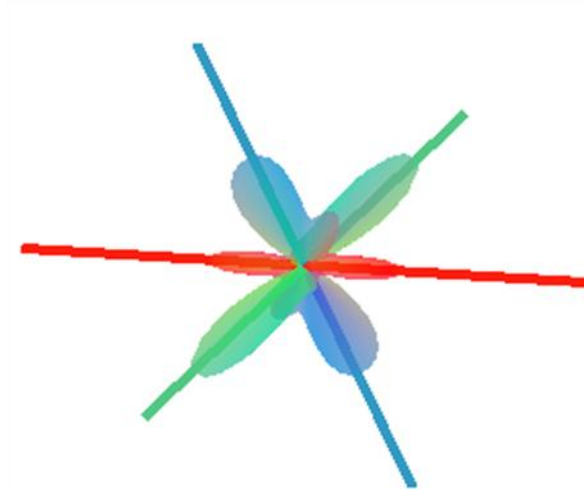
Fig.5.11: Representative Pair of ODF from Centrum Semiovale. (a) Representative ODF Before deconvolution;(b) Representative ODF after deconvolution. Deconvolution cleans up the spurious fibers, since the anatomy in this region is known. (Centrum semiovale is a crossing fiber region in the human brain known to consist of crossing fibers in three different orientations from Corona Radiata (blue), Corpus Callosum (red) and Superior Longitudinal Fasciculus (green)),

5.6.3   Diffusion Anisotropy (DA) Maps

The Diffusion Anisotropy (DA) maps were generated after deconvolution as described in the previous chapter. A representative DA map from a central axial slice (slice 14 out of 28 slices) is shown in Fig.12. The color code indicates the direction of the principal direction vector obtained from the maximum of the ODF (determined by the local maximum method).
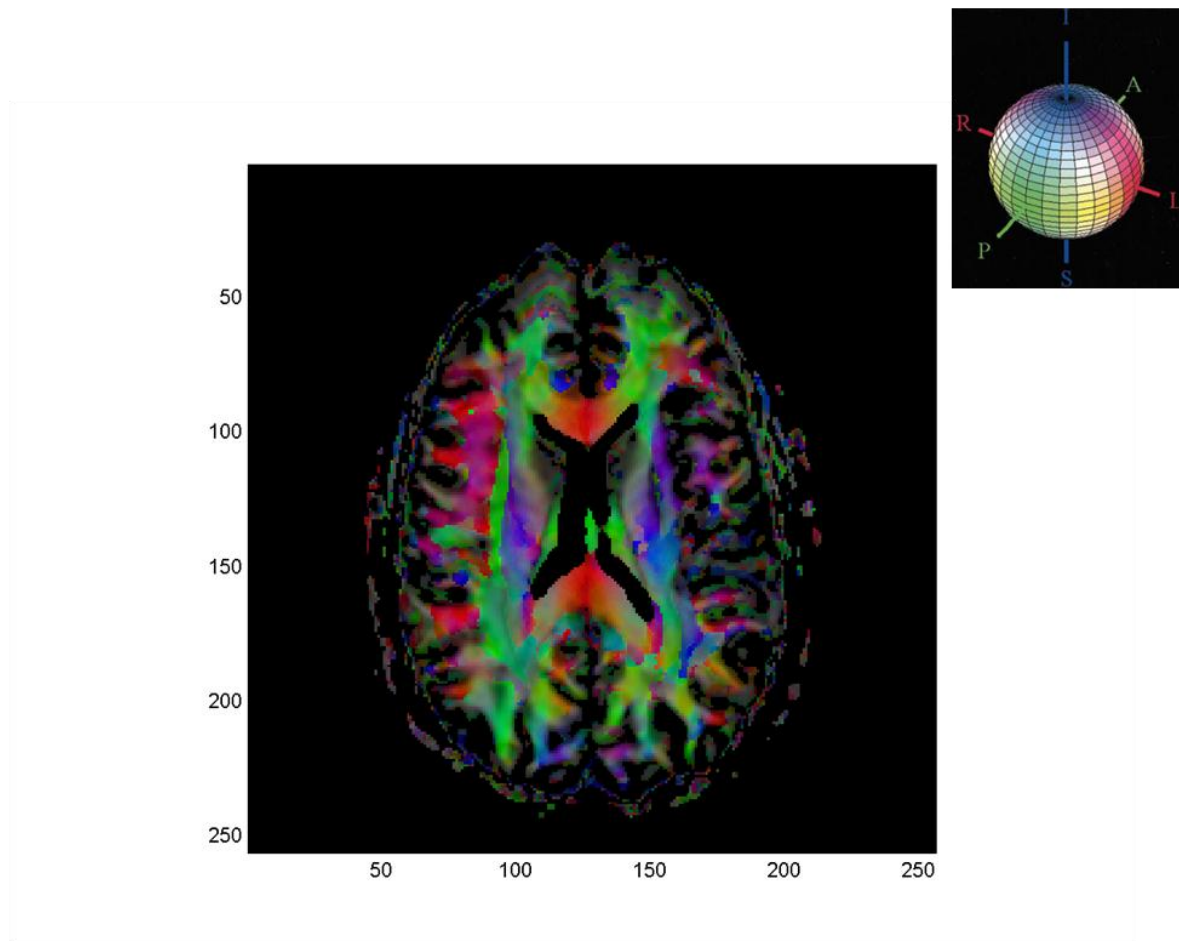
Fig.5.12: DA Map of a Normal Human Subject. The color is encoded by the direction of the principle direction vector from the maxima of the ODF (determined by the local maxima method). The color scheme is represented by the standard RGB sphere in inset (red: left-right; green: anterior-posterior; blue: superior-inferior.

5.6.4 Fiber Tracking

Fiber tracking was performed using the vector maps derived from ODFs both before and after deconvolution for comparison. Fiber tracking was performed based on the algorithm described in Chapter 4 (Note [22] recommends a step-size of $< ½$ the voxel size. Hence, a step-size of 0.4 was used given our voxel size of 4 mm (step-size of <2 mm was recommended). Also, a typically threshold value of Øc<0.5 radian (i.e. 30)was used. A DA threshold (DAthesh) value of 0.25 was chosen based on the range of DA values in the gray matter of our data-sets.

Fig.5.13 presents the results of fiber tracking from seed points placed in the corpus callosum region highlighted in (a). The tracts before and after deconvolution are shown in (b) and (c), respectively. The seeds were then extended to the entire corpus callosum region (identified manually on the sagittal slices) and the results are shown in Fig.5.14. Fiber tracts before deconvolution are shown in (Fig.5.14 a) and fiber tracts after deconvolution are shown in (Fig.5.14b). Overall, with deconvolution, the tracts appear to be better defined and more coherent.

Fiber tracking results from the centrum semiovale region which is known to consist of three-way fiber crossing crossings from corona radiata (blue), corpus callosum (red) and superior longitudinal fasciculus (green) are presented in Fig.5.15 and Fig.5.16. Fig.5.15 shows this region (which is identified from the published literature [15] and highlighted on the DA intensity map in the coronal plane (Fig.5.15 a). The resultant tracts (after deconvolution) are shown overlaid in (Fig.5.15 b). The tracts before and after deconvolution are shown in (Fig.5.16 a and b, respectively) for comparison. The tracts after deconvolution appear cleaner and depict the known three-way anatomical connectivity between three-way

fiber crossing connectivity. Such connectivity was not clearly depicted and missed by using the vector set of ODFs without deconvolution.
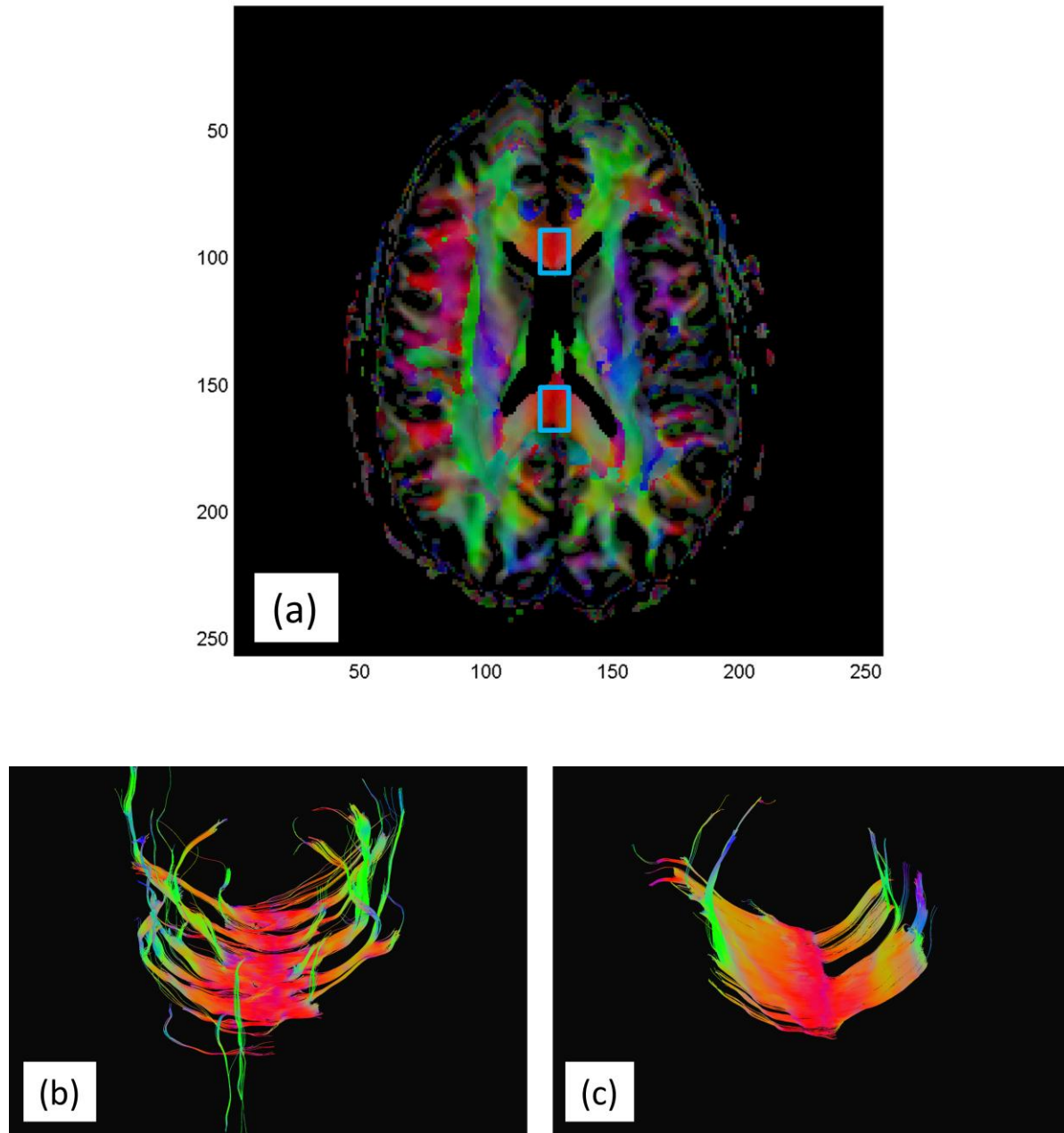
Fig.5.13: Fiber Tracking Results from CC Region. (a) Placement of seed points; (b) Fiber tracts before deconvolution; (c) Fiber tracts after deconvolution.
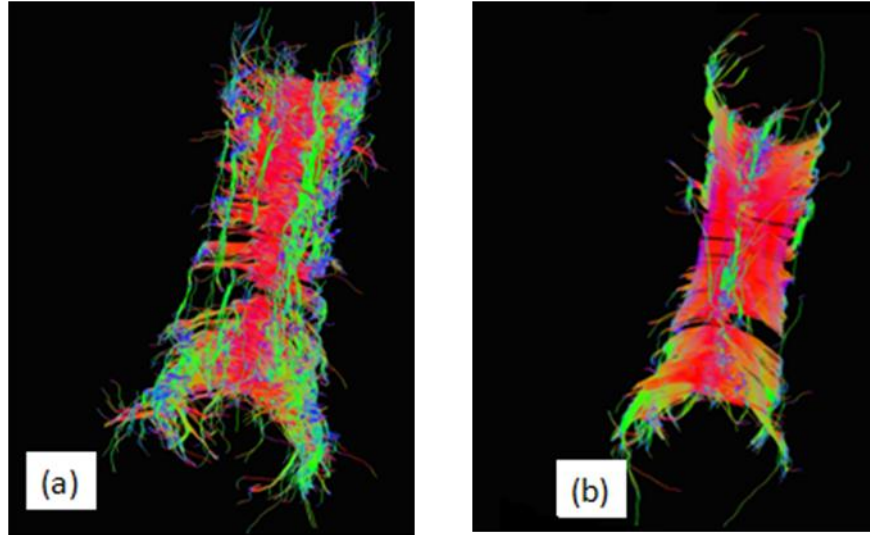
Fig.5.14: Fiber Tracking Results from a Seed Points placed in the entire CC. (a) Tracts before deconvolution; (b) tracts after deconvolution.
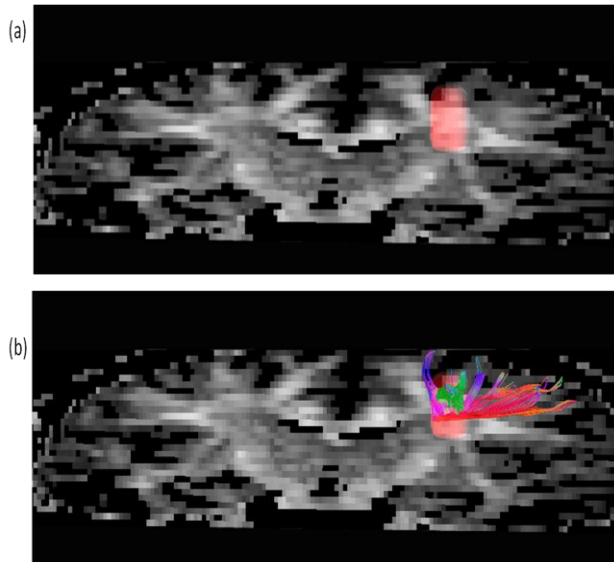
Fig.5.15: Fiber Tracking Results from Centrum Semiovale region. (a) The region where the seeds are placed is highlighted (in red) on the DA intensity map; (b) The resultant tracts after deconvolution. (zoomed version of this tract is shown in Fig.16 b).
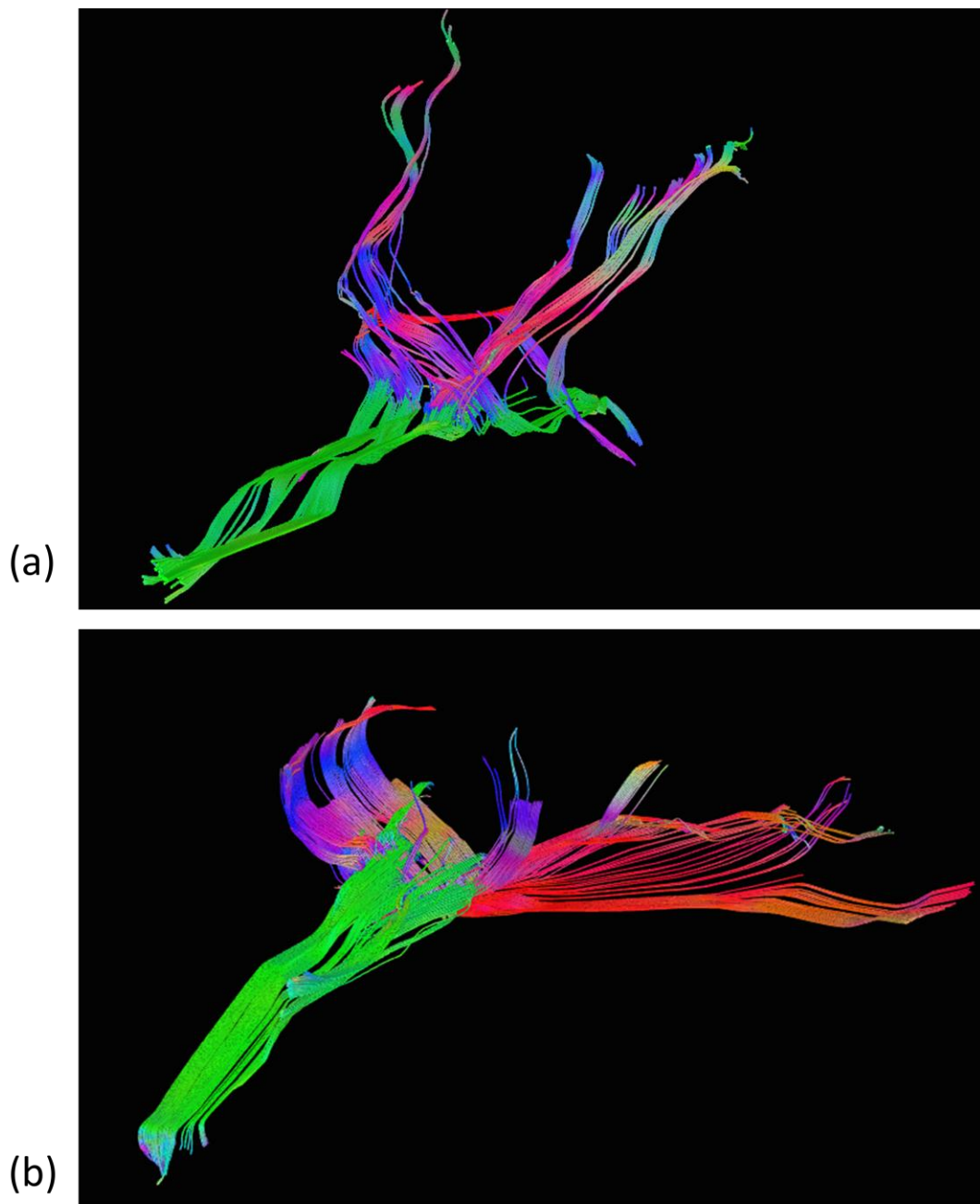
Fig.5.16: Fiber Tracking Results from Centrum Semiovale Region (zoom). (a) Fiber tracts before deconvolution; (b) tracts after deconvolution. Without deconvolution, the three crossing fibers were not getting detected. Also, there is a qualitative improvement in the tracts after deconvolution in terms of the tracts being better defined and more coherent.

5.7 Summary of Human Studies

The purpose of the human studies was not quantitative evaluation, but to qualitatively evaluate the performance of the deconvolution. Overall, with deconvolution, the tracts appear to be better defined and coherent, as shown from the fiber tracking results from seed points placed in corpus callosum. Also, the deconvolution improved the detection of the three crossing fibers from the centrum semiovale region.

5.8 SUMMARY

This chapter presented the validation of the DSI analysis described earlier using the phantoms that were developed as a part of this thesis work. Specifically, quantitative evaluation of angular accuracy of the DSI derived ODF using these phantoms was presented. The consequence of DSI acquisition parameters on the angular resolution in phantoms was quantified. The improvement in these regions by applying deconvolution was demonstrated. In addition, the applicability of the developed methodologies on normal human subjects was presented qualitatively. Known regions of human brain consisting of single fibers and crossing fibers were highlighted. Deconvolution seems to improve the fiber delineation and detection from these regions.

CHAPTER 6 – Conclusions and Future Directions

In this dissertation, I have designed and constructed novel diffusion phantoms, including three fiber crossings, and employed post-processing techniques in order to systematically validate and optimize (DSI)-derived fiber ODFs in the crossing regions on a clinical 3T MR scanner, and develop user-friendly software for DSI data reconstruction and analysis.

Two phantoms with a fixed crossing fiber configuration of two crossing fibers at 90° and 45° respectively, along with a phantom with three crossing fibers at 60° were constructed. Phantom construction involved novel hollow plastic capillaries designed to obtain a higher packing density than the previously reported hollow capillary phantoms. Also, a novel placeholder was designed for keeping the capillaries in a preset orientation forming a number of interleaved parallel layers resulting in fibers crossing at the desired angle. T2-weighted MRI results on these phantoms demonstrated high SNR, homogeneous signal and absence of air bubbles.

A technique to de-convolve the response function of an individual peak from the overall ODF was also implemented. The technique involves representing the DSI derived ODF with its spherical harmonic coefficients and performing the deconvolution using the properties of Funk-Hecke theorem. The deconvolution methodology greatly improved the angular resolution of the otherwise un-resolvable peaks in the ODF. The effect of DSI acquisition

parameters and SNR on the resultant angular accuracy of DSI on the clinical scanner was studied and quantified using the phantoms.

With a high angular direction sampling and reasonable levels of SNR, quantification of a crossing region with 10x10 pixels in the 90°, 45° and 60° phantoms resulted in a successful detection of angular information with mean ± SD of 86.93 ± 2.65, 44.61 ± 1.6° and 60.03 ±2.21° respectively, while simultaneously sharpening the ODFs in regions containing single fibers. As the number of sampling points and SNR increases, there is an overall improvement in the angular accuracy in DSI. Also, given a choice between increasing NEX and increasing the number of samples (for a given scan time), increasing the number of samples appears to yield more accurate results. Deconvolution in general is beneficial for DSI as a post-processing step; however, deconvolution should be used with caution if the angular resolution or SNR of the data is low. Similar evaluations can be performed with these phantoms to test the effect of other acquisition parameters (for example effect of b-value and effect of slice thickness).

The proposed deconvolution methodology significantly improved the angular accuracy of the crossing fiber ODFs obtained from DSI. This deconvolution methodology is directly applicable to ODFs obtained from any other ODF based high angular resolution diffusion imaging techniques. Given a reasonable angular direction sampling and reasonable levels of SNR, inclusion of deconvolution in the post-processing ensures enhanced angular resolution i.e. sharper peaks of the ODF. In this thesis, the fiber tracking was performed using a deterministic algorithm. However, the probabilistic tracking is likely to benefit more with the improved angular resolution in the ODFs obtained using the deconvolution technique,

since probabilistic tracking is likely to benefit from lesser and correct fiber orientations to choose from at each step.

Finally, the applicability of these methodologies on normal human subjects was demonstrated. The improvement in delineating known crossing fiber regions by applying deconvolution, followed by fiber tracking results were studied qualitatively.

An in-house software package in MATLAB which streamlines the data reconstruction and analysis for DSI with easy to use graphical user interface was also developed. This software package can be easily extended in functionality since it is highly modular in design.

The phantoms developed in this dissertation offer a means of providing ground truth for validation of various diffusion models (particularly the ones that aims to resolve the crossing fibers), evaluation of different acquisition or reconstruction schemes and validation of tractography algorithms. For example, the acquisition time can be reduced by truncating the number of samples and filling the q-space using the mathematical relationship and exploiting the q-space symmetry. The minimum number of sampling points can be validated using the phantoms. Also, an interesting study would be to compare DSI with q-ball, using the phantoms developed, to quantitatively evaluate the performance of these comparable q-space sampling schemes simultaneously on the clinical scanner. Another future direction would be to evaluate the tractography systematically in humans, compare rigorously the fiber tracts obtained with DTI and HARDI techniques and determine the fiber compromise in diseases such as Multiple Sclerosis (MS).

Overall, this dissertation sheds further light on the viability of using DSI in a clinical setting using ground truth phantoms. The main contributions of this thesis were:

- Validation of the angular resolution of DSI against the known ground truth diffusion phantom on a clinical 3T scanner.
- Design and construction of novel diffusion phantoms including a three fiber crossing phantom.
- Implementation of a de-convolution based technique for post-processing DSI data.
- Development of software tools for automated DSI post-processing, image reconstruction and analysis.

REFERENCES

1.   Wehrli, F.W., *On the 2003 Nobel Prize in medicine or physiology awarded to Paul C. Lauterbur and Sir Peter Mansfield.* Magn Reson Med, 2004. **51**(1): p. 1-3.

2.   Basser, P.J., J. Mattiello and D. LeBihan, *MR diffusion tensor spectroscopy and imaging.* Biophys J, 1994. **66**(1): p. 259-67.

3.   Basser, P.J. and D.K. Jones, *Diffusion-tensor MRI: theory, experimental design and data analysis - a technical review.* NMR Biomed, 2002. **15**(7-8): p. 456-67.

4.   Miller, D.H., R.I. Grossman, S.C. Reingold and H.F. McFarland, *The role of magnetic resonance techniques in understanding and managing multiple sclerosis.* Brain, 1998. **121 (Pt 1)**: p. 3-24.

5.   Hess, C.P. and P. Mukherjee, *Visualizing White Matter Pathways in the Living Human Brain: Diffusion Tensor Imaging and Beyond.* Neuroimaging Clinics of North America, 2007. **17**(4): p. 407-426.

6.   Alexander, D.C., *Multiple-fiber reconstruction algorithms for diffusion MRI.* Ann N Y Acad Sci, 2005. **1064**: p. 113-33.

7.   Ciccarelli, O., M. Catani, H. Johansen-Berg, C. Clark and A. Thompson, *Diffusion-based tractography in neurological disorders: concepts, applications, and future developments.* The Lancet Neurology, 2008. **7**(8): p. 715-727.

8.   Mori, S. and P.C. van Zijl, *Fiber tracking: principles and strategies - a technical review.* NMR Biomed, 2002. **15**(7-8): p. 468-80.

9.   Sundgren, P.C., Q. Dong, D. Gomez-Hassan, S.K. Mukherji, P. Maly and R. Welsh, *Diffusion tensor imaging of the brain: review of clinical applications.* Neuroradiology, 2004. **46**(5): p. 339-50.

10. Ge, Y., M. Law and R.I. Grossman, *Applications of diffusion tensor MR imaging in multiple sclerosis.* Ann N Y Acad Sci, 2005. **1064**: p. 202-19.

11. Neil, J., J. Miller, P. Mukherjee and P.S. Huppi, *Diffusion tensor imaging of normal and injured developing human brain - a technical review.* NMR Biomed, 2002. **15**(7-8): p. 543-52.

12. Hagmann, P., L. Cammoun, X. Gigandet, S. Gerhard, P.E. Grant, V. Wedeen, R. Meuli, J.P. Thiran, C.J. Honey and O. Sporns, *MR connectomics: Principles and challenges.* J Neurosci Methods, 2010. **194**(1): p. 34-45.

13. Tuch, D.S., *Q-ball imaging.* Magn Reson Med, 2004. **52**(6): p. 1358-72.

14. Lenglet, C., J.S. Campbell, M. Descoteaux, G. Haro, P. Savadjiev, D. Wassermann, A. Anwander, R. Deriche, G.B. Pike, G. Sapiro, K. Siddiqi and P.M. Thompson, *Mathematical methods for diffusion MRI processing.* Neuroimage, 2009. **45**(1 Suppl): p. S111-22.

15. Tuch, D.S., T.G. Reese, M.R. Wiegell and J.W. Van, *Diffusion MRI of Complex Neural Architecture.* Neuron, 2003. **40**(5): p. 885-895.

16. Descoteaux, M., E. Angelino, S. Fitzgibbons and R. Deriche, *Regularized, fast, and robust analytical Q-ball imaging.* Magn Reson Med, 2007. **58**(3): p. 497-510.

17. Wedeen, V.J., P. Hagmann, W.Y. Tseng, T.G. Reese and R.M. Weisskoff, *Mapping complex tissue architecture with diffusion spectrum magnetic resonance imaging.* Magn Reson Med, 2005. **54**(6): p. 1377-86.

18. Cheng, J., A. Ghosh, R. Deriche and T. Jiang, *Model-free, regularized, fast, and robust analytical orientation distribution function estimation.* Med Image Comput Comput Assist Interv, 2010. **13**(Pt 1): p. 648-56.

19. Canales-Rodriguez, E.J., L. Melie-Garcia and Y. Iturria-Medina, *Mathematical description of q-space in spherical coordinates: exact q-ball imaging.* Magn Reson Med, 2009. **61**(6): p. 1350-67.

20. Michailovich, O. and Y. Rathi, *On approximation of orientation distributions by means of spherical ridgelets.* IEEE Trans Image Process, 2010. **19**(2): p. 461-77.

21. Tuch, D.S., T.G. Reese, M.R. Wiegell, N. Makris, J.W. Belliveau and V.J. Wedeen, *High angular resolution diffusion imaging reveals intravoxel white matter fiber heterogeneity.* Magn Reson Med, 2002. **48**(4): p. 577-82.

22. Wedeen, V.J., R.P. Wang, J.D. Schmahmann, T. Benner, W.Y. Tseng, G. Dai, D.N. Pandya, P. Hagmann, H. D'Arceuil and A.J. de Crespigny, *Diffusion spectrum magnetic resonance imaging (DSI) tractography of crossing fibers.* Neuroimage, 2008. **41**(4): p. 1267-77.

23. Schmahmann, J.D., D.N. Pandya, R. Wang, G. Dai, H.E. D'Arceuil, A.J. de Crespigny and V.J. Wedeen, *Association fibre pathways of the brain: parallel observations from diffusion spectrum imaging and autoradiography.* Brain, 2007. **130**(Pt 3): p. 630-53.

24. Takahashi, E., G. Dai, R. Wang, K. Ohki, G.D. Rosen, A.M. Galaburda, P.E. Grant and V.J. Wedeen, *Development of cerebral fiber pathways in cats revealed by diffusion spectrum imaging.* Neuroimage, 2010. **49**(2): p. 1231-40.

25. Kuo, L.W., C.Y. Lee, J.H. Chen, V.J. Wedeen, C.C. Chen, H.H. Liou and W.Y. Tseng, *Mossy fiber sprouting in pilocarpine-induced status epilepticus rat hippocampus: a correlative study of diffusion spectrum imaging and histology.* Neuroimage, 2008. **41**(3): p. 789-800.

26.   Lin, C.P., V.J. Wedeen, J.H. Chen, C. Yao and W.Y. Tseng, *Validation of diffusion spectrum magnetic resonance imaging with manganese-enhanced rat optic tracts and ex vivo phantoms.* Neuroimage, 2003. **19**(3): p. 482-95.

27.   Gilbert, R.J., L.H. Magnusson, V.J. Napadow, T. Benner, R. Wang and V.J. Wedeen, *Mapping complex myoarchitecture in the bovine tongue with diffusion-spectrum magnetic resonance imaging.* Biophys J, 2006. **91**(3): p. 1014-22.

28.   Yeh, C.H., K.H. Cho, H.C. Lin, J.J. Wang and C.P. Lin, *Reduced encoding diffusion spectrum imaging implemented with a bi-Gaussian model.* IEEE Trans Med Imaging, 2008. **27**(10): p. 1415-24.

29.   Kuo, L.W., J.H. Chen, V.J. Wedeen and W.Y. Tseng, *Optimization of diffusion spectrum imaging and q-ball imaging on clinical MRI system.* Neuroimage, 2008. **41**(1): p. 7-18.

30.   Nezamzadeh, M., V.J. Wedeen, R. Wang, Y. Zhang, W. Zhan, K. Young, D.J. Meyerhoff, M.W. Weiner and N. Schuff, *In-vivo investigation of the human cingulum bundle using the optimization of MR diffusion spectrum imaging.* Eur J Radiol, 2010. **75**(1): p. e29-36.

31.   Descoteaux, M., R. Deriche, T.R. Knosche and A. Anwander, *Deterministic and probabilistic tractography based on complex fibre orientation distributions.* IEEE Trans Med Imaging, 2009. **28**(2): p. 269-86.

32.   Tournier, J.D., F. Calamante, D.G. Gadian and A. Connelly, *Direct estimation of the fiber orientation density function from diffusion-weighted MRI data using spherical deconvolution.* Neuroimage, 2004. **23**(3): p. 1176-85.

33. Canales-Rodriguez, E.J., Y. Iturria-Medina, Y. Aleman-Gomez and L. Melie-Garcia, *Deconvolution in diffusion spectrum imaging.* Neuroimage, 2010. **50**(1): p. 136-49.

34. Yeh, F.C., V.J. Wedeen and W.Y. Tseng, *Estimation of fiber orientation and spin density distribution by diffusion deconvolution.* Neuroimage, 2011. **55**(3): p. 1054-62.

35. Poupon, C., B. Rieul, I. Kezele, M. Perrin, F. Poupon and J.F. Mangin, *New diffusion phantoms dedicated to the study and validation of high-angular-resolution diffusion imaging (HARDI) models.* Magn Reson Med, 2008. **60**(6): p. 1276-83.

36. Fieremans, E., Y. De Deene, S. Delputte, M.S. Ozdemir, E. Achten and I. Lemahieu, *The design of anisotropic diffusion phantoms for the validation of diffusion weighted magnetic resonance imaging.* Phys Med Biol, 2008. **53**(19): p. 5405-19.

37. Pullens, P., A. Roebroeck and R. Goebel, *Ground truth hardware phantoms for validation of diffusion-weighted MRI applications.* J Magn Reson Imaging, 2010. **32**(2): p. 482-8.

38. Reischauer, C., P. Staempfli, T. Jaermann and P. Boesiger, *Construction of a temperature-controlled diffusion phantom for quality control of diffusion measurements.* J Magn Reson Imaging, 2009. **29**(3): p. 692-8.

39. Perrin, M., C. Poupon, B. Rieul, P. Leroux, A. Constantinesco, J.F. Mangin and D. Lebihan, *Validation of q-ball imaging with a diffusion fibre-crossing phantom on a clinical scanner.* Philos Trans R Soc Lond B Biol Sci, 2005. **360**(1457): p. 881-91.

40. Le Bihan, D., *Looking into the functional architecture of the brain with diffusion MRI.* Nat Rev Neurosci, 2003. **4**(6): p. 469-80.

41.   Hagmann, P., L. Jonasson, P. Maeder, J.P. Thiran, V.J. Wedeen and R. Meuli, *Understanding diffusion MR imaging techniques: from scalar diffusion-weighted imaging to diffusion tensor imaging and beyond.* Radiographics, 2006. **26 Suppl 1**: p. S205-23.

42.   Bloch, F., *Nuclear Induction.* Physical Review, 1946. **70**(7-8): p. 460.

43.   Hahn, E.L., *Spin Echoes.* Physical Review, 1950. **80**(4): p. 580.

44.   Stejskal, E.O. and J.E. Tanner, *Spin Diffusion Measurements: Spin Echoes in the Presence of a Time-Dependent Field Gradient.* The Journal of Chemical Physics, 1965. **42**(1): p. 288-292.

45.   Carr, H.Y. and E.M. Purcell, *Effects of Diffusion on Free Precession in Nuclear Magnetic Resonance Experiments.* Physical Review, 1954. **94**: p. 630-638.

46.   Bammer, R., *Basic principles of diffusion-weighted imaging.* Eur J Radiol, 2003. **45**(3): p. 169-84.

47.   Beaulieu, C., *The basis of anisotropic water diffusion in the nervous system - a technical review.* NMR Biomed, 2002. **15**(7-8): p. 435-55.

48.   Basser, P.J., J. Mattiello and D. LeBihan, *Estimation of the effective self-diffusion tensor from the NMR spin echo.* J Magn Reson B, 1994. **103**(3): p. 247-54.

49.   Basser, P.J. and C. Pierpaoli, *Microstructural and physiological features of tissues elucidated by quantitative-diffusion-tensor MRI.* J Magn Reson B, 1996. **111**(3): p. 209-19.

50.   Pierpaoli, C. and P.J. Basser, *Toward a quantitative assessment of diffusion anisotropy.* Magn Reson Med, 1996. **36**(6): p. 893-906.

51.   Hasan, K.M., D.L. Parker and A.L. Alexander, *Comparison of gradient encoding schemes for diffusion-tensor MRI.* J Magn Reson Imaging, 2001. **13**(5): p. 769-80.

52.   Callaghan, P.T., *Principles of Nuclear Magnetic Resolnance Microscopy. .* Oxford University Press, Oxford, 1991.

53.   Callaghan, P.T., *Principles of nuclear magnetic resonance microscopy*. Paperback ed. 1993, Oxford: Clarendon Press. XVII, 492 s.

54.   King, M.D., J. Houseman, S.A. Roussel, N. van Bruggen, S.R. Williams and D.G. Gadian, *q-Space imaging of the brain.* Magn Reson Med, 1994. **32**(6): p. 707-13.

55.   Tournier, J.D., F. Calamante and A. Connelly, *Robust determination of the fibre orientation distribution in diffusion MRI: non-negativity constrained super-resolved spherical deconvolution.* Neuroimage, 2007. **35**(4): p. 1459-72.

56.   Tournier, J.D., C.H. Yeh, F. Calamante, K.H. Cho, A. Connelly and C.P. Lin, *Resolving crossing fibres using constrained spherical deconvolution: validation using diffusion-weighted imaging phantom data.* Neuroimage, 2008. **42**(2): p. 617-25.

57.   Jeurissen, B., A. Leemans, D.K. Jones, J.D. Tournier and J. Sijbers, *Probabilistic fiber tracking using the residual bootstrap with constrained spherical deconvolution.* Hum Brain Mapp, 2011. **32**(3): p. 461-79.

58.   Khachaturian, M.H., J.J. Wisco and D.S. Tuch, *Boosting the sampling efficiency of q-Ball imaging using multiple wavevector fusion.* Magn Reson Med, 2007. **57**(2): p. 289-96.

59.   Assaf, Y. and P.J. Basser, *Composite hindered and restricted model of diffusion (CHARMED) MR imaging of the human brain.* Neuroimage, 2005. **27**(1): p. 48-58.

60.   Canales-Rodriguez, E.J., C.P. Lin, Y. Iturria-Medina, C.H. Yeh, K.H. Cho and L. Melie-Garcia, *Diffusion orientation transform revisited.* Neuroimage, 2010. **49**(2): p. 1326-39.

61.   Ozarslan, E., T.M. Shepherd, B.C. Vemuri, S.J. Blackband and T.H. Mareci, *Resolution of complex tissue microarchitecture using the diffusion orientation transform (DOT).* Neuroimage, 2006. **31**(3): p. 1086-103.

62.   Ozarslan, E. and T.H. Mareci, *Generalized diffusion tensor imaging and analytical relationships between diffusion tensor imaging and high angular resolution diffusion imaging.* Magn Reson Med, 2003. **50**(5): p. 955-65.

63.   Ghosh, A., M. Descoteaux and R. Deriche, *Riemannian framework for estimating symmetric positive definite 4th order diffusion tensors.* Med Image Comput Comput Assist Interv, 2008. **11**(Pt 1): p. 858-65.

64.   Alexander, D.C., G.J. Barker and S.R. Arridge, *Detection and modeling of non-Gaussian apparent diffusion coefficient profiles in human brain data.* Magn Reson Med, 2002. **48**(2): p. 331-40.

65.   Wu, Y.C. and A.L. Alexander, *Hybrid diffusion imaging.* Neuroimage, 2007. **36**(3): p. 617-29.

66.   Jian, B., B.C. Vemuri, E. Ozarslan, P.R. Carney and T.H. Mareci, *A novel tensor distribution model for the diffusion-weighted MR signal.* Neuroimage, 2007. **37**(1): p. 164-76.

67.   Subakan, O., B. Jian, B.C. Vemuri and C.E. Vallejos, *Feature Preserving Image Smoothing Using a Continuous Mixture of Tensors.* Proc IEEE Int Conf Comput Vis, 2007. **11**: p. nihpa163297.

[125]

68.   Jian, B. and B.C. Vemuri, *Multi-fiber reconstruction from diffusion MRI using mixture of Wisharts and sparse deconvolution.* Inf Process Med Imaging, 2007. **20**: p. 384-95.

69.   McGraw, T., B.C. Vemuri, B. Yezierski and T. Mareci, *Von Mises-Fisher Mixture Model of the Diffusion Odf.* Proc IEEE Int Symp Biomed Imaging, 2006. **2006**: p. 65-68.

70.   Parker, G.J. and D.C. Alexander, *Probabilistic anatomical connectivity derived from the microscopic persistent angular structure of cerebral tissue.* Philos Trans R Soc Lond B Biol Sci, 2005. **360**(1457): p. 893-902.

71.   Jansons, K.M. and D.C. Alexander, *Persistent Angular Structure: new insights from diffusion MRI data. Dummy version.* Inf Process Med Imaging, 2003. **18**: p. 672-83.

72.   Hagmann, P., L. Cammoun, X. Gigandet, R. Meuli, C.J. Honey, V.J. Wedeen and O. Sporns, *Mapping the structural core of human cerebral cortex.* PLoS Biol, 2008. **6**(7): p. e159.

73.   Latt, J., M. Nilsson, A. Rydhog, R. Wirestam, F. Stahlberg and S. Brockstedt, *Effects of restricted diffusion in a biological phantom: a q-space diffusion MRI study of asparagus stems at a 3T clinical scanner.* Magma, 2007. **20**(4): p. 213-22.

74.   Hikishima, K., K. Yagi, T. Numano, K. Homma, N. Nitta, T. Nakatani and K. Hyodo, *Volumetric q-space imaging by 3D diffusion-weighted MRI.* Magn Reson Imaging, 2008. **26**(4): p. 437-45.

75.   Campbell, J.S., K. Siddiqi, V.V. Rymar, A.F. Sadikot and G.B. Pike, *Flow-based fiber tracking with diffusion tensor and q-ball data: validation and comparison to principal diffusion direction techniques.* Neuroimage, 2005. **27**(4): p. 725-36.

76. Fenyes, D.A. and P.A. Narayana, *In vivo echo-planar imaging of rat spinal cord.* Magn Reson Imaging, 1998. **16**(10): p. 1249-55.

77. Fenyes, D.A. and P.A. Narayana, *In vivo diffusion tensor imaging of rat spinal cord with echo planar imaging.* Magn Reson Med, 1999. **42**(2): p. 300-6.

78. Madi, S., K.M. Hasan and P.A. Narayana, *Diffusion tensor imaging of in vivo and excised rat spinal cord at 7 T with an icosahedral encoding scheme.* Magn Reson Med, 2005. **53**(1): p. 118-25.

79. Kim, Y.B., D. Kalthoff, C. Po, D. Wiedermann and M. Hoehn, *Connectivity of thalamo-cortical pathway in rat brain: combined diffusion spectrum imaging and functional MRI at 11.7 T.* NMR Biomed, 2012.

80. Wang, T.T., H.S. Kwon, G. Dai, R. Wang, S.M. Mijailovich, R.L. Moss, P.T. So, V.J. Wedeen and R.J. Gilbert, *Resolving myoarchitectural disarray in the mouse ventricular wall with diffusion spectrum magnetic resonance imaging.* Ann Biomed Eng, 2010. **38**(9): p. 2841-50.

81. Tseng, W.Y., V.J. Wedeen, T.G. Reese, R.N. Smith and E.F. Halpern, *Diffusion tensor MRI of myocardial fibers and sheets: correspondence with visible cut-face texture.* J Magn Reson Imaging, 2003. **17**(1): p. 31-42.

82. Tuch, D.S., J.J. Wisco, M.H. Khachaturian, L.B. Ekstrom, R. Kotter and W. Vanduffel, *Q-ball imaging of macaque white matter architecture.* Philos Trans R Soc Lond B Biol Sci, 2005. **360**(1457): p. 869-79.

83. Gilbert, R.J., T.A. Gaige, R. Wang, T. Benner, G. Dai, J.N. Glickman and V.J. Wedeen, *Resolving the three-dimensional myoarchitecture of bovine esophageal*

wall with diffusion spectrum imaging and tractography. Cell Tissue Res, 2008. **332**(3): p. 461-8.

84. Gilbert, R.J., V.J. Wedeen, L.H. Magnusson, T. Benner, R. Wang, G. Dai, V.J. Napadow and K.K. Roche, *Three-dimensional myoarchitecture of the bovine tongue demonstrated by diffusion spectrum magnetic resonance imaging with tractography.* Anat Rec A Discov Mol Cell Evol Biol, 2006. **288**(11): p. 1173-82.

85. Kim, D.S., M. Kim, I. Ronen, E. Formisano, K.H. Kim, K. Ugurbil, S. Mori and R. Goebel, *In vivo mapping of functional domains and axonal connectivity in cat visual cortex using magnetic resonance imaging.* Magn Reson Imaging, 2003. **21**(10): p. 1131-40.

86. Lorenz, R., M.E. Bellemann, J. Hennig and K.A. Il'yasov, *Anisotropic Phantoms for Quantitative Diffusion Tensor Imaging and Fiber-Tracking Validation.* Applied Magnetic Resonance, 2008. **33**(4): p. 419-429.

87. Laun, F.B., S. Huff and B. Stieltjes, *On the effects of dephasing due to local gradients in diffusion tensor imaging experiments: relevance for diffusion tensor imaging fiber phantoms.* Magn Reson Imaging, 2009. **27**(4): p. 541-8.

88. Farrher, E., J. Kaffanke, A.A. Celik, T. Stocker, F. Grinberg and N.J. Shah, *Novel multisection design of anisotropic diffusion phantoms.* Magn Reson Imaging, 2012.

89. R. Lorenz1, B. W. Kreher1, J. Hennig1, M. E. Bellemann2, K. A. Il'yasov1, *Anisotropic Fiber Phantom for DTI validation on a clinical scanner.* J Magn Reson, 2006.

90. Fieremans, E., Y. De Deene, S. Delputte, M.S. Ozdemir, Y. D'Asseler, J. Vlassenbroeck, K. Deblaere, E. Achten and I. Lemahieu, *Simulation and*

experimental verification of the diffusion in an anisotropic fiber phantom. J Magn Reson, 2008. **190**(2): p. 189-99.

91.   Yanasak, N. and J. Allison, *Use of capillaries in the construction of an MRI phantom for the assessment of diffusion tensor imaging: demonstration of performance.* Magn Reson Imaging, 2006. **24**(10): p. 1349-61.

92.   Cho, K.H., C.H. Yeh, J.D. Tournier, Y.P. Chao, J.H. Chen and C.P. Lin, *Evaluation of the accuracy and angular resolution of q-ball imaging.* Neuroimage, 2008. **42**(1): p. 262-71.

93.   von dem Hagen, E.A. and R.M. Henkelman, *Orientational diffusion reflects fiber structure within a voxel.* Magn Reson Med, 2002. **48**(3): p. 454-9.

94.   Fillard, P., M. Descoteaux, A. Goh, S. Gouttard, B. Jeurissen, J. Malcolm, A. Ramirez-Manzanares, M. Reisert, K. Sakaie, F. Tensaouti, T. Yo, J.F. Mangin and C. Poupon, *Quantitative evaluation of 10 tractography algorithms on a realistic diffusion MR phantom.* Neuroimage, 2011. **56**(1): p. 220-34.

95.   Jones, D.K. and M. Cercignani, *Twenty-five pitfalls in the analysis of diffusion MRI data.* NMR Biomed, 2010. **23**(7): p. 803-20.

96.   Bodammer, N., J. Kaufmann, M. Kanowski and C. Tempelmann, *Eddy current correction in diffusion-weighted imaging using pairs of images acquired with opposite diffusion gradient polarity.* Magn Reson Med, 2004. **51**(1): p. 188-93.

97.   Merhof, D., G. Soza, A. Stadlbauer, G. Greiner and C. Nimsky, *Correction of susceptibility artifacts in diffusion tensor data using non-linear registration.* Med Image Anal, 2007. **11**(6): p. 588-603.

98. Ellingson, B.M., T.F. Cloughesy, A. Lai, P.L. Nghiemphu and W.B. Pope, *Nonlinear registration of diffusion-weighted images improves clinical sensitivity of functional diffusion maps in recurrent glioblastoma treated with bevacizumab.* Magn Reson Med. **67**(1): p. 237-45.

99. Chiang, M.C., A.D. Leow, A.D. Klunder, R.A. Dutton, M. Barysheva, S.E. Rose, K.L. McMahon, G.I. de Zubicaray, A.W. Toga and P.M. Thompson, *Fluid registration of diffusion tensor images using information theory.* IEEE Trans Med Imaging, 2008. **27**(4): p. 442-56.

100. Irfanoglu, M.O., C.G. Koay, S. Pajevic, R. Machiraju and P.J. Basser, *Diffusion tensor field registration in the presence of uncertainty.* Med Image Comput Comput Assist Interv, 2009. **12**(Pt 1): p. 181-9.

101. Irfanoglu, M.O., R. Machiraju, S. Sammet, C. Pierpaoli and M.V. Knopp, *Automatic deformable diffusion tensor registration for fiber population analysis.* Med Image Comput Comput Assist Interv, 2008. **11**(Pt 2): p. 1014-22.

102. Pollari, M., T. Neuvonen and J. Lotjonen, *Affine registration of diffusion tensor MR images.* Med Image Comput Comput Assist Interv, 2006. **9**(Pt 2): p. 629-36.

103. Yang, J., D. Shen, C. Davatzikos and R. Verma, *Diffusion tensor image registration using tensor geometry and orientation features.* Med Image Comput Comput Assist Interv, 2008. **11**(Pt 2): p. 905-13.

104. Ziyan, U., M.R. Sabuncu, L.J. O'Donnell and C.F. Westin, *Nonlinear registration of diffusion MR images based on fiber bundles.* Med Image Comput Comput Assist Interv, 2007. **10**(Pt 1): p. 351-8.

105. O'Halloran, R.L., S. Holdsworth, M. Aksoy and R. Bammer, *Model for the correction of motion-induced phase errors in multishot diffusion-weighted-MRI of the head: Are cardiac-motion-induced phase errors reproducible from beat-to-beat?* Magn Reson Med.

106. Ben-Amitay, S., D.K. Jones and Y. Assaf, *Motion correction and registration of high b-value diffusion weighted images.* Magn Reson Med.

107. Kober, T., R. Gruetter and G. Krueger, *Prospective and retrospective motion correction in diffusion magnetic resonance imaging of the human brain.* Neuroimage. **59**(1): p. 389-98.

108. Benner, T., A.J. van der Kouwe and A.G. Sorensen, *Diffusion imaging with prospective motion correction and reacquisition.* Magn Reson Med. **66**(1): p. 154-67.

109. Van, A.T., D. Hernando and B.P. Sutton, *Motion-induced phase error estimation and correction in 3D diffusion tensor imaging.* IEEE Trans Med Imaging. **30**(11): p. 1933-40.

110. Van, A.T., D.C. Karampinos, J.G. Georgiadis and B.P. Sutton, *K-space and image space combination for motion artifact correction in multicoil multishot diffusion weighted imaging.* Conf Proc IEEE Eng Med Biol Soc, 2008. **2008**: p. 1675-8.

111. Gonzalez, J.E., P.M. Thompson, A. Zhao and Z. Tu, *Modeling diffusion-weighted MRI as a spatially variant gaussian mixture: application to image denoising.* Med Phys. **38**(7): p. 4350-64.

112.   Wiest-Daessle, N., S. Prima, P. Coupe, S.P. Morrissey and C. Barillot, *Non-local means variants for denoising of diffusion-weighted and diffusion tensor MRI.* Med Image Comput Comput Assist Interv, 2007. **10**(Pt 2): p. 344-51.

113.   Wirestam, R., A. Bibic, J. Latt, S. Brockstedt and F. Stahlberg, *Denoising of complex MRI data by wavelet-domain filtering: application to high-b-value diffusion-weighted imaging.* Magn Reson Med, 2006. **56**(5): p. 1114-20.

114.   Kim, Y., P.M. Thompson, A.W. Toga, L. Vese and L. Zhan, *HARDI denoising: variational regularization of the spherical apparent diffusion coefficient sADC.* Inf Process Med Imaging, 2009. **21**: p. 515-27.

115.   Schultz, T. and H.P. Seidel, *Estimating crossing fibers: a tensor decomposition approach.* IEEE Trans Vis Comput Graph, 2008. **14**(6): p. 1635-42.

116.   Wu, Y.C., A.S. Field and A.L. Alexander, *Computation of diffusion function measures in q-space using magnetic resonance hybrid diffusion imaging.* IEEE Trans Med Imaging, 2008. **27**(6): p. 858-65.

Vita

Vaibhav Juneja was born in Indore, India on August 18, 1979, the son of Sneh Lata Juneja and Jitendra Kumar Juneja. After completing his Bachelor of Engineering in Electrical and Telecommunication Engineering at Technical University of Rajiv Gandhi, Ujjain, India in 2001, he entered University of Connecticut in Storrs, Connecticut. He received the degree of Masters of Science with a major in Biomedical Engineering from UConn in May, 2004. For the next year, he gained experience working as a research engineer. In May of 2005 he entered The University of Texas Health Science Center at Houston Graduate School of Biomedical Sciences.

Permanent address:
2 Lormar Drive Etobicoke
Ontario, Canada, M9B4V6